AD-A278 000

(1)

DTIC
S ELECTE D
APR 1 2 1994
C

JAI Associates, Inc. Technical Report 93-01

A Free-Wake Euler and Navier-Stokes CFD Method and its Application to Helicopter Rotors Including Dynamic Stall

by

Ganapathi R. Srinivasan

DISTRIBUTION STATEMENT A
Approved for public release;
Distribution Unlimited

94-10898

JAI ASSOCIATES, INC.
SCIENCE & ENGINEERING CONSULTANTS

94 4 11 000

JAI Associates, Inc. Technical Report 93-01

A Free-Wake Euler and Navier-Stokes CFD Method and its Application to Helicopter Rotors Including Dynamic Stall

by

Ganapathi R. Srinivasan

JAI Associates, Inc.
P. O. Box 293
Mountain View, California 94042

November 1993

Accesion For
NTIS CRA&I ☑
DTIC TAB ☐
Unannounced ☐
Justification ________

By ________
Distribution /

Availability Codes

Dist	Avail and / or Special
A-1	

Final Report of the Contract DAAL03-90-C-0013
April 1990 - November 1993

Prepared for
U. S. Army Research Office
P. O. Box 12211
Research Triangle Park, North Carolina 27709-2211

Approved for Public Release; Distribution Unlimited

DTIC QUALITY INSPECTED 3

THE VIEW, OPINIONS, AND/OR FINDINGS CONTAINED IN THIS REPORT ARE THOSE OF THE AUTHOR'(S) AND SHOULD NOT BE CONSTRUED AS AN OFFICIAL DEPARTMENT OF THE ARMY POSITION, POLICY, OR DECISION, UNLESS SO DESIGNATED BY OTHER DOCUMENTATION.

REPORT DOCUMENTATION PAGE

Form Approved
OMB No 0704-0188

Public reporting burden for this collection of information is estimated to average 1 hour per response, including the time for reviewing instructions, searching existing data sources, gathering and maintaining the data needed, and completing and reviewing the collection of information. Send comments regarding this burden estimate or any other aspect of this collection of information, including suggestions for reducing this burden, to Washington Headquarters Services, Directorate for Information Operations and Reports, 1215 Jefferson Davis Highway, Suite 1204, Arlington, VA 22202-4302, and to the Office of Management and Budget, Paperwork Reduction Project (0704-0188), Washington, DC 20503

1. AGENCY USE ONLY *(Leave blank)*	**2. REPORT DATE** November 1993	**3. REPORT TYPE AND DATES COVERED**

4. TITLE AND SUBTITLE

A FREE-WAKE EULER AND NAVIER-STOKES CFD METHOD AND
ITS APPLICATION TO HELICOPTER ROTORS INCLUDING DYNAMIC STALL

5. FUNDING NUMBERS

6. AUTHOR(S)

GANAPATHI R. SRINIVASAN

7. PERFORMING ORGANIZATION NAME(S) AND ADDRESS(ES)

JAI Associates, Inc.
P. O. Box 293
Mountain View, California 94042-0293

8. PERFORMING ORGANIZATION REPORT NUMBER

9. SPONSORING/MONITORING AGENCY NAME(S) AND ADDRESS(ES)

U.S. Army Research Office
P.O. Box 12211
Research Triangle Park, NC 27709-2211

10. SPONSORING/MONITORING AGENCY REPORT NUMBER

11. SUPPLEMENTARY NOTES

The views, opinions and/or findings contained in this report are those of the author(s) and should not be construed as an official Department of the Army position, policy, or decision, unless so designated by other documentation.

12a. DISTRIBUTION/AVAILABILITY STATEMENT

Approved for public release; distribution unlimited.

12b. DISTRIBUTION CODE

13. ABSTRACT *(Maximum 200 words)*

This report summarizes the results of the research in two parts. Part I describes the development and application of a free-wake Euler and Navier-Stokes computational fluid dynamics method, called "TURNS", for helicopter applications. This finite-difference, implicit, upwind numerical method uses structured grids, and has been used for calculating the viscous, three-dimensional flowfields of rotors in hover, forward flight, blade-vortex interactions, and high speed impulsive noise. The good agreement of numerical results with experiments for surface pressures, wake trajectory, thrust, power, Figure of Merit, and acoustic wave forms indicate the accuray and suitability of the numerical method. It is demonstrated that both aerodynamics and acoustics information can be obtained in a single solution of the goverinig equations. In Part II, the unsteady flowfield results of a two-dimensional oscillating wing are presented for five widely used turbulence models and compared with experiments. The accuracy and suitability of turbulence models for unsteady separated flow are discussed.

14. SUBJECT TERMS

Free-wake, hover, viscous, three-dimensional, forward flight, Helicopter, Dynamic Stall, Light-stall, Deep-stall, Unsteady, Euler, Navier-Stokes, Blade-vortex interaction, Impulsive noise

15. NUMBER OF PAGES

117

16. PRICE CODE

17. SECURITY CLASSIFICATION OF REPORT	**18. SECURITY CLASSIFICATION OF THIS PAGE**	**19. SECURITY CLASSIFICATION OF ABSTRACT**	**20. LIMITATION OF ABSTRACT**
UNCLASSIFIED	UNCLASSIFIED	UNCLASSIFIED	UL

SUMMARY

This report summarizes the results of the research in two parts. Part I describes the development and application of a free-wake Euler and Navier-Stokes computational fluid dynamics method, called "TURNS", for helicopter applications. This finite-difference, implicit, upwind numerical method uses structured grids, and has been used for calculating the viscous, three-dimensional flowfields of rotors in hover, forward flight, blade-vortex interactions, and high speed impulsive noise. In this free-wake method, the induced effects of wake, including the interaction of tip vortices with successive blades, are captured as a part of the overall flowfield solution without specifying any wake models.

The hovering flowfield calculations are done for a two-bladed model rotor as well as for four-bladed modern rotors of UH-60A Blackhawk and BERP helicopters. Different modifications of the UH-60A blade have also been considered. Using the computational results, an attempt is made to understand the importance of planform effects of the various four-bladed rotor configurations considered. Calculated results are presented in the form of surface pressures, hover performance parameters, surface partice flow, tip vortex formation, and vortex wake trajectory. Comparison of calculated surface pressures and the nearfield wake trajectory for the model two-bladed rotor and the UH-60A Blackhawk rotor show good agreement with measured data. The captured vortex structure is, however, diffused due to coarse grids, but this appears to have minimal influence on the prediction of surface pressures and airloads. Comparison of UH-60A results with an equivalent rectangular UH-60A blade and a high-twist BERP blade indicates that the BERP blade, with an unconventional planform, produces more thrust at a given collective pitch, and approximately the same Figure of Merit. The high thrust conditions considered produce severe shock-induced flow separation for the UH-60A blade, while the BERP blade develops more thrust and minimal separation. The BERP blade produces a tighter tip vortex structure compared with the UH-60A blade. These results and the discussion presented bring out the similarities and differences between the various four-bladed, high performance rotors considered.

The capabilities of the TURNS code are further demonstrated by calculating the blade-vortex interactional flowfield of a rotor in forward flight and encountering an upstream generated concentrated line vortex. The code has also been used to calculate the acoustics of high speed impulsive noise in both hover and forward flight. Sample results are presented for these cases and compared with available experimental data. Limited comparisons of the Navier-Stokes results with the Euler results are also presented for both aerodynamics and acoustics.

In Part II, the unsteady flowfield results of an oscillating wing are presented. The unsteady flowfields of a two-dimensional oscillating wing are calculated using an implicit, finite-difference, Navier-Stokes numerical scheme using five widely used turbulence models. The objective of this study is to identify an appropriate turbulence model for accurate simulation of three-dimensional dynamic stall. Three unsteady flow conditions corresponding to attached flow, light-stall, and deep-stall of an oscillating wing experiment were chosen as test cases for computations. Results of unsteady airload hysteresis curves, harmonics of unsteady pressures, and instantaneous flowfield pictures are presented.

Unsteady airloads calculated using the turbulence models of the Baldwin-Lomax, Renormalization Group Theory, the Johnson-King, the Baldwin-Barth, and the Spalart-Allmaras are compared with experimental data of Piziali of U. S. Army Laboratory. The comparisons of unsteady airloads show that all models are deficient in some sense and not a single model predicts all airloads consistently and in agreement with experiment for all three regimes of flow conditions considered. Considering the overall performance of these models, the Baldin-Barth one-equation model appears to have a better performance when the flow is separated. It is also found to be the most expensive model in terms of computational cost. Finally, the three-dimensional oscillating wing calculations done using the Baldwin-Lomax turbulence model and a modified TURNS algorithm for the deep-stall case demonstrate that the simple algebraic model consistently underpredicts separation history just like in the two-dimensional case and the predicted airloads have poor agreement with experiments.

FOREWORD

The research reported in this document was performed for the U. S. Army Research Office under Contract DAAL03-90-C-0013 with co-funding from the U. S. Army Aeroflightdynamics Directorate at NASA Ames Research Center and the U. S. Air Force Office of Scietific Research. Dr. Thomas L. Doligalski was the Technical Monitor. Computational time and access to the supercomputer were provided by the Numerical Aerodynamic Simulation (NAS) Program Office and the Computational Aerosciences Branch at the NASA Ames Research Center.

Drs. W. J. McCroskey, Y. Yu, and T. L. Host have provided helpful suggestions and guidance at various stages of this investigation. The helpful assistance of Drs. J. D. Baeder, J. Ekaterinaris, V. Raghavan, and Mr. E. P. N. Duque at various stages of this project is appreciated.

p

TABLE OF CONTENTS

Section page

SUMMARY v

FORWARD vii

LIST OF SYMBOLS xi

LIST OF FIGURES xiii

PART I: TURNS Code and Its Application To Helicopter Rotors 1

1. INTRODUCTION 2

2. GOVERNING EQUATIONS AND NUMERICAL SCHEME 4

3. GRIDS AND BOUNDARY CONDITIONS 8

4. RESULTS AND DISCUSSION 10

   4.1 Model Two-Bladed Rotor in Hover 11

      4.1.1 Fine Grid Results 11

      4.1.2 Fine Grid versus Coarse Grid Results 12

      4.1.3 Euler versus Navier-Stokes Results 13

   4.2 Four-Bladed UH-60A Blackhawk and BERP Rotors in Hover 13

      4.2.1 UH-60A Blackhawk Model Rotor 14

      4.2.2 BERP Rotor 16

   4.3 Effect of Farfield Boundary Conditions 18

   4.4 Model Two-Bladed Rotor in Forward Flight 20

      4.4.1 Rotor in Forward Flight 20

      4.4.2 Three-Dimensional Parallel Blade-Vortex Interaction 21

   4.5 High-Speed Impulsive Noise in Hover and Forward Flight 21

5. CONCLUSIONS 22

PART II: Dynamic Stall of an Oscillating Wing 24

6. INTRODUCTION 25

7. GOVERINING EQUATIONS AND NUMERICAL SCHEME 26

8. TURBULENCE MODELS 30
9. RESULTS AND DISCUSSION 35
  9.1 Unsteady Attached flow Case 37
  9.2 Light-Stall Case 38
  9.3 Deep-Stall Case 40
10. CONCLUDING REMARKS 43
11. REFERENCES 45
12. FIGURES and TABLES 53
13. APPENDIX I 101
  List of Technical Papers Published 103
  TURNS Code Distribution List 105
  Recent Publication 107

LIST OF SYMBOLS

a_∞ = speed of sound, characteristic velocity scale

b = number of blades of the rotor

$c(r)$ = blade chord at radial location r

c_{eq} = equivalent blade chord, $1/R \int_{R_1}^{R} c(r)dr$

C_p = pressure coefficient based on local dynamic pressure

C_P = power coefficient, also equal to C_Q

C_Q = rotor torque coefficient, $Q/(2\pi R^3 q_{tip})$

C_{Q_i} = induced power

$C_{Q_{pr}}$ = component of power from surface pressure integration

$C_{Q_{prof}}$ = profile power

C_{Q_s} = component of power from surface skin friction integration

C_t = sectional thrust coefficient based on local chord, $dt/dr/(c(r)q_{tip})$

$\overline{C}_t$ = sectional thrust coefficient based on c_{eq}, $dt/dr/(c_{eq}q_{tip})$

C_{tave} = area under C_t vs r curve

C_T = rotor thrust coeffient, $T/(2\pi R^2 q_{tip})$

dt = incremental thrust

dr = incremental radial distance

e = energy per unit volume

$\widehat{E}, \widehat{F}, \widehat{G}$ = inviscid flux vectors

J = Jacobian of the coordinate transformation

FM = Figure of Merit, $0.707C_T^{3/2}/C_Q$

FM_i = Figure of Merit without viscous contribution, $0.707C_T^{3/2}/C_{Q_i}$

FM_{max} = maximum value of Figure of Merit

M_∞ = free stream Mach number, forward speed of the rotor

M_{tip} = blade-tip Mach number

p = static pressure

Pr = Prandtl number

q_{tip} = rotational dynamic pressure, $1/2\ \rho(\Omega\ \mathrm{R})^2$

$\widehat{Q}$ = flowfield vector of conserved flow quantities

Q = rotor torque

r = rotor radial coordinate

R = blade radius

R_1 = blade radius at the root section

Re = Reynolds number based on M_{tip} and c_{eq}

$\widehat{S}$ = viscous flux vector

T = rotor thrust

u, v, w = velocity components in physical space

u_{loc} = local blade speed

U, V, W = contravariant velocity components

x, y, z, t = inertial coordinates

x_o, z_o = vortex offset position relative to the rotor axis

$\tilde{x}_v, \tilde{z}_v$ = distance from blade leading edge to the line vortex

$\tilde{x}, \tilde{y}, \tilde{z}, \tilde{t}$ = blade-fixed coordinates

α = angle of attack, degrees

Γ = sectional bound circulation, also vortex strength

$\tilde{\Gamma}$ = dimensionless strength of vortex, $\Gamma/(a_\infty C)$

$\widehat{\Gamma}$ = normalised blade sectional bound circulation, $\Gamma/\Omega R^2$

θ_c = collective pitch

ρ = density

σ = rotor geometric solidity, $b \int_{R_1}^{R} c(r)dr/(\pi R^2)$

μ = viscosity coefficient, also advance ratio of rotor

ξ, η, ζ, τ = body-conforming coordinates of computational space

ψ = azimuthal angle

Ω = rotor angular velocity

LIST OF FIGURES

Figure Page

Fig. 1 A C-H cylindrical grid topology for a two-bladed rotor; a) view in the plane of the rotor, and b) isometric view showing the grid boundaries for a single blade. 56

Fig. 2 Comparison of surface pressures for a lifting rotor in hover; $M_{tip} = 0.44$, $\theta_c = 8°$, and $Re = 1.92\times10^6$. 57

Fig. 3 Comparison of surface pressures for a lifting rotor in hover; $M_{tip} = 0.877$, $\theta_c = 8°$, and $Re = 3.93\times10^6$. 58

Fig. 4 Comparison of surface pressures for a lifting rotor in hover; $M_{tip} = 0.794$, $\theta_c = 12°$, and $Re = 3.55\times10^6$. 59

Fig. 5 Computed surface particle flow detail highlights the shock-induced boundary layer separation for the flow conditions of a) $M_{tip} = 0.877$, $\theta_c = 8°$, and $Re = 3.93\times10^6$, and b) $M_{tip} = 0.794$, $\theta_c = 12°$, and $Re = 3.55\times10^6$. 60

Fig. 6 Comparison of bound circulation distribution for the case of collective pitch $\theta_c = 8°$ with tip speeds of $M_{tip} = 0.44$ and 0.877. 60

Fig. 7 Calculated tip vortex particle flow details showing the near-field view for the flow condition of $M_{tip} = 0.794$, $\theta_c = 12°$, and $Re = 3.55\times10^6$. 61

Fig. 8 Calculated tip vortex trajectory for the flow conditions of $M_{tip} = 0.44$, $\theta_c = 8°$, and $Re = 1.92\times10^6$; views show (a) contraction of wake (looking from the top), (b) captured tip vortex path and its vertical descent, and (c) comparison of the calculated trajectory over 450° of vortex age with experments. 61

Fig. 9 Comparison of surface pressures with coarse and fine grids for the case of $M_{tip} = 0.877$, $\theta_c = 8°$, and $Re = 3.93\times10^6$. 62

Fig. 10 Comparison of surface pressures for Euler and Navier-Stokes solutions; $M_{tip} = 0.877$, $\theta_c = 8°$, and $Re = 3.93\times10^6$. 63

Fig. 11 Planform views and surface grids for the a) BERP and b) UH-60A rotor blades. 64

Fig. 12 Radial twist distributions for the UH-60A and BERP rotor blades. ... 64

Fig. 13 View of a C-H grid for a single BERP blade showing outer boundaries and grid in the plane of the blade. 65

Fig. 14 Surface pressure distributions at various span stations for the UH-60A blade compared with experiments. $M_{tip} = 0.628$, Re = 2.75 x 10^6, and calculated $C_T/\sigma = 0.084$. 66

Fig. 15 Sectional thrust loading for the UH-60A blade, equivalent UH-60A rectangular blade, and the UH-60A blade with linear twist distribution in the tip region. $M_{tip} = 0.628$, $\theta_c = 9°$, and Re = 2.75 x 10^6. 67

Fig. 16 Comparison of calculated sectional thrust loading for the UH-60A blade for two thrust conditions. $M_{tip} = 0.628$, and Re = 2.75 x 10^6. 67

Fig. 17 Upper surface particle flow (skin friction) patterns of UH-60A blade for $\theta_c = 9°$ and 13° cases at $M_{tip} = 0.628$ and Re = 2.75 x 10^6. 68

Fig. 18 Close-up view of surface particle flow in the tip region for the UH-6A0 blade at $\theta_c = 9°$ and $\theta_c = 13°$. $M_{tip} = 0.628$, and Re = 2.75 x 10^6. 68

Fig. 19 Mach contours for the UH-60A blade for the conditions of $M_{tip} = 0.628$, $\theta_c = 13°$, and Re = 2.75 x 10^6. Views show upper surface contours at $L = 8$ (away from the wall), and cross-sectional plane at $r/R = 0.94$. 69

Fig. 20 Comparison of calculated and experimental hover performance for four-bladed UH-60A Blackhawk and BERP rotors. 70

Fig. 21 Comparison of calculated and experimental Figure of Merit for four-bladed UH-60A Blackhawk and BERP rotors. 71

Fig. 22 Surface pressure distributions for the BERP rotor blade at different span stations; $M_{tip} = 0.628$, $\theta_c = 13°$ and Re = 2.94 x 10^6. 72

Fig. 23 Radial circulation distributions for the UH-60A and BERP blades at a collective pitch setting of $\theta_c = 9°$ with $M_{tip} = 0.628$. 73

Fig. 24 Comparison of radial thrust loadings for the BERP blade at $\theta_c = 9°$ and 13° with $M_{tip} = 0.628$ and Re = 2.94 x 10^6. 73

Fig. 25 Bound circulation distributions for the BERP blade for the conditions of Fig. 24. 73

Fig. 26 Upper surface particle flow details for the BERP blade at $\theta_c = 9°$ and 13°; $M_{tip} = 0.628$ and Re = 2.94 x 10^6. 74

Fig. 27 Upper surface particle flow pattern and pressure contours at the notch region for the BERP blade at $M_{tip} = 0.628$, $\theta_c = 13°$, and Re = 2.94 x 10^6. ... 74

Fig. 28 Near-field view of tip vortex formation and roll-up process for the BERP blade at $\theta_c = 13°$, $M_{tip} = 0.628$. 75

Fig. 29 Schematic of new farfield boundary conditions for the hovering rotor. .. 76

Fig. 30 Sectional thrust distributions for the UH-60A blade with old and new farfield boundary conditions compared with experimental data. $M_{tip} = 0.628$, $\theta_c = 9°$, and Re = 2.75 x 10^6. 76

Fig. 31 Calculated wake contraction and descent for the 4-bladed UH-60A Black

Hawk rotor. Views show (a) planform view of wake contraction looking from top; (b) wake contraction and descent looking from side; and (c) comparison calculated results with experimental data for the flow condition of $M_{tip} = 0.628$, $\theta_c = 9°$, and Re = 2.75×10^6. 71

Fig. 32 Comparison of instantaneous surface pressures for a nonliftng two-bladed rotor in forward flight. $M_{tip} = 0.6$, $\mu = 0.2$, and $Re = 2.22\text{x}10^6$ at $r/R = 0.893$. 78

Fig. 33 Instantaneous surface pressures of a nonlifting rotor in forward flight at different azimuthal locations compared with experiments. $M_{tip} = 0.8$, $\mu = 0.2$, and $Re = 2.89\text{x}10^6$ at $r/R = 0.893$. 79

Fig. 34 Instantaneous surface pressures during transonic parallel BVI at $\Psi = 174.5°$ azimuth compared with experiments. $M_{tip} = 0.8$, $\mu = 0.2$, $Re = 2.89\text{x}10^6$, $\tilde{\Gamma} = 0.177$, $x_o = 0.0$, $z_o = -0.4$, at $r/R = 0.893$. 80

Fig. 35 Pressure-time histories of high-speed impulsive noise of a hovering rectangular blade rotor in-plane at $r/R = 3.09$ and at a blade-tip Mach number of (a) $M_{tip} = 0.90$, and (b) $M_{tip} = 0.95$. 81

Fig. 36 Pressure-time histories of high-speed impulsive noise for an advancing rotor in-plane at 1.8 rotor diameters directly in front of the blade at $M_{tip} = 0.896$, $\mu = 0.348$, and $Re = 2.17\text{x}10^6$ compared to wind tunnel and flight test data. 81

Fig. 37 Quasi-steady surface pressure distributions of NACA 0015 airfoil compared to experiments (Ref. 19) at flow conditions of $M_\infty = 0.29$, $Re = 1.95\text{x}10^6$; a) $\alpha = 11°$; b) $\alpha = 17°$. 82

Fig. 38 Comparison of calculated unsteady airloads hysteresis of oscillating wing for different turbulence models with experiments. $M_\infty = 0.29$, $\alpha(t) = 4° + 4.2° sin(Kt)$, $k = 0.1$, $Re = 1.95\text{x}10^6$. 83

Fig. 39 Comparison of harmonic components of unsteady pressures for different turbulence models at the experimental conditions of Fig. 38.. 84

Fig. 40 Comparsion of unsteady airloads hysteresis for J-K model with different constant time-steps for the oscillating cycle and experiments. $M_\infty = 0.29$, $\alpha(t) = 11° + 4.2° sin(Kt)$, $k = 0.1$, and $Re = 1.95 \text{x} 10^6$. 85

Fig. 41 Effect of numerical dissipation on the solution accuracy with J-K model for the experimental conditions of Fig. 40. 86

Fig. 42 Effect of grid sensitivity on the solution accuracy with J-K model for the experimental conditions of Fig. 40. 87

Fig. 43 Effect of grid sensitivity on the solution accuracy with B-B model for the experimental conditions of Fig. 40. 88

Fig. 44 Comparison of unsteady airloads hysteresis for different turbulence models with experiments for the flow conditions of Fig. 40. 89

Fig. 45 Comparison of harmonic components of unsteady pressures for the J-K and B-B turbulence models at the flow conditions of Fig. 40. 90

Fig. 46 Comparison unsteady airloads hysteresis for different turbulence models with experiments. $M_\infty = 0.29$, $k = 0.1$, $Re = 1.95 \text{x} 10^6$, and $\alpha(t) = 15° + 4.2° sin(Kt)$. 91

Fig. 47 Calculated unsteady surface pressures during an oscillatory cycle for the flow conditions of Fig. 46 using the B-B turbulence model. 92

Fig. 48 Calculated harmonic components of unsteady pressures for the flow conditions of Fig. 46 using the B-B turbulence model. 93

Fig. 49 Locus of flow reveral point during the oscillatory cycle for different turbulence models for the flow conditions of Fig. 46. 94

Fig. 50 Instantaneous steamline patterns at four different time instants during the oscillatory cycle for the B-B turbulence model and for the flow conditions of Fig. 46. 95

Fig. 51 Comparison of instantaneous streamline patterns for different turbulence models at 16° downstroke during the oscillatory cycle for the flow conditions of Fig. 46. 96

Fig. 52 Instantaneous streakline pattern for flow at 16° downstroke using the Baldwin-Barth model and for the flow conditions of Fig. 51. 97

Fig. 53 Comparison of unsteady airloads hysteresis for different turbulence models with experiments. $M_\infty = 0.29$, $k = 0.1$, $Re = 1.95 \times 10^6$, and $\alpha(t) = 17° + 4.2° sin(Kt)$. 98

Fig. 54 Comparison of relative costs of computations with different turbulence models. 99

LIST OF TABLES

Table 1: Calculated and experimental hover performance parameters for the UH-60A Blackhawk and BERP rotors for $M_{tip} = 0.628$ 55

Table 2: Thrust and power coefficients for the UH-60A and BERP rotors 55

Table 3: Table 3: Quasi-steady airloads 82

PART I

TURNS CODE AND ITS APPLICATION TO HELICOPTER ROTORS

1. INTRODUCTION

The accurate numerical simulation of the helicopter rotor flowfield in hover continues to be one of the most complex and challenging problems of applied aerodynamics. This is true despite the availability of the present day supercomputers and improved numerical algorithms. The complexity of the flow stems from several peculiar features that are unique to the helicopter rotor; the dominant of these is the vortical wake, since is is responsible for producing unsteady loads fluctuation, noise, and vibration. In other words, the vortical wake strongly influences the operating characteristics of helicopter. Accurate prediction of this vortical wake is probably the most important, most studied and the most difficult aspect of helicopter flowfield.

Current methods of analysis of wakes range in complexity from relatively simple momentum-theory applications to sophisticated free-wake methods. In between these extremes, there exists a variety of so-called prescribed-wake models[1]. Although such methods are often used in industry for predicting airloads, they do suffer from the limitation that the empirical determination of wake shape ignores some of the important flowfield details such as the mutual interaction of individual vortex elements. Since most of these flowfield prediction methods have to be coupled with some wake model for realistic estimates of airloads, they are, therefore, restricted in their application to blade shapes and planforms that are geometrically simple. Besides, further modeling is required to simulate the formation of concentrated tip vortex in the tip region.

Although, a complete flowfield simulation of helicopter is still beyond the current capability, a combination of powerful supercomputers in conjuction with improved numerical algorithms have enabled advances to be made, recently, using Computational Fluid Dynamics (CFD) to solve the equations of fluid motion for individual elements of such a complex flowfield. The solution schemes for these equations are usually coupled with integral wake models, e. g. vortex line elements, vortex lattices, or panels, to bring in the influence of the vortex wake. Techniques that implement this idea using a "prescribed" wake geometry encompass potential flow[1-5], Euler[6-8] and Navier-Stokes methods[9-12]. Also, a potential flow method[13] has been coupled with a "free" wake approach, in which the wake vorticity is specified, but is allowed to convect freely with the flow without constraining its trajectory. Other recent methods, including the present one, use direct techniques for the entire solution process, using Euler[14-17] and Navier-Stokes[18] flow solvers by capturing the influence of wake as a part of the overall flowfield solution. In this context one can refer to these "free-wake" methods as wake-capturing schemes, in analogy to shock-capturing, whereas the "coupled-" or "prescribed-wake" methods are somewhat analogous to shock-fitting. In another study, a totally different approach has been followed that is different from the above schemes, viz., the Navier-Stokes calculations have been performed[19] for the global time-averaged wake alone, with the details of the flow on the rotor itself prescribed.

The weakest link in the wake-coupled methodologies[1-12] is the wake modeling. That is, the technique of specifying a prescribed wake has to be specialized for each blade shape, making it difficult to treat blade shapes with arbitrary twist, taper, and planforms. Therefore , the purpose of this study is to develop an improved calculation method for the solution of Navier-Stokes equations for the complete flowfield of a lifting rotor, including the wake and its induced effects. The vortex wake and its effects are captured as a part of the complete flowfield, and thus no arbitrary inputs or vortex-modeling approximations are necessary to describe the wake. In addition to the wake-capturing capabilities, the Navier-Stokes approach is chosen for the following reasons: 1) better tip-flow simulation, which involves resolving the flow separation and the formation of a concentrated tip vortex, 2) accurate simulation of strong viscous-inviscid interaction involving shock induced separation at high blade tip speeds and high collective pitch conditions, and 3) future modeling of retreating blade and dynamic stall regimes in forward flight.

A new free-wake Euler and Navier-Stokes CFD method, called TURNS (transonic unsteady rotor Navier-Stokes) Code, is developed for helicoter rotors in this study. This is an improvement of the version that was developed previously by the present author in related studies with wake modeling[9]. One fundamental difference of the present numerical scheme is the use of Roe's upwinding for all three coordinate directions[20]. This feature, coupled with an implicit iterative procedure has produced a fast, efficient, and accurate numerical scheme. In addition, a periodic boundary condition[17] has been implemented in the azimuthal direction, as described later in the text. Also, a new procedure for implementing farfield boundary conditions for a hovering rotor has been used. These improvements allow the near wake to be computed well enough to approximately simulate the correct inflow through the rotor, thus obviating the need for the *ad hoc* wake modeling used previously[9]. These additional changes in the Euler/Navier-Stokes algorithm are based on some of the numerical procedures described in Ref. 21.

Radiated noise can severely restrict rotorcraft usage in both civilian and military operations. Impulsive noise, the sum total of the blade-vortex interaction (BVI) noise and the high-speed impulsive (HSI) noise, forms the most important component of the radiated noise. The BVI noise is generated due to the interaction of the vortical wake with rotating blades and is generally more difficult to model due to the importance of unsteady, three-dimensional, and vortex wake effects. High-speed impulsive noise, on the other hand, is caused primarily due to compressibility effects. If the advancing blade tip Mach number is highly supercritical, the phenomenon known as delocalization may occur, wherein the supersonic pocket on the rotor blade extends out to the far-field beyond the blade tip. If this occurs, the noise becomes more impulsive and in particular gets focused in its direction of propagation. Fortunately, the influence of lift on HSI noise appears to be secondary[22]. Thus, one can estimate this even with nonlifting configurations.

Recent studies using the Euler and Navier-Stokes method of TURNS have demonstrated the feasibility of using a single computational fluid dynamics (CFD) method to calculate simultaneously the aerodynamics and acoustics of a helicopter rotor in hover and forward flight[23], including the blade-vortex interaction. The calculations of the high-speed impulsive noise are in good agreement atleast upto a distance of about three rotor radius. This numerical procedure is, thus, capable of calculating the aerodynamics and the acoustics (HSI) out to several rotor diameters all in one single solution without using any modeling either for wake or for acoustic propagation. The vortical wake and its influence as well as the acoustics are captured as a part of the overall flowfield solution. Comparisons of the numerical results with the available experimental data demonstrate the accuracy and suitability of this numerical method. The next few sections of this report describe the details of the numerical procedure of TURNS code and example solutions are given for validation.

2. GOVERNING EQUATIONS AND NUMERICAL SCHEME

The governing differential equations are the thin layer Navier-Stokes equations. These can be written in conservation-law form in a generalized body-conforming curvilinear coordinate system as follows[24]:

$$\partial_\tau \widehat{Q} + \partial_\xi \widehat{E} + \partial_\eta \widehat{F} + \partial_\zeta \widehat{G} = \frac{\varepsilon}{Re} \partial_\zeta \widehat{S} + \widehat{\Re} \tag{1}$$

where Re is the Reynolds number, $\varepsilon = 0$ or 1 for the Euler or the Navier-Stokes equations, respectively, and $\tau = t$, $\xi = \xi(x,y,z,t)$, $\eta = \eta(x,y,z,t)$ and $\zeta = \zeta(x,y,z,t)$. The coordinate system (x,y,z,t) is attached to the blade (see Fig. 1). The vector of conserved quantities $\widehat{Q}$ and the inviscid flux vectors $\widehat{E}$, $\widehat{F}$, and $\widehat{G}$ are given by

$$\widehat{Q} = \frac{1}{J} \begin{bmatrix} \rho \\ \rho u \\ \rho v \\ \rho w \\ e \end{bmatrix}, \qquad \widehat{E} = \frac{1}{J} \begin{bmatrix} \rho U \\ \rho u U + \xi_x p \\ \rho v U + \xi_y p \\ \rho w U + \xi_z p \\ U H - \xi_t p \end{bmatrix}$$

$$\widehat{F} = \frac{1}{J} \begin{bmatrix} \rho V \\ \rho u V + \eta_x p \\ \rho v V + \eta_y p \\ \rho w V + \eta_z p \\ V H - \eta_t p \end{bmatrix}, \widehat{G} = \frac{1}{J} \begin{bmatrix} \rho W \\ \rho u W + \zeta_x p \\ \rho v W + \zeta_y p \\ \rho w W + \zeta_z p \\ W H - \zeta_t p \end{bmatrix} \tag{2}$$

In these equations, $H = (e+p)$ and U, V, and W are the contravariant velocity components defined, for example, as $U = \xi_t + \xi_x u + \xi_y v + \xi_z w$. The Cartesian velocity components are given by u, v, and w in the x, y, and z directions, respectively. Also, the density, pressure, and the total energy per unit volume are represented by ρ, p, and e, respectively. While the velocity and length scales are nondimensionalized by the characteristic velocity and length scales, given by the ambient sound speed a_∞ and the rotor blade chord c, the pressure p, density ρ, and the energy e are nondimensionalized by the freestream reference values p_∞/γ, ρ_∞, and $\rho_\infty a^2{}_\infty$, respectively. The quantities ξ_x, ξ_y, ξ_z, ξ_t, etc. are the coordinate transformation metrics and J is the Jacobian of the transformation. For the thin layer approximation used here, the viscous flux vector $\widehat{S}$ is given by

$$\widehat{S} = \frac{1}{J}\begin{bmatrix} 0 \\ \mu m_1 u_\zeta + \frac{\mu}{3} m_2 \zeta_x \\ \mu m_1 v_\zeta + \frac{\mu}{3} m_2 \zeta_y \\ \mu m_1 w_\zeta + \frac{\mu}{3} m_2 \zeta_z \\ \mu m_1 m_3 + \frac{\mu}{3} m_2 (\zeta_x u + \zeta_y v + \zeta_z w) \end{bmatrix} \tag{3}$$

with

$$\begin{aligned} m_1 &= \zeta_x^2 + \zeta_y^2 + \zeta_z^2 \\ m_2 &= \zeta_x u_\zeta + \zeta_y v_\zeta + \zeta_z w_\zeta \\ m_3 &= \frac{1}{2}(u^2 + v^2 + w^2)_\zeta + \frac{1}{Pr\,(\gamma - 1)}(a^2)_\zeta \end{aligned}$$

where Pr is the Prandtl number, γ is the ratio of specific heats, and a is the speed of sound. For the noninertial reference frame used in this study, source terms have to be included in Eq. (1) to account for the centrifugal acceleration of the rotating blade[25]. The term $\widehat{\mathfrak{R}}$ represents this in Eq. (1) and is given for a rigid rotor rotating in the x - y plane by

$$\widehat{\mathfrak{R}} = \frac{1}{J}\begin{bmatrix} 0 \\ \Omega \rho v \\ -\Omega \rho u \\ 0 \\ 0 \end{bmatrix} \tag{4}$$

where Ω is the angular velocity of the rotor. The fluid pressure p is related to the conserved flow quantities through the nondimensional equation of state for a perfect gas given by,

$$p = (\gamma - 1)\{\, e - \frac{\rho}{2}(u^2 + v^2 + w^2)\, \} \tag{5}$$

For turbulent viscous flows, the nondimensional viscosity coefficient μ in $\widehat{S}$ is computed as the sum of $\mu_l + \mu_t$ where the laminar viscosity, μ_l, is estimated using Sutherland's law and the turbulent viscosity, μ_t, is evaluated using the Baldwin-Lomax algebraic eddy viscosity model[26].

A finite-difference, upwind numerical algorithm is developed for the helicopter rotor applications. In this, the evaluation of the inviscid fluxes is based on an upwind-biased flux-difference scheme originally suggested by Roe[27] and later extended to three-dimensional flows by Vatsa et al.[20] The chief advantage of using upwinding is that it eliminates the addition of explicit numerical dissipation and has been demonstrated to produce less dissipative numerical solutions[20]. This feature, coupled with a fine grid description in the tip region, increases the accuracy of the wake simulation. The van Leer monotone upstream-centered scheme for the conservative laws (MUSCL) approach[28] is used to obtain the second- or third-order accuracy with flux limiters so as to be total variation diminishing (TVD). Lower-Upper - Symmetric Gauss-Seidel (LU-SGS) scheme, suggested by Jameson and Yoon[29-30], is used for the implicit operator.

The space-discretized form of the differential Eq. (1) at node (j,k,l) is

$$\begin{aligned}\partial_\tau \widehat{Q} = &-\frac{\widehat{E}_{j+\frac{1}{2}} - \widehat{E}_{j-\frac{1}{2}}}{\Delta\xi} - \frac{\widehat{F}_{k+\frac{1}{2}} - \widehat{F}_{k-\frac{1}{2}}}{\Delta\eta} - \frac{\widehat{G}_{l+\frac{1}{2}} - \widehat{G}_{l-\frac{1}{2}}}{\Delta\zeta} \\ &+ \frac{\varepsilon}{Re}\frac{\widehat{S}_{l+\frac{1}{2}} - \widehat{S}_{l-\frac{1}{2}}}{\Delta\zeta} + \widehat{\Re}_{j,k,l}\end{aligned} \tag{6}$$

where j, k, and l correspond to the ξ, η, and ζ coordinate directions, respectively.

The application of Roe's upwinding to the numerical flux of the inviscid terms results in the locally one-dimensional form and can be written, e.g., in the ξ direction, as

$$\begin{aligned}&\widehat{E}(Q_L, Q_R, (\nabla\xi/J)_{j+\frac{1}{2}}) = \\ &\frac{1}{2}[\widehat{E}(Q_R, (\nabla\xi/J)_{j+\frac{1}{2}}) + \widehat{E}(Q_L, (\nabla\xi/J)_{j+\frac{1}{2}}) \\ &- |A(Q_L, Q_R, (\nabla\xi/J)_{j+\frac{1}{2}})|(Q_R - Q_L)]\end{aligned} \tag{7}$$

where A is the Roe-averaged Jacobian matrix and Q_L and Q_R are the left and right state variables. The scheme degenerates to the first-order accuracy if $Q_L = Q_j$ and $Q_R = Q_{j+1}$, for example, at the grid boundaries. Higher-order schemes can be constructed from a one-parameter family of interpolations for the primitive variables ρ, u, v, w, and p. For example, the left and right state variables for p are,

$$p_L = \{1 + \frac{\psi_j}{4}[(1-\kappa)\nabla + (1+\kappa)\Delta]\}p_j \tag{8a}$$

$$p_R = \{1 - \frac{\psi_{j+1}}{4}[(1+\kappa)\nabla + (1-\kappa)\Delta]\}p_{j+1} \tag{8b}$$

where ∇ and Δ are backward and forward difference operators, and κ is a parameter that controls the construction of higher-order differencing schemes. For example, $\kappa = \frac{1}{3}$ is used in the present method to construct the third-order scheme. The limiter ψ is calculated by using Koren's differentiable limiter[31] as

$$\psi_j = \frac{3\nabla p_j \Delta p_j + \epsilon}{2(\Delta p_j - \nabla p_j)^2 + 3\nabla p_j \Delta p_j + \epsilon} \tag{9}$$

where a small constant, typically $\epsilon = 10^{-6}$, is added to prevent the division by zero. Similar formulae are used for the other primitive variables. The viscous flux terms are discretized using standard second-order central-differencing[24].

The time marching integration procedure uses the LU-SGS method. The details of this scheme are described elsewhere[21]. Briefly, the lower-upper factored symmetric Gauss-Seidel method is a direct modification of the approximate lower-diagonal-upper (LDU) factorization to the unfactored implicit matrix. The resulting factorization can be regarded as the symmetric Gauss-Seidel relaxation method. The LDU factorization yields better stability than the simple LU factorization since the diagonal elements always have the absolute value of the Jacobian matrices.

The final form of this algorithm can be written for a first-order time accurate scheme as

$$LDU\Delta\hat{Q}^n = -\Delta t RHS^n \tag{10}$$

where

$$\begin{aligned} L =& I - \Delta t\hat{A}^-|_{j,k,l} + \Delta t\nabla_\xi\hat{A}^+ \\ &- \Delta t\hat{B}^-|_{j,k,l} + \Delta t\nabla_\eta\hat{B}^+ \\ &- \Delta t\hat{C}^-|_{j,k,l} + \Delta t\nabla_\zeta\hat{C}^+ \end{aligned} \tag{11a}$$

$$\begin{aligned} D =& [I + \Delta t(\hat{A}^+ - \hat{A}^- \\ &+ \hat{B}^+ - \hat{B}^- + \hat{C}^+ - \hat{C}^-)|_{j,k,l}]^{-1} \end{aligned} \tag{11b}$$

$$\begin{aligned} U =& I + \Delta t\hat{A}^+|_{j,k,l} + \Delta t\Delta_\xi\hat{A}^- \\ &+ \Delta t\hat{B}^+|_{j,k,l} + \Delta t\Delta_\eta\hat{B}^- \\ &+ \Delta t\hat{C}^+|_{j,k,l} + \Delta t\Delta_\zeta\hat{C}^- + \frac{\partial R}{\partial Q} \end{aligned} \tag{11c}$$

where Δt is the time step, RHS represents the discretized steady state terms, e. g., Eq. (6), and n refers to the current time-level. Also, $A^+ = \frac{1}{2}(A + \sigma_\xi)$, $A^- = \frac{1}{2}(A - \sigma_\xi)$, $\sigma_\xi = |U| + ar_\xi + \epsilon$, $\epsilon = 0.01$ typically, and $r_\xi = \sqrt{{\xi_x}^2 + {\xi_y}^2 + {\xi_z}^2}$. Also, in addition to the source term $\Re$ added to the right side of the Eq. (6), a source term Jacobian, $\partial R/\partial Q$, is added to either L or U operator on the left hand side of Eq. (10). In the present case this is added to the U operator, as shown in Eq. (11c), and is given by

$$\frac{\partial R}{\partial Q} = \frac{1}{J}\begin{bmatrix} 0 & 0 & 0 & 0 & 0 \\ 0 & 0 & \Omega & 0 & 0 \\ 0 & -\Omega & 0 & 0 & 0 \\ 0 & 0 & 0 & 0 & 0 \\ 0 & 0 & 0 & 0 & 0 \end{bmatrix} \tag{12}$$

As a result of the simplified form of the Jacobian terms, e.g., A^+, all the diagonal elements of L, D, and U reduce to scalar elements. Thus this method requires only two (one forward and one backward) sweeps with scalar inversions and leads to less factorization error. The source term adds two off-diagonal elements, resulting in slightly more computational work.

The present numerical scheme uses a modified finite-volume method for calculating the metrics. The chief advantage of standard finite-volume formulations is that both space and time metrics can be formed accurately[25] and that the free-stream is captured accurately[17]. However, to be compatible with the present finite-difference numerical scheme, the space metrics are evaluated at the grid nodes instead of cell interfaces. But, the time metrics are evaluated in the same manner as in a finite-difference scheme, which is computationally less expensive than a rigorous finite-volume calculation. As a result, free-stream subtraction of the time-metric terms is then required to restore time accuracy.

In the calculation procedure, the rotor blade is started from rest in a quiescent fluid and the evolution of the flowfield is monitored as the blade moves in azimuth. To take advantage of the quasi-steady nature of the asymptotic hovering rotor flowfield in blade-fixed coordinates, a locally-varying time step is used in the integration procedure to accelerate convergence, as suggested in Ref. 32.

3. GRIDS AND BOUNDARY CONDITIONS

Body-conforming, single-block, three-dimensional computational grids were constructed for the rectangular rotor blades[33] by stacking and bending two-dimensional C-H grids which were generated by an elliptic solver[34]. Because of the cylindrical nature of the flow of a hovering rotor, a C-H cylindrical grid topology was chosen, as in Ref. 17, with the wrap-around C-direction in the chordwise direction and H-type in the spanwise direction. In contrast to the experimental model rotor that has a square tip, the present grid generator approximates this as a bevel tip because of the H-topology in the spanwise direction (see Ref. 35).

The standard viscous grids used here had 217 grid points in the wrap-around (along the chord) direction with 144 points on the body, 71 points in the spanwise (radial) direction with 55 points on the blade surface, and 61 points in the normal direction. The grid was clustered near the leading and trailing edges and near the tip region to resolve the tip vortex. It was also clustered in the normal direction to resolve the viscous flow near the blade surface. There are about 15 points in the boundary layer with a spacing of the first grid point from the surface equal to 5×10^{-5} chord ($y^+ = O(1)$). A coarse grid was constructed from this fine viscous grid by removing every other point in all three directions. The inboard plane near the axis of rotation was located at a radial station equal to one chord. The grid outer boundaries were set at 8 chords in all directions. The same grids were used for the Euler calculations.

Figure 1 shows the coarse grid that was used in the computations. Because of the symmetry of the hovering flow and the periodic boundary condition described below, the calculations could be performed for only one blade. Figure 1a shows the cylindrical nature of the grid in the plane of the rotor, and Fig. 1b shows an isometric view of the grid boundary for a single blade. For clarity, the figure shows only the blade, side and bottom boundaries. Also shown is the coordinate system, where x is in the chordwise direction, y is in the radial direction, and z is in the normal direction. The blade motion is counterclockwise.

All the boundary conditions are applied explicitly. At the wall a no-slip boundary condition is used for the viscous calculations. The Euler calculations use an extrapolation of the contravariant velocities at the surface. The density at the wall is determined by a zeroth-order extrapolation. The pressure along the body surface is calculated from the normal momentum relation (see, for example, Ref. 24). The total enery is then determined from the equation of state. To ensure continuity across the wake cut and also outboard of the blade tip, where the grid collapses to a singular plane because of H-grid topology, the flow quantities are determined by averaging the flow variables from both sides of the singular plane.

To capture the information in the wake region of the blade, a periodicity condition is used in the blade azimuthal direction that swaps the flow information, after interpolation, at the front and back boundaries of the cylindrical grid (see Fig. 1b). This is also done in an explicit manner. The flowfield of the entire rotor is then assembled by combining the flowfields of individual blades through a post-processing procedure. The radial inboard and far-field boundaries, as well as the upper boundary of the cylindrical mesh, are updated by means of a characteristic-type boundary condition procedure, although the Roe's upwinding used in the numerical procedure would otherwise treat the boundaries in a 1-D characteristic sense anyway. At the bottom boundary, the scene of the far-field wake, an approximate condition based on the normal velocity is used. For an outflow condition, all conserved flow quantities are extrapolated from the grid interior except for the energy, which is calculated by prescribing the free-stream pressure.

Although the helicopter rotor operates in a quiescent fluid atmospere, unlike in a fixed wing airplane, it induces significant velocities at large distances from the rotor. Therefore, specification of no flow at the inflow boundaries of a computational box, which is typically small for economy, poses a difficulty for the prediction methods. This no-flow condition at the farfield boundaries produces a "closed box" environment for the rotor where the flow recirculates within the computational "box". This problem, and the large time required for the initial transients to decay, were recognized by Kramer et al.[14,36], who used an approximate vortex-element solution to specify an initial condition that produced a flow through the farfield boundaries of the computational box.

A simpler and more economical alternative was introduced in Ref. 37 using the concepts of a three-dimensional point-sink and simple momentum theory as a guide. This is described in detail later in the text in Section 4.3. With this approach, the application of the above characteristic-type boundary condition produced a non-zero inflow at these boundaries. At the outflow boundary located at the farfield boundary below the rotor plane, the specification of the flow velocity is dictated from the momentum theory concepts, viz., the flow exit through a circular hole whose area is half that of the rotor disk, with an outflow velocity magnitude twice the momentum theory average value through the plane of the rotor. A characteristic-type numerical outflow boundary condition was applied across the exit plane by prescribing this outflow mass flux, and extrapolating the other flow variables from within. With this, the flow entered and exited smoothly the computational box. Most of the results presented in this study used a "box-type" boundary conditions approach mentioned earlier. After recognizing the importance of smooth vortex wake descent below the rotor disk, one calculation was repeated with the new boundary conditions.

4. RESULTS AND DISCUSSION

4.1 Model Two-Bladed Rotor in Hover

The test cases considered in this study correspond to the experimental model hover test conditions of Caradonna and Tung (Ref. 33). The experimental model consists of a two-bladed rigid rotor with rectangular-planform blades with no twist or taper. The blades are made of NACA 0012 airfoil sections with an aspect ratio of 6. Three experimental conditions were chosen from the data: 1) tip Mach number $M_{tip} = 0.44$, collective pitch $\theta_c = 8^\circ$, and the Reynolds number based on the blade tip speed and chord, Re = 1.92×10^6; 2) $M_{tip} = 0.877$, $\theta_c = 8^\circ$ and Re = 3.93×10^6; and 3) $M_{tip} = 0.794$, $\theta_c = 12^\circ$ and Re = 3.55×10^6.

4.1.1 Fine Grid Results

Surface pressures are shown in Figs. 2-4 for the three experimental conditions considered. These calculations were done on a fine grid consisting of nearly one million points. Figure 2 shows the surface pressures for the conditions of $M_{tip} = 0.44$, $\theta_c = 8^\circ$, and $Re = 1.92\times10^6$. In this figure, the present calculations are compared with the experimental data of Ref. 29 and the results from a previous Navier-Stokes calculation that used a simple wake model (Ref. 9). The present calculations agree well with the experimental data for all radial stations. There are some improvements in the results at $y/R = 0.50$ and 0.96 over the previous results from Ref. 9. It should be pointed out that the calculations of Ref. 9 used a O-O grid topology with nearly 700,000 grid points having a grid clustering similar to the present grid.

Figure 3 shows a comparison of surface pressures for the condition of $M_{tip} = 0.877$, $\theta_c = 8^\circ$ and $Re = 3.93\times10^6$. At this transonic flow condition, the present calculations show excellent agreement with the experimental data for all radial stations. In contrast to the calculations of Ref. 9, the present results show shock locations and shapes that are well captured due to the TVD upwinding used here. The inboard regions of the flow are also predicted more accurately; this indicates that the present computed wake is superior to the approximate wake model of Ref. 9.

Figure 4 shows a comparison of surface pressures for the condition of $M_{tip} = 0.794$, $\theta_c = 12^\circ$ and $Re = 3.55\times10^6$. Because of the high collective pitch, this case is more severe in terms of the shock strength and shock-induced boundary layer separation, even though the tip speed is slightly less than the previous case. The results show good agreement of the calculations with the experimental data, especially near the tip.

Figure 5 shows, through the surface particle flow, the extent of shock-induced boundary layer separation for the transonic cases discussed above. These are are created by releasing fluid particle tracers at one grid point above the surface and forcing them to stay in that plane. Figure 5a shows the details of this flow for the case of $M_{tip} = 0.877$ and $\theta_c = 8°$. The separation and reattachment locations are apparent in this figure. It is seen that this flow condition produces a mild shock-induced separation in the outboard part of the blade. In contrast, the shock-induced separation and viscous-inviscid interaction are much stronger for the case of $M_{tip} = 0.794$ and $\theta_c = 12°$. The surface particle flow pattern for this more severe case is shown in Fig. 5b. As seen, the extent of the separation is much larger for this flow condition than for the case of Fig. 5a. It is interesting, however, to note that the separation patterns in the tip region are approximately the same for these cases.

A general comparison of the present results with the experimental data can be made by examining the bound circulation distribution. Figure 6 shows such a plot of dimensionless circulation, $\Gamma/\Omega R^2$, as function of r/R for $\theta_c = 8°$ case and tip speeds of 0.44 and 0.877, corresponding to the data presented in Figs. 2-3. Here r is the radial distance from the rotation axis, R is the radius of the rotor, and Γ is the circulation, computed from the blade-element lift. Also shown are the integrated data from the experiments, which were reported to be essentially independent of tip speed. The calculations show a fair agreement with the experiments, except in the inboard part of the blade. This suggests that only the near-field effects of the tip vortex are captured as well as desired. There are two possible reasons for the poor agreement in the inboard part of the blade. First, the vortex wake becomes diffused in the far-field grid, so its induced effect is significantly diminished. Second, the inboard plane boundary condition may be indequate. In contrast to the experimental observation of the bound cirulation distribution, the present calculations show some dependency on the blade tip speed.

In the tip region the agreement is also not very good. This may be due to the bevel tip that is used in the computations compared to the square-tipped blade used in the experiments. Overall, however, the surface pressure distributions give the appearance of agreeing better with the experiments than the bound-circulation distribution. Relatively minor discrepancies in the pressure distributions near the leading edge, where the experimental transducer locations are relatively sparse, seem to translate into significant differences in the circulation distribution.

The chief advantage of the Navier-Stokes methods is to predict the separated flow in the tip region and the associated detailed structure of the tip vortex. The prediction of the overall shed-wake geometry is the most important step in the process of accurately modeling the complete hover flowfield. The ability to preserve this shed wake (including the vortex structure) from numerical diffusion is a more complex issue. The path of the tip vortex is more important to the outboard blade loading, whereas the ability to convect this shed wake without significant numerical diffusion strongly influences the inflow in the inboard parts of the blade.

Figure 7 shows a near-field view of the tip vortex particle path trajectory for the experimental conditions of $M_{tip} = 0.794$ and $\theta_c = 12°$ corresponding to Fig. 4. These trajectories are generated by releasing particle tracers in the vicinity of the tip of the blade on both surfaces and allowing them to move freely in time and space. It is apparent from this figure that the particles released right on the tip first group together and then get braided and stay in the vicinity of the core. As observed before (Ref. 35), the process of formation of the tip vortex involves braiding of fluid particles from both upper and lower surface of the blade. As the process of braiding of fluid particles from upper and lower surfaces continues, the tip vortex lifts up from the upper surface and rolls inboard in the downstream wake.

After identifying those fluid particles released in the vicinity of the blade tip that end up in the vortex core, fewer particles were released on the tip of the blade, in the proximity of the quarter-chord region, to trace out a trajectory of the tip vortex path. The free-wake trajectory showed the correct wake contraction and descent initially, up to about 360 deg. of vortex age. Subsequently, the wake trajectory continued to descend, but it expanded in size and eventually ended up in the recirculating flow. This problem, due to the "box-type" of farfield boundary condition used here, has been recently corrected by applying a point-sink and simple momentum theory concepts[37], as noted in the previous Section. With this the flow smoothly enters the computational box and leaves through the exit boundary. The calculated vortex trajectory with this new boundary conditions is shown in Fig. 8. The wake contraction and descent trajectories are shown in Fig. 8a. Figure 8b shows a very good comparison of the calculated nearfield trajectory with experiments[33]. Comparison of the calculated loads with the two methods of prescribing farfield boundary conditions showed only a 5% difference. However, the wake trajectory had the right characteristics of contraction and descent with the latter approach of specifying farfield boundary conditions.

4.1.2 Fine Grid *versus* Coarse Grid Results

The results presented in the preceeding sections were calculated on a fine grid of nearly one million points. The initial test calculations were made primarily on a coarse Navier-Stokes grid of 109×36×31 size. This grid was generated by removing every other point from the fine grid in all three directions. The outer dimensions of the grid and the grid topology are thus the same as for the previous fine grid.

Figure 9 shows a comparison of surface pressure distributions for the fine and coarse grids for the experimental condition of $M_{tip} = 0.877$, $\theta_c = 8°$ and $Re = 3.93 \times 10^6$. A general deterioration of the predicted surface pressure distributions can be seen for the coarse grids. In particular, the shocks are not as sharp as for the fine grid. The inboard results, not shown here for $y/R < 0.5$, had much poorer comparison. The tip vortex structure is also very diffused due to the poor grid density in this region. However, typical converged solutions with this coarse grid took only about one hour of CPU (central processor unit) time on the Cray-2 supercomputer, down from about 15 hours for the fine-grid cases.

4.1.3 Euler *versus* Navier-Stokes Results

As discussed earlier, there have been several attempts to capture rotor wakes using Euler methods (Refs. 14-17). The vortex formation in the tip region of a wing or a helicopter blade is a result of complex three-dimensional separated flow, and it is not clear how well the Euler methods are able to mimic viscous effects and separation to produce a vortex structure. Nevertheless, these Euler methods have been able to predict the pressure distributions and spanwise blade loading reasonably well for the outer part of the blade. Against this background, a limited comparison of surface pressures has been made of the Euler results with experiments and Navier-Stokes results. The Euler calculations were made by turning-off viscous terms in the TURNS code and using the same fine grid of about one million points used for viscous calculations. It should be noted that even for this fine viscous grid, the Euler version of the code did not exhibit any stability problems.

A typical comparison of the Euler results with experiments[33] and the Navier-Stokes results is presented in Fig. 10 for the test conditions of $M_{tip} = 0.877$, $\theta_c = 8°$, and $Re = 3.93\times10^6$. Because it neglects viscous-inviscid interaction, the Euler method overpredicts the shock wave strength and position (for $y/R \geq 0.75$). Otherwise, the Euler results are in good agreement with the Navier-Stokes results, which show mild shock-induced separation for this flow condition (see Fig. 5a). The overall agreement of surface pressures certainly does not reflect the details of the flow near the blade surface, especially the separation pattern and vortex wake details as predicted by the Navier-Stokes method. A cursory examination of surface particle tracers showed that the flow is completely attached everywhere. Although it is not clear how the tip vortex is formed with flow separation only at the edges of the blade, the prediction of reasonably accurate surface pressures indicate that the induced inflow through the rotor is approximately correct and that the tip vortex *strength* was accurately captured. The recent Euler calculations of Strawn[38] indicate that the Euler methods capture the strength and peak velocities of the wing tip vortex as well as any Navier-Stokes method (e. g., see Ref. 35), which is still underpredicting peak velocities and tight braiding of the vortex. In current study, the details of the wake structure for the Euler results need to be investigated further.

4.2 Four-Bladed UH-60A Blackhawk and BERP Rotors in Hover

Body conforming finite-difference grids are used, as before, for the long slender blades of the model UH-60A Blackhawk[39] and BERP[40] rotors. These blades, shown in planform in Fig. 11, have aspect ratios of 15.51 and 12.46 respectively. The blades are highly twisted and have twist distributions along their lengths as shown in Fig. 12. Because of the axial symmetry of the hovering rotor flowfield, a C-H grid topology is chosen, with C-type in the chordwise direction and H-type in the spanwise direction. The H-type spanwise topology creates a bevel edge for the square-tipped UH-60A blades. To adapt to the cylindrical flowfield of the rotor, three-dimensional grids are constructed for these blades by stacking and bending two-dimensional C-H grids so that they lie on the blade along the chord. Typical fine grids have nearly 940,000 points with 217 points in the chordwise direction and 71 and 61 points in the spanwise and normal directions, respectively. These grids have clustering in the leading and trailing edge regions as well as in the tip region. The grid lines are nearly orthogonal at the surface with a spacing of 0.00004 chord in the normal direction at the surface. The grid boundary is located at two rotor diameters away at the top and bottom boundaries and one radius beyond the tip in the spanwise direction. Coarse grids have been constructed by eliminating every other point in all three-directions; these typically have 120,000 points. Figure 13 shows a view of a typical grid for single blade constructed for the BERP blade. This view shows the grid boundaries and the details of grid clustering near the grid surface and in the tip region.

4.2.1 UH-60A Blackhawk Model Rotor

The four-bladed rotor considered here is the model Sikorsky UH-60A Black Hawk rotor[39]. The model blade geometry is identical to the full-scale rotor with the exception that the trim tabs have been omitted. Therefore, the UH-60A blades used here have approximately a constant chord along the entire span as shown in Fig. 1. They are made up of SC1095 airfoils except for $0.48 \leq r/R \leq 0.87$ where SC1095R8 airfoils are used. They have a swept-back planform in the tip region. A distinguishing feature of this rotor is the hook-like twist distribution in the tip region and an approximately linear twist inboard of $r/R \simeq 0.8$, as shown in Fig. 12. The solidity calculated for this rotor is 0.08393.

At the time these calculations were performed, much of the experimental information[39] for the UH-60A model rotor was restricted, including the collective pitch settings of the model rotor. In view of this, a representative tip speed ($M_{tip} = 0.628$) was selected, and a thrust condition was chosen for which the experimental Figure of Merit was reported to be essentially independent of thrust coefficient, i.e., near FM_{max}. A collective pitch setting of $\theta_c = 9°$ was tried out to match with the experimental data, but no attempt was made to model the elastic twist of the experimental model blades. Figure 14 presents the calculated surface pressure distributions at several radial stations along with the experimental results for $C_T/\sigma =$ 0.085, which approximately matches the calculated value of 0.084. The numerical results appear to be in general agreement with the data at all radial stations. The normalized sectional thrust distribution along the blade radius is also compared with the experimental data in Fig. 15. The overall agreement is fairly good. The calculated performance parameters for this rotor are presented along with the experimental data in Tables 1 and 2. As shown in Table 1, the calculated $C_Q/\sigma = 0.0068$ agrees well with the experimental data.

In the standard definition, the total power, C_Q, is the sum total of the induced and profile powers. It is also the sum total of the components of the integrated surface pressures $C_{Q_{pr}}$ and the surface skin friction C_{Q_s}. That is, $C_Q = C_{Q_i} + C_{Q_{prof}} \equiv C_{Q_{pr}} + C_{Q_s}$. As the integrated surface pressures include some of the profile power also, there is, of course, some degree of difficulty in isolating the actual induced power and profile powers according to their definitions. Also, the grid resolution in trailed wake precludes accurate determination of induced power from wake integration, but the induced power is approximately equal to $C_{Q_{pr}}$. In view of this, the second definition is used here for the results presented in these figures and in Tables 1 and 2.

In order to assess the importance of planform effects, flowfield calculations were made on an equivalent rectangular blade of identical airfoils and twist distribution as the UH-60A blade (shown as Twist1 in Fig. 12) for the above flow conditions of $M_{tip} = 0.628$, and $\theta_c = 9°$ and $Re = 2.75 \times 10^6$. The results are compared with the UH-60A blade in Fig. 15 in a plot of normalized sectional thrust coefficient (C_t) variation along the blade radius (r/R). Since the equivalent rectangular blade has the identical twist distribution as the UH-60A blade along its radius and has an unswept planform in the tip region, the differences seen with the UH-60A blade in Fig. 15 are only in this region. The sectional thrust for the equivalent blade has a smaller peak than the UH-60A blade and this peak occurs towards the tip of the blade as seen in Fig. 15. Although both of these blade tips are modeled by bevelled edges, because of the H-grid topology used in the radial direction, the UH-60A blade produces a relatively milder separation in this region than the equivalent rectangular blade with an unswept tip. Examination of the flow particle tracers released in the tip region for these blades showed that the tip vortex location for the UH-60A blade is slightly inboard of that seen for the equivalent rectangular blade. This observation is in general agreement with some previous studies of swept and unswept planforms with bevel-tips[33]. In terms of overall performance, the equivalent rectangular blade produces about 7% less thrust than the UH-60A blade, and the calculated Figure of Merit is about 5% lower. Tables 1 and 2 detail the performance parameters for these rotors.

Figure 16 shows the sectional thrust distribution along the radius of UH-60A blade for two thrust conditions corresponding to $\theta_c = 9°$ and 13° at $M_{tip} = 0.628$ and $Re = 2.75 \times 10^6$. The higher collective pitch produces higher thrust all along the blade radius and in all nearly 67% more thrust than the $\theta_c = 9°$ case, but the Figure of Merit is almost unchanged. The performance parameters for this thrust condition are also summarized in Tables 1 and 2. This high thrust condition also produces a much stronger tip vortex which is located more inboard than the $\theta_c = 9°$ case. The flow topology is very complicated for the upper surface of the blade at this high thrust condition with shock-induced boundary layer separation occuring over a large part of the blade, as shown by the surface particle tracers (skin friction lines) in Fig. 17. In contrast, as seen in the close-up view of the tip region in Fig. 18, the low thrust case ($\theta_c = 9°$) does not produce shock-induced flow separation. Both thrust conditions produce flow separation on the inboard parts of the blade as seen in Fig. 17, but the spanwise extent is, of course, greater at $\theta_c = 13°$. An examination of the Mach contours, on the upper surface of the blade at a plane outside the boundary layer as seen in the views of Fig. 19, for the $\theta_c = 13°$ case shows the extent and severity of the transonic flow with shock wave and shock induced separated flow around the swept part of the blade.

Two representative performance curves for the UH-60A rotor as calculated here for $M_{tip} = 0.628$ are shown in Fig. 20 and Fig. 21 along with the experimental data[6]. The details of the calculated results are as shown in Tables 1 and 2. Figure 20 shows a plot of power *vs* thrust for this rotor. Also shown in this are the induced power calculated using an empirical relation[41] and the ideal power. The present calculations for thrust and total power at $\theta_c = 9°$ show good agreement with experiments. Also, at this subcritical flow condition, the component of the power calculated from the pressure integration, $C_{Q_{pr}}$, is in good agreement with the empirically-estimated induced power[41]. The high thrust condition ($\theta_c = 13°$) for this rotor is apparently beyond the model test range. This high thrust condition produces severe shock-induced flow separation over a large part of the blade and a more severe flow separation pattern on the inboard part of the blade. As seen in Table 2, the skin friction contribution to the power has slightly decreased due to the reversed flow in the separated regions.

Figure 21 shows another rotor performance plot of Figure of Merit. As before, at the moderate thrust condition corresponding to $\theta_c = 9°$, the calculated Figure of Merit is in good agreement with experiments, including the empirical estimate of Figure of Merit that neglects viscous contribution (FM_i). It is interesting to note that the calculated Figure of Merit *including viscous effects* is almost the same at $\theta_c = 13°$ as at $\theta_c = 9°$, indicating that this particular measure of total hover performance seems to stay relatively uniform for this rotor, at least over this range of θ_c. On the other hand, the Figure of Merit calculated using only $C_{Q_{p_r}}$ from Table 2 shows a significantly lower value at this high thrust condition than at $\theta_c = 9°$. In other words, the calculations confirm that the relative contribution of skin friction drag to Figure of Merit is greater at lower thrust conditions.

In addition to the planform change study for this blade, a fictitious UH-60A blade having the same airfoils and planform but with a linear twist distribution in the tip region (Twist2 in Fig. 12) was considered to examine the importance of twist in this region on airloads. The sectional thrust distribution for this blade is shown in Fig. 15 along with results for the standard UH-60A blade and the equivalent rectangular UH-60A blade at the same test conditions as of Fig. 14. As seen in this figure, this blade generates almost identical thrust in the inboard region. There appears to be a small difference in the tip region, resulting in slightly less overall thrust coeficient than the UH-60A blade and with a 7% lower Figure of Merit, as shown in Table 1. As before, there is no flow separation on the blade except in the very tip region at this flow condition. An inspection of particle tracers released in the tip region from both sides of the blade indicates the location of tip vortex for this configuration to be slightly inboard of the UH-60A blade and has less tight braiding than the UH-60A blade tip vortex at a comparable blade location, although this blade also has a swept-tip planform.

4.2.2 BERP Rotor

The BERP rotor has an unorthodox planform shape with high-performance RAE airfoils.The spanwise twist distribution used in the present investigation and in Ref. 40 is shown in Fig. 12; it corresponds to a version of the BERP blade designed for good hover performance, rather than the version used on the Westland G-Lynx helicopter[42], and the total twist is approximately the same as the UH-60A. However, the innovative distribution of advanced RAE airfoils is used for the present BERP blade. As noted in Ref. 40, a distinguishing feature of the BERP blades is the enlarged-chord paddle-shaped planform, (see Fig. 11), with a leading-edge notch at approximately 80% span and a swept delta-wing-like planform in the tip region. The combination of unusual planform, high performance airfoils, and a balanced, spanwise distribution of airfoils has enabled the low-twist BERP rotor to achieve high performance in high-speed forward flight. In order to compare planform effects of the high-twist BERP blade with the UH-60A blade, two calculations are made for collective pitch of $\theta_c = 9°$ and 13° at a tip speed of $M_{tip} = 0.628$ and $Re = 2.95 \times 10^6$. The calculated rotor solidity is 0.10913.

Figure 22 shows sample surface pressures for the BERP rotor at different radial locations for the flow condition corresponding to $\theta_c = 13°$. Currently no experimental data are available for these flow conditions. However, these results and the surface pressures for $\theta_c = 9°$ appear to be in good qualitative agreement with the nonrotating blade results of Ref. 40. The spanwise circulation distribution is shown for this blade for $\theta_c = 9°$ in Fig. 23, along with UH-60A results at identical collective pitch and flow conditions. Since the BERP blade has a variable chord along its radius in contrast to the UH-60A blade, a comparison of bound circulation distribution appears to be more meaningful than the sectional thrust distribution. As seen in the comparison of Fig. 23, the combination of high performace airfoils, the leading-edge notch and increased area of the paddle part produces an increased thrust on most of the blade except for $r/R \leq 0.4$ where it is nearly the same as the UH-60A blade. The increased circulation seen at the inboard station (R_1) may be due to the deficiency in the inboard boundary condition.

Tables 1 and 2 summarize important hover performance results for this rotor. Figures 24 and 25 compare the sectional thrust and bound circulation distributions for the two thrust conditions. The high thrust condition produces about 64% more thrust at the expense of 101% more power compared to the moderate thrust condition of $\theta_c = 9°$. The sectional thrust distributions, shown in Fig. 24, has the same qualitative behavior as that of UH-60A blade. The bound circulation distribution of Fig. 25 appears to resemble qualitatively the sectional lift distribution of nonrotating BERP blade[40]. Of particular significance is the distribution in the vicinity of the notch. As observed for a nonrotating blade from both the wind tunnel tests and calculations[40], the present calculations also show a decrease and then an increase of sectional thrust distribution in this region for the $\theta_c = 13°$ case. In contrast, the thrust distribution for $\theta_c = 9°$ case does not show this behavior.

The surface particle tracer pictures of the BERP blade are shown in Fig. 26 for $\theta_c = 9°$ and 13°. For both thrust conditions, the flow stays attached on the paddle part of the blade. As seen in Fig. 26(a), the flow appears to be completely attached at the moderate thrust condition. The high thrust condition corresponding to $\theta_c = 13°$, however, produces a complicated vortical flow structure in the notch region as shown in Fig. 26(b) as well as in Fig. 27. Also, the strong supercritical flow at this high thrust condition produces a relatively small extent of shock-induced flow separation, confined only to the inboard of the notch region as seen in Fig. 15(b) and in Figs. 27(a) and 27(b). In contrast, as shown in Fig. 18(b), the UH-60A blade produces a severe shock induced flow separation over a large part of the blade for this flow condition. The extent and severity of the supercritical flow for the upper surface of the BERP blade in the notch region is highlighted in Fig. 27(c) by the pressure contour plot.

The nearly total absence of the flow separation on the paddle part of the BERP blade at the transonic flow condition, except in the very tip region where the tip vortex develops, has a favorable influence on the performance of the blade. Since these blades have high twists, both thrust conditions produce severe flow separation inboard. The extent of separation for the $\theta_c = 13°$ case, shown in Fig. 27(a), is much more massive than the $\theta_c = 9°$ case, as for the UH-60A blade (see Fig. 17).

A detailed comparison of surface particle traces for the UH-60A (Fig. 18) and BERP (Fig. 26) rotors in the outer part of the blades towards the tip reveals several noteworthy features, resulting from the different planforms and twist distributions in this region. The UH-60A blade has a hook-like twist distribution in the swept part near the tip while the BERP blade has constant twist with a large chord in the paddle part and a delta-wing like tapered tip. For the low thrust case, corresponding to $\theta_c = 9°$, both blades show completely attached flow except for the extreme tip region, and benign surface flow. In contrast, at the high thrust condition ($\theta_c = 13°$), they have totally different surface flow patterns. The UH-60A blade shows strong shock-induced separation and reattachment near the leading edge area on either side of the beginning of the sweep-back, whereas the BERP blade shows completely attached flow on the paddle-part except in the extreme tip region. The notch region has a complicated flow separation and vortical flow structure.

Figure 28 shows the details of the tip-vortex formation and roll-up process for the BERP blade. This flow visualization picture is generated by releasing unrestricted flow particle tracers in the tip region on both sides of the blade at different chordwise and spanwise locations and at different heights from the surface of the blade. The particles so released bunch-up and get braided over each other to form a distinct structure of concentrated vorticity. Such a structure represents the formation process of a concentrated tip vortex as seen in Fig. 28. While this tip vortex is still forming, it starts to roll-up and in the process stays distinctly above the wake vortex sheet. Once it leaves the surface, it convects with the wake. As this vortex wake convects, it contracts in size and descends with the flow. With the present nonadaptive, structured grids, the computed vortex structure is smeared, meaning the core of such a vortex is diffuse. But a line integration of the velocity vector along a closed path around such a line vortex reveals that the circulation is correctly captured in strength. This estimation has been verified at several locations along the vortex wake trajectory, viz., in the near wake and near the periodic boundaries. Because of the vortex diffusion, the farther the integration station from the blade the larger the size of the closed path is needed. In comparing the vortical flow structures of UH-60A and BERP blades corresponding to $\theta_c = 13°$, it was found that both have distinct but diffuse tip vortex structures. The notch area of the BERP blade produces a complex vortical structure, which is barely discernable in Fig. 28. Similary, the kink of the UH-60A blade also produces a very mild vortical structure for this flow condition.

4.3 Effect of Farfield Boundary Conditions

A difficult aspect of numerical prediction of hovering rotor flows is the prescription of farfield boundary conditions. In hover, if the specification of farfield boundary conditions is based on the quiescent flow outside of the computational box, then the flow into and out of the box will be zero. This creates a closed box environment for the rotor, with the flow inside the box recirculating when the rotor is spinning. In principle, this is precisely the environment in many hover test chambers. However, a large computational box of this size for the Navier-Stokes calculations is not cost effective and exceeds the memory limits of the present day supercomputers. Alternatively, with a smaller computational box around the rotor one should specify a non-zero flow farfield boundary conditions that will allow the flow to enter and exit the box without violating the conservation laws. Currently, no precise methods are available to specify such boundary conditions, although some schemes have been suggested[43]. The present calculations take a slighty different approach to specifying farfield conditions. A three-dimensional point sink, whose strength is determined from the thrust of the rotor by satisfying the mass flow conservation, is located at the axis of rotation in the plane of the rotor. The point sink pulls the flow from outside into the computational box with a velocity W_{in} given by

$$W_{in} = -\frac{M_{tip}}{4}\sqrt{\frac{C_T}{2}}\left(\frac{R}{d}\right)^2 \tag{13}$$

where $d^2 = x^2 + y^2 + z^2$. The velocity given by Eq. (13) represents the magnitude of the total incoming flow volocity. An appropriate component of this flow enters the computational box from each boundary except through an exit plane on the lower boundary. Assuming the far-field exit velocity at this exit plane to be uniform, its magnitude can be determined from 1-D momentum theory concepts by relating the outflow momentum to the rotor thrust by

$$W_e = -M_{tip}\sqrt{\frac{C_T}{2}} \tag{14}$$

A characteristic-type outflow boundary condition is specified by prescribing this w-velocity, W_e, across the exit plane whose area is half of the rotor disk. The other four quantities are extrapolated from within. Prescription of this new boundary condition procedure enables the flow to enter and exit smoothly the computational box. A schematic of this new farfield boundary of the computational box is shown in Fig. 29.

Using the above approach of specifying the farfield boundary conditions, calculations were repeated for the UH-60A blade at flow conditions of $M_{tip} = 0.628$, $\theta_c = 9°$ and $Re = 2.75 \times 10^6$. Figure 30 shows the sectional thrust distribution calculated with the new farfield boundary condition compared with old boundary conditions results along with experiments. Although there is general agreement of the overall results in this plot, there are small differences near the kink and in the tip region that appear to be due to differences in the wake trajectory. The performance parameters for this new condition are shown in Table 1. The thrust and power values are about 3% more than those obtained with the old boundary conditions.

The important test of this new boundary condition is the behavior of the captured wake trajectory. Fluid particle tracers that reside within the core of the tip vortex, such as shown in Fig. 28, were identified and monitored as the wake evolved. Figure 31 shows the views of vortical wake contraction and descent calculated with this new procedure. The nearfield trajectory of this wake, for both contraction and descent, appears to be in reasonable agreement with the experiments, as shown in Fig. 31c. The previous calculations, for the same computational box with old boundary conditions, produced a wake trajectory that was accurate only up to about 180° of vortex age (azimuthal travel). Subsequently, the wake trajectory continued to descend but expanded in size, from its previous size at 180° azimuth, and eventually got caught in the recirculating flow. With the new farfield boundary conditions, the entire wake exits smoothly at the bottom boundary, as seen in Fig. 31.

4.4 Model Two-Bladed Rotor in Forward Flight

In this section, instantaneous surface pressures of a two-bladed rotor in forward flight, calculated using the TURNS code, are presented and compared with experimental data for rotor-alone configuration[44,45]. Several test conditions from among many model rotor experiments are selected for computations. The hovering rotor calculations described in the previous sections were done in the blade-fixed coordinates system. In contrast, the forward flight calculations are done in the inertial coordinate system. The TURNS code switches from one-system to the other by choosing the proper input for the grid motion. To validate the TURNS code for forward flight motion, calculations are done for a nonlifting rotor in forward flight at both subcritical and supercritical flow conditions. This solution is then used as the baseline solution for calculating a lifting, three-dimensional, unsteady, blade-vortex interaction (BVI) flowfield.

4.4.1 Rotor in Forward Flight

The two-bladed rigid rotor considered here for flowfield calculation is a nonlifting configuration that was tested in a wind tunnel by Caradonna et al. [44]. Several test calculations have been performed[46,47] corresponding to the model rotor test conditions[44,45]. Typical results of instantaneous surface pressures for rotor-alone case are presented in Figs. 32 and 33 for the conditions of $M_{tip} = 0.6$ and 0.8, respectively, and an advance ratio $\mu = 0.2$. The results for subcritical case of Fig. 32 shows that the rotor flowfield behaves like a two-dimensional flow and the surface pressures at different azimuthal location of the rotor all look alike. The unsteady time-lag effects and the three-dimensional effects are nearly absent. In contrast, the surface pressures shown for various azimuthal locations of rotor in Fig. 33, for the supercritical flow condition, appears to behave differently. The presence of transonic shock wave on the advancing cycle produces strong time-lag effects and accentuates three-dimensionality of the flow (see also Ref. 46). The instantaneous surface pressures for subcritical and superctical cases are in good agreement with experimental data. The numerical method captures correctly the evolution of the unsteady flow in forward flight, atleast for this nonlifing configuration.

4.4.2 Three-Dimensional Parallel Blade-Vortex Interaction

Using this baseline solution, a vortex fitting technique[48,49] is used to introduce the convecting vortex flowfield in to the rotor flowfield and the evolution of the interactional flowfield is then calculated. The interacting line vortex lies along y-axis and is located at $x_o = 0.0$ and $z_o = -0.4$ where x, y, and z are the physical space coordinates. These are respectively along the chord of the blade, along the radius of the blade and normal to the blade surface. Both parallel and oblique blade-vortex interactions have been calculated for several tip Mach numbers. In contrast to the subcritical flow conditions, the presence of shock waves under supercritical flow conditions appears to enhance the flow unsteadiness and three-dimensionality. A typical result of instantaneous surface pressure distribution for a parallel blade-vortex interaction, calculated on a coarse grid, is shown in Fig. 34 along with comparison to experimental data. For the azimuthal position of the blade of $\psi = 174.5°$, the blade-vortex interaction appears to have peaked. As seen, the instantaneous surface pressures are in fair agreement with experiments. Although not shown here, the oblique BVI occurs over a larger azimuthal travel of the blade. The interaction begins in the first quadrant and completes only towards the end of second quadrant.

4.5 High-Speed Impulsive Noise in Hover and Forward Flight

The capability of TURNS code in simulataneously calculating the aerodynamics and aeroacoustics in one single calculation is demonstrated here. The acoustics calculations were performed by Baeder[23]. For calculating the HSI noise, the rotor blade considered is from the experiments of Ref. 50. The blade is a 1/7th scale model of a UH-1H main rotor with untwisted rectangular blades of NACA 0012 airfoil section. This rotor has an aspect ratio of 13.7. The computations were done on a 49x37x55 grid (half plane) with grid boundary located at 48 chords away from the center of rotation. The first case examined is for $M_{tip} = 0.90$ and $Re = 1.6 \times 10^6$ for which the flow is just delocalized. The pressure time histories at 3.09 rotor radii are shown in Fig. 35a. The predicted amplitude of the negative peak pressure, as well as the wave shape, agree well with the experiments. Similar agreement occurs at other locations also. For this weak shock case, the Euler and Navier-Stokes results are nearly identical. In contrast to the present CFD method, studies using the acoustic analogy method[22] or the nonlinear Kirchoff formulation[51], with aerodynamic input from either small disturbance code or full potential code, underpredict the negative peak pressure.

If M_{tip} is increased to 0.95, the shock on the surface of the blade becomes very strong. Examination of the pressure contours, in a plane normal to the blade surface at 98% of the span, indicates that the Navier-Stokes results show the shock location slightly upstream and more smeared at its root than the Euler results. However, away from the blade surface the shock location and strength appears to be nearly identical with that of Euler results. The resulting pressure time histories at 3.09 rotor radii are shown in Fig. 35b. Again the agreement with experiment is excellent. The reason for the overall good agreement of the Euler results with the Navier-Stokes results is because HSI noise is caused by the (summation of the) large gradients across the whole flowfield, and not just the portion of the shock that intersects the blade surface.

For calculating the HSI and its propagation in forward flight, the OLS rotor blade of an AH-1 helicopter is selected due to its simple geometry of a rectangular planform with constant thickness. The maximum thickness of the airfoil is 9.71% chord and the rotor blade has an aspect ratio of 9.22. Acoustic data are available for full-scale and model OLS blades[52]. For the calcuations reported here the twist of the blade is neglected and the tip path plane angle and collective pitch are set to zero. The mesh consists of 73x55x55 points with 55x19 points on the blade, covering the upper half plane of the whole flowfield.

The test case examined is for $M_{tip} = 0.665$, an advance ratio $\mu = 0.348$, and $Re = 2.17\text{x}10^6$. The flowfield is delocalized[22] for a short period of time. The time histories of the pressure pulse at 1.8 rotor diameters directly in front of the blade are shown in Fig. 36. Non-linear effects manifest themselves in the steeper compression wave and in the magnitude of the pulse; calculations using linear theory underpredicts the negative peak pressure. A detailed examination of the Euler and Navier-Stokes solutions reveals strong directivity. The propagated noise to the sides of the blade is relatively small and non-impulsive. Upstream of the rotor, however, the propagated noise is very large and impulsive. Similar trends have been observed in the experiments. Further examination of the pressure contours in the plane of the rotor shows the growth and decay of the supersonic pocket on the rotor blade surface, the initial separation of the acoustic wave from the aerodynamic field and the propagation of the acoustic wave to the far-field. It is currently impossible to obtain such detailed information from experiments.

5. CONCLUSIONS

A free-wake Euler and Navier-Stokes CFD method, called TURNS, has been developed for helicopter applications. This implicit, completely upwind, finite-difference numerical procedure of structured-grids is applied to calculate the viscous flowfields of helicopter in hover, forward flight, and blade-vortex interaction (BVI) flowfield of an advancing rotor interacting with a concentrated line vortex. The hovering flowfields of two-bladed and four-bladed rotors are calculated using cylindrical C-H grid topology and body-fixed coordinates. The vortex wake and its induced effects are captured as a part of the overall numerical solution without specifying any wake structure or position; that is, without any wake modeling. The use of periodic boundary conditions with a single blade enables the construction of a full helicopter rotor flowfield and thus saves computational time. The captured vortical structure is smeared due to grid coarseness. Nevertheless, the induced flow in the plane of the rotor and the near-field wake trajectory are computed fairly accurately, and the calculated surface pressures on the blade, thrust, power, and Figure of Merit are in good agreement with experiments. The wake trajectory is significantly improved when new farfield boundary conditions are introduced.

Of the two flow conditions considered for the two four-bladed rotors, the BERP rotor produces more thrust, and the calculated Figure of Merit remains approximately constant as C_T increases. Results for the UH-60A and BERP blades at transonic high-thrust conditions indicate that the BERP blade produces milder shock-induced separation than the UH-60A blade. The BERP blade also shows a more tightly braided tip vortex structure compared to the UH-60A blade. Further improvements are needed, but the good comparison of the UH-60A rotor performance calculations with experiments indicates that this free-wake Navier-Stokes CFD capability is promising as a tool for analyzing the properties of new and exotic blade shapes whose properties are not known *a priori*. The numerical method is fairly efficient and runs at 145 MFLOPS on the Cray-YMP supercomputer. The quasi-steady Navier-Stokes calculations presented here for coarse and fine grids took approximately 1 hour and 15 hours of CPU time, respectively, on the Cray-2 supercomputer.

Overall, the study demonstrates the capabilities of TURNS code in calculating the helicopter rotor aerodynamic flowfields, including the acoustics (high speed impulsive noise), in both hover and forward flight. The aerodynamics and acoustics informations can be obtained in one single calculation. The agreement with experiments is very encouraging, demonstrating the ability of the solution scheme to capture the flowfield and acoustic details that are hard to obtain from experiments.

PART II

6. DYNAMIC STALL OF AN OSCILLATING WING

6. INTRODUCTION

The term "dynamic stall" is often referred to the unsteady separation and stall phenomena of aerodynamic bodies or lifting surfaces that are forced to execute time-dependent (unsteady) motion, oscillatory or otherwise. It is a complex fluid dynamic phenomenon of practical importance and occurs on manuvering flight vehicles, retreating blades of helicopter rotors, wind turbine blades, and compressor cascades. The dynamic stall phenomena often leads to the initiation of stall flutter. As summarized in extensive reviews by McCroskey[53,54] and Carr[55], the majority of the work on this fundamental fluid dynamic problem is devoted to the case of airfoils oscillating with moderate amplitude in a uniform freestream. When the airfoil reaches fairly high angles of attack during the oscillatory cycle, past the static stall angle limit, the generated unsteady flowfield is characterized by massive unsteady separation and large-scale vortical structures. One important difference between this flowfield structure and that generated by the static stall is the large hysteresis in the unsteady separation and reattachment. The maximum values of lift, drag, and pitching-moment coefficients can greatly exceed their static counterparts, and not even the qualitative behavior of these can be reproduced by neglecting the unsteady motion of the body surface (airfoil or wing).

One of the reasons why the flowfield associated with dynamic stall is more difficult to analyze than the static stall is of its dependence on a much larger number of parameters. The important ones are the airfoil shape, Mach number, reduced frequency or pitch rate, amplitude of oscillations, type of motion (ramp or oscillatory), Reynolds number, three-dimensional effects, and wind tunnel effects. To date most of the research in this area has been performed for the simpler model problems of two-dimensional oscillating airfoils. Most of what is understood about the characteristics and various regimes of dynamic stall has essentially come from experimental observations, which are mostly two-dimensional. Attempts to calculate the quantitative effects of dynamic stall abound in the literature (Refs. 55-63). The purely laminar case is assumed to have been solved (Refs. 57-58), although recent studies[64] show small-scale details of possible importance. However, the laminar calculations have not been validated with experiments (for the lack of availability of purely laminar data). The flows with turbulent boundary layer have not yet been successfully solved.

The weak link in the computational/theoretical methods for an accurate simulation of these unsteady flowfields is the turbulence modeling. Of course, the transitional nature of the boundary layer is almost always neglected; instead the flow is approximated to be either completely laminar or completely turbulent on the airfoil surface. Such an approximation may not be correct if the flowfield is dominated by leading-edge separation. In any case, a reasonably good turbulence model must be used to accurately calculate the nonequilibrium nature of the separated turbulent boundary layer and the associated unsteady time-lag features. Simple eddy viscosity models, like the Baldwin-Lomax model[26], have been found to be inadequate. The objective of this investigation is to identify a reasonably accurate and robust turbulence model. Several turbulence models that are in use in most Computational

Fluid Dynamics (CFD) codes are considered for evaluation. It should be noted that Refs. 59-62 have considered a similar exercise.

The five turbulence models considered are the Baldwin-Lomax (B-L) algebraic model[26], the Renormalization Group (RNG) based algebraic model[65], the half-equation Johnson-King (J-K) model[66,67], the one-equation Baldwin-Barth (B-B) model[68], and the one-equation Spalart-Allmaras (S-A) model[69]. The performance of these models is evaluated for accuracy and robustness by using them to calculate the unsteady, two-dimensional, viscous, flowfields of an oscillating NACA 0015 wing. The accuracy of the calculated results is determined by comparison with the oscillating wing experimental data[70] measured at the U. S. Army Aeroflightdynamics Directorate at NASA Ames Research Center. The eventual objective is to use the turbulence model that calculates the unsteady boundary layer and flow physics accurately to simulate the three-dimensional dynamic stall of oscillating wing and the retreating blade stall of a helicopter rotor blade.

7. GOVERNING EQUATIONS AND NUMERICAL SCHEME

The governing equations considered are the Reynolds-averaged, two-dimensional, Navier-Stokes equations in strong conservation-law form. These can be written in a generalized body-conforming curvilinear coordinate system (ξ, η, τ) as follows[71] :

$$\partial_\tau \widehat{\mathbf{Q}} + \partial_\xi \widehat{\mathbf{E}} + \partial_\eta \widehat{\mathbf{F}} = \frac{1}{Re}(\partial_\xi \widehat{\mathbf{R}} + \partial_\eta \widehat{\mathbf{S}}) \tag{15}$$

where $\xi = \xi(x,y,t)$, $\eta = \eta(x,y,t)$, and $\tau = t$. Here (x,y,t) is the body-fixed coordinate system; x is along the chord and y is normal to the chord. Also, $\widehat{Q}$ is the vector of conserved flow variables; $\widehat{E}$ and $\widehat{F}$ are the inviscid flux vectors. These are given by

$$\widehat{\mathbf{Q}} = \frac{1}{J}\begin{pmatrix} \rho \\ \rho u \\ \rho v \\ e \end{pmatrix}, \quad \widehat{\mathbf{E}} = \frac{1}{J}\begin{pmatrix} \rho U \\ \rho u U + \xi_x p \\ \rho v U + \xi_y p \\ (e+p)U - \xi_t p \end{pmatrix},$$

$$\widehat{\mathbf{F}} = \frac{1}{J}\begin{pmatrix} \rho V \\ \rho u V + \eta_x p \\ \rho v V + \eta_y p \\ (e+p)V - \eta_t p \end{pmatrix}$$

The vectors $\widehat{\mathbf{R}}$ and $\widehat{\mathbf{S}}$ are the viscous stress vectors in the ζ and η directions, respectively. The viscous terms are retained in both directions to resolve massive separation and these are considered in the thin layer approximation. For example, the vector in the η-direction is written as

$$\widehat{\mathbf{S}} = \frac{1}{J}\begin{pmatrix} 0 \\ \mu m_1 u_\eta + (\mu/3) m_2 \eta_x \\ \mu m_1 v_\eta + (\mu/3) m_2 \eta_y \\ \mu m_1 m_3 + (\mu/3) m_2 m_4 \end{pmatrix}$$

Here

$$\begin{aligned} m_1 &= \eta_x^2 + \eta_y^2 \\ m_2 &= \eta_x u_\eta + \eta_y v_\eta \\ m_3 &= \left(\frac{1}{2}\right)\frac{\partial}{\partial}(u^2 + v^2)/2 + \frac{1}{Pr(\gamma-1)}\left(\frac{\partial a^2}{\partial \eta}\right) \\ m_4 &= \eta_x u + \eta_y v \end{aligned}$$

where U and V are the contravariant velocity components and ξ_x, ξ_y, η_x, η_y, ξ_t, and η_t are the coordinate transformation matrics[71].

In the above equations all geometrical dimensions are normalized with the airfoil chord length, c, the Cartesian velocity components, u and v are scaled by the freestream sound speed a_∞, and the time t is normalized as tc/a_∞; p is the static pressure normalized by γa_∞; ρ is the density normalized by free-stream density ρ_∞; e is the total energy per unit volume normalized with $\rho_\infty a_\infty^2$; a is the speed of sound; Re is the Reynolds number; Pr is the Prandtl number; γ is the ratio of specific heats; and μ is the viscosity coefficient normalized by its free-stream value. The pressure is related to the density and total energy through the equation of state for an ideal gas,

$$p = (\gamma - 1)\left[e - \rho(u^2 + v^2)/2\right] \tag{16}$$

The governing equations are written in conservation law form for an inertial reference frame (x_o, y_o, t). Let $\vec{\mathbf{r}}_o(t)$, $\vec{\mathbf{v}}_o(t)$, and $\vec{\Omega}(t)$ be the position vector of the origin, the velocity, and the angular velocity of a non–inertial frame (x, y) relative to the inertial frame (x_o, y_o). The velocity $\vec{\mathbf{v}}$ of the non–inertial frame relative to the inertial frame is:

$$\vec{\mathbf{v}} = \vec{\mathbf{v}}_o(t) + \vec{\Omega}(t) \times \left[\vec{\mathbf{r}} - \vec{\mathbf{r}}_o(t)\right] = \dot{\vec{\mathbf{r}}}_o(t)$$

When the motion is reduced to pure rotation then $\vec{\mathbf{v}}_o(t) = 0$. Positioning the origin of the non–inertial frame at the origin of the inertial frame, for rotational type of motion, makes $\vec{\mathbf{r}}_o(t) = 0$. Therefore, for this restricted class of motion the velocity $\vec{\mathbf{v}}$ is expressed as, $\vec{\mathbf{v}} = \vec{\Omega}(t) \times \vec{\mathbf{r}}(t)$. Further simplification is obtained when the body rotates around only one coordinate axis. For example, when the body rotates about the y–axis $\vec{\Omega}(t) = (0, \omega_y)$ then $\vec{\mathbf{v}} = \omega_y \vec{e}_x - \omega_y \vec{e}_y$. Here $\vec{e}_x$ and $\vec{e}_y$ are the unit normals along $x-$ and y-directions, respectively. The rotational speed ω_y is obtained from the type of motion prescribed as $\omega_y = d\alpha/dt$. The reduced frequency parameter is defined as either $k = \dot{\alpha}c/2U_\infty$, or $\pi fc/U_\infty$ where f is the frequency of oscillation and U_∞ is the free-stream velocity. Then $\omega_y = \alpha_1(2kU_\infty/c)cos[(2kU_\infty/c)t]$ for $\alpha(t) = \alpha_0 + \alpha_1 sin(Kt)$ where α_0 is the mean angle of oscillation, α_1 is the amplitude of the pitch, and $K = 2kU_\infty/c$.

The numerical scheme uses a factored, finite-difference Beam-Warming implicit algorithm[71]. The viscous terms are retained in both ξ- and η–directions and in a thin layer approximation form. The viscous terms are treated implicitly. The approximately factored algorithm is given by

$$\begin{aligned}
&\Big\{I + h\big[\delta_\xi \widehat{\mathbf{A}}^n_{i,j} - Re^{-1}\delta_\xi \widehat{\mathbf{M}}^n_{i,j} + (D_{imp})_i\big]\Big\}^p \times \\
&\Big\{I + h\big[\delta_\eta \widehat{\mathbf{B}}^n_{i,j} - Re^{-1}\delta_\eta \widehat{\mathbf{N}}^n_{i,j} + (D_{imp})_j\big]\Big\}^p \Delta\widehat{Q}^p_{i,j} \\
&\qquad = -\Delta t\Big\{\widehat{Q}^p_{i,j} - \widehat{Q}^n_{i,j} + \big[\delta_\xi \widehat{E}^n_{i,j} + \delta_\eta \widehat{F}^n_{i,j}\big] \\
&\qquad\qquad - \big[\delta_\xi \widehat{R}^n_{i,j} + \delta_\eta \widehat{S}^n_{i,j}\big] + \epsilon_e D^n_{i,j}\Big\}
\end{aligned} \tag{17}$$

Here δ is the central difference operator and h is the time-step that determines whether the algorithm is first- or second-order time accurate . The time index is denoted by n and $\Delta\widehat{Q}^n_{i,j} = (\widehat{Q}^{n+1}_{i,j} - \widehat{Q}^n_{i,j})$. The explicit inviscid fluxes are given by $\widehat{E}_{i,j}$, $\widehat{F}_{i,j}$ and $\widehat{R}_{i,j}$, $\widehat{S}_{i,j}$ are the explicit viscous fluxes. The quantities $\widehat{A}, \widehat{B}$, $\widehat{M}$ and $\widehat{N}$ in Eq. (17) are flux Jacobian matrices obtained from the linearization of the left hand side. D_{imp} and $\epsilon_e D$ are the implicit and explicit dissipation terms. A Jameson–type[72], blended second and fourth order, numerical dissipation based on the computed pressure field is used to suppress high frequency numerical oscillations. For subsonic shock free solutions only the fourth-order dissipation is used, while for transonic solutions the second-order dissipation is activated in the vicinity of shocks where the pressure jump has steep gradients. Both the implicit and explicit dissipation are scaled by the spectral radius. For the accuracy of calculated solutions, the added dissipation coefficients are kept as small as possible.

The errors introduced by the linearization and approximate factorization of the left hand side of the numerical algorithm may be minimized by performing Newton subiterations at each time-step during the unsteady calculations. The approximation to $\tilde{Q}^{n+1}$ at each subiteration is the quantity $\tilde{Q}^p$. When $p \geq 2$, during a given level of subiteration to convergence, $\tilde{Q}^p = \tilde{Q}^{n+1}$, but when $p = 1$ and no subiterations are performed, then $\tilde{Q}^p = \tilde{Q}^n$, and $\tilde{Q}^{p+1} = \tilde{Q}^{n+1}$. In the present study, the numerical experiments have demonstrated that because of the small time-steps used, the Newton subiterations are not required. It was also found that the two time-level numerical scheme does not increase the accuracy of the unsteady calculations.

In the normal practice of the thin layer approximation for viscous terms, only the terms in the normal direction $(\widehat{S})$ are retained because of the large flow gradients in that direction. Retaining the viscous terms for both the directions $(\widehat{R}, \widehat{S})$, in the present study, was found to be slightly beneficial for the deep-stall cases, perhaps because of massive separation. For the light-stall case, however, the calculations performed retaing the viscous terms for the η direction alone and terms for both the ξ and η directions showed very little difference between the solutions. Therefore, the light-stall calculations are performed by retaining the viscous terms only in the η direction. The computational cost was not significantly increased for doing this for both the directions. Also, numerical experiments have demonstrated that implicit treatment of the streamwise viscous term, $\widehat{\mathbf{M}}$ of Eq. (17), does not contribute to the accuracy of the solution but results in increased computational cost. Therefore, implicit treatment of the streamwise viscous term is not used in the present study.

Body-fitted C-type computational grids are used in all calculations. These are generated using a hyperbolic grid generator. The grids are clustered at the body surface in the normal direction, leading edge, and trailing edge regions. The spacing of the first grid point at the surface in the normal direction is 0.00002 chord and the grid boundaries are located at 15 chords in all directions. Although most of the results presented are generated using one grid of size 361x71 with 271 points on the airfoil in the chordwise direction and the remaing in the wake region, three other grids of size 181x71, 671x71, and 361x141 have also been used to study the effect of grid size on the solution accuracy.

The orientation of the non–inertial frame with respect to the inertial frame is changing at each instant of time. Therefore, after each time-step the grid is moved to the new location and all metrics are recomputed.

Boundary conditions are updated explicitly. All flows are computed at one subsonic free stream speed. For subsonic inflow-outflow, the flow variables at the boundaries are evaluated using one-dimensional Riemann invariant extrapolation. At the inflow boundary there is one incoming and three outgoing characteristics. Therefore, three variables, the density, the normal velocity, and the pressure are specified and the fourth variable, the axial velocity is extrapolated from the interior. At the outflow boundary there are one incoming and three outgoing characteristics and only one quantity, the pressure, is specified while the others are extrapolated from the interior. For the density, a simple first–order extrapolation is used. On the body surface a nonslip condition is applied for the velocities, viz., the contravariant velocities in the body-fixed coordinates are set to zero. It should be noted that the surface velocity is non-zero because of the body motion through the unsteady metrics. The boundary layer approximation is used to obtain the surface pressures as $p_{i,1} = p_{i,2}$. For C–type grids used in this study averaging of the flow variables at the wake cut is used.

8. TURBULENCE MODELS

All flows computed in this study are assumed to have fully turbulent boundary layer on both the upper and lower surface of the airfoil by neglecting the laminar and trasitional boundary layer. In the experiments of Piziali[70], with which all present calculations are compared, the boundary layer is tripped in the leading-edge region. For turbulent viscous flows, the non-dimensional viscosity μ in the viscous flux vectors is calculated as the sum total of the laminar and turbulent viscosity. It is the determination of this turbulent viscosity that is of special significance and the focal point of this present study. As mentioned before, five different turbulence models are used for calculating turbulent eddy viscosity and the unsteady flowfield of an NACA 0015 oscillating wing. The results are used to evaluate their performance. The details of how these models are developed are described elsewhere[26,65-69]. The following paragraphs describe briefly the salient features of these models and the specific versions used in the present investigation.

8.1 Baldwin-Lomax (B-L) model

This is a two-layer, zero-equation model. It is patterned after Cebeci-Smith model[73] and introduces a modification that eliminates the need to search for the edge of the boundary layer to determine length scale. It is the most commonly used turbulence model available in most of the CFD codes. Its strength and weakness are well known in CFD community; it predicts accurately the steady flows with little or no separation and fares poorly if there is large separation, either shock-induced or otherwise. It uses an inner and outer layer formulation for determining the turbulent viscosity with a smooth transition that spreads over the two regions. It uses a classical mixing-length hypothesis for the inner layer with a van Driest damping function to force the eddy viscosity at the wall to zero. In the outer layer, the length scale is fixed by the location where the product of distance from the solid wall and vorticity reaches a maximum in the boundary layer. The Klebanoff's intermittency factor is used to drive the eddy viscosity to zero in the outer flow away from the wall. Some of the constants of the theory are determined by correlating with experimental data. The details of the theory are described in Ref. 26.

8.2 RNG model

Another algebraic eddy viscosity model was proposed recently, for the closure of the Reynolds averaged Navier-Stokes equations, based on the Renormalization Group (RNG) theory of turbulence[65]. The algebraic model, although free from uncertainties related to the experimental determination of empirical modeling constants, still requires specification of an integral length-scale of turbulence, similar to the B-L model, which reduces the generality of the model. In this model the integral scale is assumed to be proportional to the boundary layer thickness δ, and the eddy viscosity is obtained as in Ref. 65 from

$$\nu = \nu_l \left[1 + H \left\{ \frac{\widehat{a}}{\nu_l{}^3} \phi \left(\frac{1}{y} + \frac{1}{0.225\delta} \right)^{-4} - C_c \right\} \right]^{\frac{1}{3}} \tag{18}$$

where $\nu = \nu_t + \nu_l$, the subscripts t and l refer to the turbulent and laminar components, respectively and δ is the boundary layer thickness. It is determined from $\delta = 1.2\, y_{1/2}$ where $y_{1/2}$ is the normal distance from the wall at which the vorticity function $F(y)$ (see Ref. 26) attains its half amplitude[67]. H is the Heaviside step function and ϕ is the dissipation rate, it is determined by assuming production equals dissipation for equilibrium flows. The parameter $\widehat{a} = 0.0192$ corresponding to the von Karman constant $\kappa = 0.372$ and the parameter $C_c = 75$. The turbulent eddy viscosity is then obtained by solving Eq. (18) at every point in the computational domain. In estimating the eddy viscosity with this model in this study, the model is applied only to the suction side of the airfoil (upper surface) while the pressure side (having attached flow) and wake regions are computed with the B-L model. Application of the model to both the upper and lower surfaces essentially gave the same results as the one obtained by applying for only uppper surface; so the latter was used.

8.3 Johnson-King (J-K) model

The above two models, viz., the B-L and RNG models, are termed equilibrium models meaning that the eddy viscosity instantaneously adjusts to the local flow without any history effects. The next three models presented are called non-equilibrium models in which the calculated eddy visocity accounts for the upstream history of the flow.

From the time Johnson and King first introduced their half-equation turbulence model[66], there have been several modifications and/or enhancements to improve their original model for separated flows[61]. In the present application to unsteady flows, the original version of this model is used[66] and is briefly described in the following paragraphs.

The Johnson–King model[66] takes into account the convection and diffusion effects on the Reynolds shear stress $\overline{-u'w'}$ in the streamwise direction. The eddy viscosity is given by

$$\nu_t = \nu_{t_o} \left[1 - exp(-\frac{\nu_{t_i}}{\nu_{t_o}}) \right] \tag{19}$$

where ν_{t_i}, ν_{t_o} describe the eddy viscosity variation in the inner and outer part of the boundary layer. The inner eddy viscosity is computed as

$$\begin{aligned} \nu_{t_i} &= D^2 \kappa y \sqrt{(\overline{-u'w'})_{max}} \\ D &= 1 - e^{-(y/A^+)} \end{aligned} \tag{20}$$

where the constant $A^+ = 15$. The outer eddy viscosity is given by

$$\nu_{t_o} = \sigma(x)\cdot[0.0168 U_e \delta^* \gamma] \tag{21}$$

where δ^* is the boundary layer displacement thickness, γ is the Klebanoff's intermittency function given by $\gamma = \left[1+5.5(\frac{y}{\delta})^6\right]^{-1}$, and $\sigma(x)$ is obtained from the solution of an ordinary differential equation which describes the development of $\overline{-u'w'}|_{max}$ along the path of the maximum shear stress. The effects of convection and diffusion on the Reynolds shear stress development are accounted from the solution of the following ordinary differential equation

$$\begin{aligned} \frac{dg}{dx} = \frac{a_1}{2\bar{u}_m L_m}\Bigg\{\left(1-\frac{g}{g_{eq}}\right)+ \\ \frac{C_{dif}L_m}{a_1\delta[0.7-(\frac{y}{\delta})_m]}|1-\sqrt{\frac{\nu_{t_o}}{\nu_{t_o,eq}}}|\Bigg\} \end{aligned} \tag{22}$$

Here C_{dif} and a_1 are modeling constants $\bar{u}_m$ is the maximum average mean velocity and

$$\begin{aligned} g &= \left[\overline{-u'w'}_m\right]^{-1/2}, and \\ g_{eq} &= \left[(\overline{-u'w'})_{m,eq}\right]^{-1/2} \end{aligned}$$

where L_m is the dissipation length evaluated as

$$\begin{aligned} L_m =&0.40y \quad for \quad y_m/\delta \le 0.225 \\ L_m =&0.09\delta \quad for \quad y_m/\delta \ge 0.225 \end{aligned} \tag{23}$$

The boundary layer thickness, δ, is determined in the same way[67] as explained in the discussion of RNG model. The equilibrium shear stress g_{eq} in Eq. (22) is determined from the following equilibrium eddy viscosity distribution

$$\begin{aligned} \nu_{t,eq} =&\nu_{t_o,eq}\left[1-exp(-\frac{\nu_{t_i,eq}}{\nu_{t_o,eq}})\right] \\ \nu_{t_i,eq} =&D^2\kappa y\sqrt{(\overline{-u'w'})_{m,eq}} \\ \nu_{t_o,eq} =&0.0168U_e\delta^*\gamma \end{aligned} \tag{24}$$

where U_e is the velocity at the edge of the boundary layer.

An implicit Euler method is used for the numerical solution of Eq. (22), and the maximum shear stress at each iteration level is updated as follows

$$\sigma(x)^{n+1} = \sigma(x)^n\frac{\nu_{t_o}^{n+1}}{\nu_{t_o}^n} \tag{25}$$

It should be noted that the unsteady term is neglected in the above formulation. Solutions with the Johnson–King turbulence model are obtained as follows. First a convergent solution using the Baldwin–Lomax turbulence model for the entire flowfield is obtained. Then the Johnson–King model is applied only to the upper surface of the airfoil as using it for both the surfaces did not change the results. To initiate the solution $\sigma(x)$ in Eq. (21) is set unity and it is allowed to change according to Eq. (25). It should be noted that the Johnson–King model reduces to the Cebeci–Smith model[73] when $\sigma(x)$ is identically equal to one.

8.4 One–Equation Models

The B-L and the RNG models are equilibrium models, in which the production is identically equal to the dissipation. The J-K model is an improvement over the equilibrium turbulence models because it accounts for the evolution of the maximum shear stress through the solution of an ordinary differential equation (ODE). It, therefore, attempts to calculate the non-equilibrium turbulent boundary layer. The validity of these models is limited and questionable when applied to a flow environment consisting of unsteady separated flow with multiple shear layers.

Recently, several one-equation models have been developed for use in place of these lower-order turbulence models. In the present investigation two such models are considered for investigation. These are the Baldwin-Barth[68] and Spalart-Allmaras[69] models. The primary advantage of these methods is that they do not require the evaluation of flow-dependent length scales, such as the boundary layer thickness. The validity of these models for steady flows has been demonstrated, but only in a limited sense. In the present investigation these models are tested for several unsteady attached and separated flows over oscillating airfoils.

8.4.1 Baldwin-Barth (B-B) model

This one-equation model[68] is derived from the simplified form of the $k - \epsilon$ model equations. It solves for the modified turbulent Reynolds number $\nu\tilde{R}_T$ from

$$\begin{aligned}\frac{D(\nu\tilde{R}_T)}{Dt} =&(c_{\epsilon_2}f_2 - c_{\epsilon_1})\sqrt{\nu\tilde{R}_T P}\\ &+(\nu+\frac{\nu_t}{\sigma_\epsilon})\nabla^2(\nu\tilde{R}_T)\\ &-\frac{1}{\sigma_\epsilon}(\nabla\nu_t)\cdot\nabla(\nu\tilde{R}_T)\end{aligned} \qquad (26)$$

This is a partial differential equation for the field quantity $R_T = k^2/\nu\epsilon = \tilde{R}_T f_3(\tilde{R}_T)$, named turbulent Reynolds number. The turbulent Reynolds number is related to the eddy viscosity as

$$\nu_t = \nu c_\mu f_\mu R_T = \nu c_\mu f_\mu f_3 \tilde{R}_T \tag{27}$$

where

$$\begin{aligned}
\frac{1}{\sigma_\epsilon} &= (c_{\epsilon_2} - c_{\epsilon_1})\sqrt{c_\mu}/\kappa^2 \\
\nu_t &= c_\mu(\nu \tilde{R}_T) D_1 D_2 \\
\mu_t &= \rho \nu_t \\
f_\mu &= D_1 D_2 \\
D_1 &= 1 - exp(-y^+/A^+) \\
D_2 &= 1 - exp(-y^+/A_2^+) \\
P &= \nu_t\Big(\frac{\partial U_i}{\partial x_j} + \frac{\partial U_j}{\partial x_i}\Big)\frac{\partial U_i}{\partial x_j} - \frac{2}{3}\nu_t\Big(\frac{\partial U_i}{\partial x_j}\Big) \\
f_2(y^+) &= \frac{c_{\epsilon_1}}{c_{\epsilon_2}} + (1 - \frac{c_{\epsilon_1}}{c_{\epsilon_2}})(\frac{1}{\kappa y^+} + D_1 D_2) \\
&\quad \{\sqrt{D_1 D_2} + \frac{y^+}{\sqrt{D_1 D_2}}(\frac{1}{A^+}exp(-y^+/A^+)D_2 \\
&\quad + \frac{1}{A_2^+}exp(-y^+/A_2^+)D_1)\}
\end{aligned}$$

Here $y^+ = u_\tau y/\nu$ and u_τ is the skin friction velocity. The constants used for the B–B model are the same as in their original paper[68] and are given by:

$$\kappa = 0.41, \quad c_{\epsilon_1} = 1.2, \quad c_{\epsilon_2} = 2.0$$

$$c_\mu = 0.09, \quad A^+ = 26., \quad A_2{}^+ = 10.$$

This model is applied to the entire flowfield to compute the eddy viscosity.

8.4.2 Spalart-Allmaras (S-A) model

The second one-equation model used in the present investigation is the Spalart-Allmaras (S-A) model[69]. This model requires the solution of a transport (partial differential) equation for the turbulent eddy viscosity. This equation was constructed using empirical criteria and arguments from dimensional analysis. It has many similarities with the B-B model but it is relatively simpler for its numerical implementation. The S-A model also incorporates transition location specification, although the present investigation treats the boundary layer as turbulent on the entire surface. The eddy viscosity is obtained from the solution of the following partial differential equation.

$$\begin{aligned}
\frac{D\tilde{\nu}}{Dt} &= c_{b1}(1 - f_{t2})\tilde{S}\tilde{\nu} + \frac{1}{\sigma}\Big[\nabla \cdot ((\nu + \tilde{\nu})\nabla\tilde{\nu}) + c_{b2}(\nabla\tilde{\nu})^2\Big] \\
&\quad - \Big[c_{w1} f_w - \frac{c_{b1}}{\kappa^2} f_{t2}\Big]\Big[\frac{\tilde{\nu}}{d}\Big]^2 + f_{t1}\Delta U^2
\end{aligned} \tag{28}$$

where

$$
\begin{aligned}
f_{t1} &= c_{t1} g_t exp\Big(- c_{t2} \frac{\omega_{tr}^2}{\Delta U^2}[d^2 + g_t^2 d_t^2]\Big) \\
f_{t2} &= c_{t3} exp(-c_{t4}\chi^2) \\
g_t &= min(0.1, \Delta U/\omega_{tr}\Delta x)
\end{aligned}
\tag{29}
$$

where $\chi = \tilde{\nu}/\nu$ and ω_{tr} is used here to denote the vorticity at the wall at the boundary layer trip point. The constants of this model have been chosen the same as in the original reference[69], and the transition location was set at the airfoil leading edge. The model constants are:

$$
\begin{aligned}
c_{b1} &= 0.1355 \\
c_{b2} &= 0.622 \\
\sigma &= 2/3 \\
c_{w1} &= c_{b1}/\kappa^2 + (1 + c_{b2})/\sigma \\
c_{w2} &= 2.0 \\
c_{w3} &= 0.3 \\
\kappa &= 0.41 \\
f_w &= g\Big(\frac{1 + c_{w3}^6}{g^6 + c_{w3}^6}\Big)^{1/6} \\
g &= r + c_{w2}(r^6 - r), r = \frac{\nu_t}{S\kappa^2 d^2} \\
c_{t1} &= 1.0 \\
c_{t2} &= 2.0 \\
c_{t3} &= 1.1 \\
c_{t4} &= 2.0
\end{aligned}
$$

The relative computational costs for each of the five turbulence models is discussed towards the end of Results Section.

9. RESULTS AND DISCUSSION

This paper describes an attempt to evaluate five different, but widely used, turbulence models in calculating the unsteady, two-dimensional flowfields of an oscillating NACA 0015 wing spanning a wind tunnel wall and an end plate. The test cases considered for the calculation correspond to the wind tunnel conditions of an experiment of a NACA 0015 oscillating wing conducted in the 7x10 foot wind tunnel of the U. S. Army Aeroflightdynamics Directorate, located at NASA Ames Research Center[19]. The flow conditions of the experiment are as follows: free-stream Mach Number, $M_\infty = 0.29$ and Reynolds number,

$Re = 1.95x10^6$ based on the chord of the wing and free-stream speed. Four mean angles of $\alpha_0 = 4°, 11°, 15°$, and $17°$ are considered with an amplitude of pitch of $\alpha_1 = \pm 4.2°$ around the mean angle and a reduced frequency, $k = 0.1$. The instantaneous angle of attack of the wing is given by $\alpha(t) = \alpha_0 + \alpha_1 \ sin(Kt)$.

The present calculations are done for free-air conditions and, therefore, the wind tunnel walls are not included in the calculations. The unsteady calculations for oscillating airfoils are usually started from the steady state solution at the lowest angle of attack of the pitch cycle. However, to check the accuracy of the solution method, steady-state solutions were calculated for several angles of attack in a time-accurate manner. Figure 37 shows sample results of steady surface pressures for $\alpha = 13°$ (Fig. 37a) and 17° (Fig. 37b) compared with experiments. The B-L turbulence model yielded satisfactory surface pressures for the case of $\alpha = 11°$ where the flow is essentialy attached (not shown here). For the mildely separated case of $\alpha = 13°$ and the massively separated cases of $\alpha = 15°$ and 17°, the B-L model predicted surface pressures that had higher leading-edge suction peaks and milder separation. It gave higher lift and lower drag values. Therefore more accurate turbulence models were needed to predict satisfactory airloads. As seen in Fig. 37, the J-K model is able to predict the surface pressures more accurately than the B-L algebraic model at these conditions. Although not shown here, the B-B one-equation model fared as good at 13° and slightly better at 17° than the J-K model in predicting the overall quasi-steady airloads. The airfoil is completely stalled at the $\alpha = 17°$ condition.

Table 1 lists the calculated force coefficients for these two quasi-steady flow conditions and the experimental measurements. The airloads are calculated in this study by integrating the surface pressures. Therefore, the drag coefficient shown is that due to pressure drag only. There are large fluctuations in airloads in the experimental data not only from cycle to cycle at a single station, but also from station to station for a two-dimensional wing. The results listed for the coefficients of lift (C_l), drag (C_d), and pitching-moment about quarted-chord (C_m) in this table are time-averaged values over a large period of time for the calculations. The experimental value was read-off from Ref. 70. At the lower angle of $\alpha = 13°$, the J-K and B-B models did better in predicting the overall airloads than the B-L model, although all of them fail to predict accurately the drag and pitching-moment. At the stalled condition of 17° the flow was unsteady. The results are in poor agreement with each other and with experiment, although the agreement with experiments improved as the models got more sophisticated from B-L to B-B models.

The discussion of unsteady results is divided into three flow regimes, viz., a) attached flow corresponding to $\alpha_0 = 4°$; b) light-stall case corresponding to $\alpha_0 = 11°$; and c) deep-stall cases corresponding $\alpha_0 = 15°$ and 17°. After calculating the quasi-steady solution at the lowest angle of the pitch cycle for each of the condition, the airfoil is made to execute pitching oscillations rotating about its quarter-chord point. The unsteady flow evolution is monitored. Most of the results presented in the following paragraphs were calculated using 361x71 grid with 10,000 constant time-steps per osciallating cycle. This number of time-steps per cycle corresponds to a nondimensional time-step of $\Delta t = 0.0108$, based on c and a_∞. An explicit dissipation coefficient of $\epsilon_e = 0.05$ was used as the standard value. A parametric study of the grid size, the value of ϵ_e, and number of time-steps per cycle has also been done for one turbulence model, for the light-stall case, to identify optimum values to be used for all calculations and this discussions is presented in the section on the Light-stall.

9.1 Unsteady attached flow case: $\alpha(t) = 4° + 4.2° sin(Kt)$

This flow condition essentially serves to validate the accuracy of the flow solver in calculating unsteady attached flow. Figure 38 presents the calculated unsteady airloads with different turbulence models compared to the experimental data[70]. The experimental data is averaged over 20 cycles period and the calculations are not averaged but were found to be repeatable beyond the second cycle. The results of calculations with different turbulence models compare favorably with each other for lift and pressure drag, but the pitching-moment appears to be more sensitive. The RNG, J-K, and S-A models give relatively good comparison among themselves and with experimental data for lift, drag, and pitching-moment. It is surprising to see that the B-B model does relatively poorly compared to the above three models for lift and pitching-moment. Similarly, the B-L model does poorly in predicting the lift and pithing-moment. It consistently predicts higher lift and lower pitching-moments compared to the rest of the models. It should be noted that the scales used in presenting the airloads in Fig. 38 are expanded to bring out the differences clearly for various turbulence models, but in the scales used in rest of the study for different airloads, the results are well within the range of experimental scatter. The trends of the calculated results show that the if the results are tilted slightly, they perhaps agree better with experiments. As observed by McCroskey and Pucci[74] in their experiments with NACA 0012 oscillating wing, such a trend can be attributed to wind tunnel wall interference effects.

Figure 39 shows the details of unsteady pressure distributions by harmonic components, where the decomposition of C_p is according to $C_p = C_{p_0} + C_{p_{1s}} sin(Kt) + C_{p_{1c}} cos(Kt) + C_{p_2} sin(2Kt + \phi_2)$ with ϕ_2 as the phase-shift. In order to stretch out the leading-edge region of the airfoil, the various harmonics are plotted against $\sqrt{x}$. Such a representation brings out the variations and discrepancies better with linear theory. Note that the differences seen in the lift and pitching-moment hysteresis curves for B-L and B-B models in Fig. 38 relatively translate into small differences in the mean and quadrature components in Fig. 39. No experimental pressure data was available for comparison with these results, but comparison of the four components with the measurements of Ref. 74 for NACA 0012 oscillating airfoil for attached unsteady flow case show similar behavior for all the components.

9.2 Light-stall case: $\alpha(t) = 11^\circ + 4.2^\circ sin(Kt)$

Figures 40-45 show the results for the light-stall case for $\alpha_0 = 11^\circ$. In order to determine the optimum values of time-step, Δt, the explicit numerical dissipation coefficient, ϵ_e, and size of the grid for a reasonably accurate solution, parametric calculations have been done using one turbulence model (J-K) and varying these variables one at a time while keeping the others constant. For example, Fig. 40 presents results of unsteady airloads hysteresis for three values of Δt for a grid size of 361x71 and $\epsilon_e = 0.05$ along with experimental data. In Fig. 40, $\Delta t = 0.0108$ corresponds to using 10,000 time-steps per cycle. Similarly, $\Delta t = 0.0216$ corresponds to 5,000 time-steps per cycle. The maximum number used in the present calculations is 20,000 time-steps per cycle for deep-stall cases. This contrasts with 50,000 to 100,000 time-steps per cycle used by other investigators[62,63] in similar situations. The large number of time-steps in these investigations was dictated by the numerical stability of their solution method. Obviously these become prohibitively expensive when extended to three-dimensions. As seen in Fig. 40, a $\Delta t = 0.0108$ corresponding to 10,000 time-steps per cycle is a good compromise, and this is the number used for calculating all the results presented in this study.

The results of unsteady airloads presented in Fig. 41 shows that all three forces are very sensitive to the dissipation coefficeint ϵ_e. These airloads are calculated using a $\Delta t = 0.0108$ for a 361x71 grid with J-K turbulence model. For the four values of ϵ_e used, the upstroke results of lift, drag, and pitching-moment are nearly the same. Differences are seen for the downstroke results with higher values of ϵ_e giving better drag and pitching-moment predictions. From this, a value of $\epsilon_e = 0.05$ is chosen as the reference value for the rest of the calculations. For a value less than this, the solutions at other higher mean angles showed oscillatory behavior for the unsteady airloads.

Figure 42 presents the unsteady airloads results calculated on different grid sizes. Again, J-K model is used along with $\epsilon_e = 0.05$ and $\Delta t = 0.0108$ for these calculations. As seen the solutions are quite sensitive to the grids used. It should be noted that all grids have the same wall spacing of the first grid point in the normal direction and the boundaries are located at the same distance from the airfoil. It is surprising to see that even fine grids have produced poor results compared to the 361x71 grid. This perhaps is due to using the same ϵ_e for all cases. It is evident from the results presented in Fig. 42 that for the ϵ_e and Δt used, the 361x71 grid appears to be the best choice and this is the grid used for most results presented in this study.

A similar result of grid-sensitive study using B-B model is presented in Fig. 43. For this turbulence model, the unsteady airloads show less sensitivity to different grids. These results are also calculated using the same values of Δt and ϵ_e as those of Fig. 42 for J-K model. As seen, the drag and pitching-moment have better agreement with experiment for both upstroke and downstroke, but the lift on the downstroke has very poor agreement with experiment indicating that the flow reattachment is not complete until after the upstroke begins. Again the 361x71 grid appears to be the optimum grid for the given Δt and dissipation.

Using the above suggested optimum values for Δt, ϵ_e, and 316x71 grid, unsteady flowfield solutions are calculated using all the turbulence models. Figure 44 presents the unsteady airloads results from these solutions. Comparison of results for different turbulence models reveal that every model behaves differently. The chief characteristic of all these solutions is that all models produce trailing-edge separation. The B-L model (not shown in this figure) produces the least separation. The lift, drag, and pitching–moment hysteresis curves for this model are distinctly different from the rest of the solutions and, in particular, the lift and pitching-moment are in poor agreement with experiment. The lift hysteresis curves for the J-K, RNG, and S-A models are in good agreement with experiments, although the RNG model has slightly higher lift during the upstroke. In general, all models show good agreement with each other and with experiment for the unsteady airloads on the upstroke part of the cycle. As seen here, no one model has perfect agreement with experiment for all airloads. Once the flow separates on the upper surface of the airfoil, before the downstroke begins, the B-B model appears to recover very slowly to the attached flow condition compared to the other models. In fact the boundary layer reattachment is not complete for the B-B model until after the upstroke begins. Therefore, the lift stays very low until the upstroke begins. Although not apparent in the drag curve, this is very well seen in the pitching-moment curve.

The RNG and J-K models produce nearly the same extent of separation that is much larger than what the B-B model produces. They also appear to have similar recovery in the downstroke much better than the B-B model. Both models predict very similar drag and pitching-moment that are in poor agreement with experiment for the downstroke. The S-A model produces separation similar in extent to the B-B model, but has good recovery just like the J-K model. The lift hysteresis for this model is in good agreement with experiment, like the J-K model, and the drag and pitching-moment are in better agreement with experiment than the J-K model but not as good as the B-B model. All the models except the B-B model predict poor pitching-moments. The B-B model produces nearly the right amount of separation and, that is the reason, it predicts pitching-moment correctly including its cusp-like behavior at the end of upstroke. The hump-like behavior at the end of downstroke is the result of poor recovery as discussed before.

In general, all models predict the unsteady airloads reasonably well for the upstroke and they all behave differently during the downstroke. The B-B model is the only model that predicts the pitching-moment correctly and in agreement with experimental data except for the part at the end of downstroke. But it nicely recovers as the upstroke begins. No leading-edge separation is seen for any of the models, perhaps due to negleting laminar and transition regions and assuming turbulent boundary layer for the entire airfoil.

Figure 45 shows the harmonic components of unsteady pressures calculated for this light-stall case using the J-K and B-B models. All four parts of this figure are different from those of the preceding attached case, $\alpha_0 = 4°$, shown in Fig. 39. The large changes seen in these curves can be attributed to the nonlinear behavior of the flow at this mean angle of $\alpha_0 = 11°$. The two models predict very similar mean and in-phase components. But the very different pitching-moments produced by the two models is apparent in the out-of-phase component.

9.3 Deep-stall case: $\alpha(t) = \alpha_0 + 4.2° \, sin(Kt)$

In contrast to the light-stall with mild trailing-edge separation seen for $\alpha_0 = 11°$ case, the deep-stall cases for $\alpha_0 = 15°$ and 17° are dominated by massive flow separation and highly nonlinear flow behavior. The separation that originates in the trailing-edge region, during the upstroke of the oscillatory cycle, continues to spread upstream as the airfoil motion changes to downstroke. The unsteady stall behavior in this regime is characterized by the shedding of a large vortex-like structure during the downstroke of the cycle. This structure convects over the upper surface of the airfoil and leaves the trailing edge before the downstroke part of the oscillatory cycle is completed. As a result, unsteady airloads far in excess of the static counterpart are generated during the upstroke and large amounts of hysteresis occur during the remainder of the cycle. The scale of the viscous-inviscid interaction zone is also large, producing a viscous layer thickness of the order of the airfoil chord, particularly during the vortex shedding process.

Figure 46 shows the calculated lift, drag, and pitching-moment hysteresis loops for the $\alpha_0 = 15°$ case using different turbulence models. The results are also compared to experimental data. For reference, the B-L results are also shown for this case. Examination of individual curves reveals the following behavior. The lift hysteresis is in general agreement with calculations for all turbulence models except for the B-L model which shows an oscillatory-type behavior for the loads during downstroke. All models show very good agreement with each other and with the experiment for the upstroke lift curve. There are differences in the size of the dynamic stall vortex produced by each model and its convection downstream. Nevertheless, there are only minor differences in the downstroke lift curves for these models. As before, the B-B model shows clearly that it is slow in the recovery and reattachment process. As a result, the lift stays lower compared to the experimental value and the recovery is not complete until the airfoil changes its attitude from downstroke to upstroke motion.

Reasonbly good agreement of lift curves with experiment is not an indication to how the drag and pitching-moment are predicted. Unlike the light-stall results for drag and pitching-moment of Fig. 44, the deep-stall case shows a steep rise in drag curve and negatively steep rise in the pitching-moment towards the end of the upstroke of the cycle. The J-K model which predicted good lift and drag curves for mean angles $\alpha_0 = 4°$ and 11°, also shows good agreement for lift hysteresis with experiment, but predicts poorly for the drag and pitching-moment. Examination of instantaneous particle flow pictures of flow at different airfoil positions during the downstroke reveals that the dynamic stall vortex leaves the surface much sooner than what other models predict. Except for the B-L and J-K models, all other models have good qualitative agreement with experiment for drag and pitching-moment.

The behavior of the intantaneous surface pressures during the oscillatory cycle is shown in Fig. 47 for the upper surface of the airfoil for the B-B model. As seen in this figure, the leading-edge suction peak continues to rise through the upstroke without stall. The peak angle of attack at the end of upstroke is 19.2°. This angle is about 6° above the static stall angle for this airfoil, as unsteady effects extend the dynamic lift beyond the static stall angle. The leading-edge suction peak suddenly collapses immediately after the airfoil starts the downstroke, as revealed by the surface pressure distributions. Another revealing feature of this plot is that the vortex shedding phenomenon manifests itself in the pressure distributions on the downstroke.

The harmonic components of the unsteady pressures for the B-B model are presented in Fig. 48. Three of the four components are very different from those of the light-stall case presented in Fig. 45 and also of the unseparated flow presented in Fig. 39. Only the mean-component is qualitatively similar in shape to Fig. 45a. The in-phase, out-of-phase, and the second harmonic are all changed by the massive separation and the presence of a large–scale dynamic stall vortex. The growth of the second harmonic indicates the flow is highly nonlinear.

The various turbulence models produce different sizes of dynamic stall vortex and separated flow. An examination of the loci of the flow reversal point (x_s) on the upper surface of the airfoil (Fig. 49) shows that at any given instant of time, the extent of reversed flow varies widely. The B-L model produces the smallest extent of reversed flow over most of the cycle whereas the B-B model produces the largest extent of reversed flow. The position indicating 0° phase denotes the mean angle of oscillation. It is apparent from this figure that the B-B model completes the recovery process on the upstroke only when it reaches approximately the mean angle. For the large part of the cycle, from 15° upstroke to 15° downstroke, the RNG, B-B, and S-A models predict nearly the same extent of reversed flow. The massive reversed flow regions clearly increase the unsteady-lag effects.

Figure 50 shows a four-part figure of the instantaneous flow pictures of the extent of the dynamic stall vortex at different times of the oscillatory cycle for the B-B model. The flow which separates in the trailing-edge region during the upstroke cycle continues to increase in extent by moving the flow reversal point, S, upsteam towards the leading-edge region. As seen in this figure, the dynamic stall vortex has peaked in in its size around 17° downstroke and from then on it prepares to shed by moving the flow reversal point away from the leading edge.

Another way of demonstrating the performance of the various turbulence models is through the examination of instantaneous flow pictures at any one given phase in the oscillatory cycle. For example, Fig. 51 shows instantaneous steamline particle flow pictures for all turbulence models corresponding to the instant when the airfoil is at 16° on the downstroke. The three models, RNG, B-B, and S-A have very similar dynamic stall vortex structures at this instant. The B-L model has a complex pattern with primary and secondary vortices, whereas the J-K model has already shed the primary vortex at this time. All models produce multiple vortices at slightly different times during the downstroke. The B-L model also produces a small bubble in the leading edge region, identified as $S1$, when the airfoil has reached 14.5° in the upstroke. This bubble stays distinctly separate from the region containing the dynamic stall vortex and eventually merges with this at about 15° downstroke. The locus of the reverse flow points shown in Fig. 49 is for the point marked S in Fig. 51a.

The instantaneous streamline pictures of Fig. 51 are used only for qualitative comparison of different turbulence models. In fact, such a representation of flow appears to be misleading as it does not depict the correct picture of the unsteady flow. Visualization of the same flow using streaklines show a very different flow picture. (The steaklines are computed using a Lagrangian description for the fluid particles through UFAT[75] program.) For example, Fig. 52 shows the same flow that is pictured in Fig. 51d at 16° downstroke for the B-B model. As seen here, the flow pattern and the details shown by streaklines are phenomenally different compared to Fig. 51d. The large-scale dynamic-stall vortex (V1), the pairing of vortices downstream of trailing-edge (V2), and a diffused pair of vortices further downstream of this (V3) is something that is not apparent from the instantaneous streamline patterns of Fig. 51d. Therefore, it is necessary to be cautious in interpreting instantaneous steamline patterns of unsteady flowfield.

Another case of deep-stall considered is for the mean angle of $\alpha_0 = 17°$. This flow was calculated using both 10,000 and 20,000 time-steps per oscillatory cycle. It appears that for this deep-stall case at least 15,000 time-steps are needed to capture the important details of the flow. The results of unsteady airloads presented in Fig. 53 are calculated using 20,000 time-steps. Comparison of calculations with experiments show that all models predict the lift hysteresis fairly accurately, although the RNG and the J-K models show oscillatory behavior during the downstroke. The calculated results are slightly shifted from the experimental data and every model predicts separation at different instant on the upstroke. Nevertheless, they all reproduce the details of the lift hysteresis correctly. The J-K model predicts C_d and C_m loops that are incorrect both for the upstroke and downstroke. The S-A model although has the right trends for drag and pitching-moment, it produces separation too early, with the result it underpredicts the peak drag and pitching-moments. The RNG and the B-B models calculate all the three components fairly accurately. The RNG model shows oscillatory behavior for the drag and pitching-moment curves also. The results for all the models are shifted compared to the experimental data. The flowfield on the downstroke part of the cycle is very complicated. Although it is shifted from the experimental data, it appears that the B-B model has demonstrated superior performance for this flow condition in predicting all unsteady airloads correctly.

It is important to know how much each model costs computationally. Figure 54 shows the relative costs of these turbulence models averaged over all the calculations performed. The B-L model is used as the reference as this is the most commonly used of all models and least expensive. As seen, the B-B model is the most expensive model and costs about 2.5 times the cost of B-L model. The S-A model closely follows the B-B model. There is no clear choice of any one single model that has consistently superior performance for all flow regimes. The one that comes close to this from this evaluation is the RNG model. It is also cheaper to run and costs as much as the B-L model. The B-L model accounts for 15.6% of the total CPU of the numerical code.

9.4 Three-Dimensional Deep-stall case: $\alpha(t) = 15° + 4.2°\ sin(Kt)$

The TURNS CFD code was modified for calculating the unsteady flowfields of an oscillating wing. Some preliminary calculations were done using Baldwin-Lomax[26] turbulence model for the deep-stall case of $\alpha(t) = 15° + 4.2°\ Sin(Kt)$. Just like in the two-dimensional case, the Baldwin-Lomax model was found to be inadequate to resolve the separated flow and the model totally underpredicted the extent of separation. Some findings of this study was presented at the International Dynamic Stall Workshop. The inadequacy of the simple algebraic model to resolve the unsteady separated flow necessitated a detailed study of using alternative turbulence models that are more accurate. The results of this study is described in the previous sections.

10. CONCLUDING REMARKS

The unsteady, two-dimensional flowfield of an oscillating NACA 0015 airfoil is calculated using an implicit, finite-difference numerical method for the solution of the Navier-Stokes equations with intent to evaluate the accuracy of five widely used turbulence models to calculate the unsteady separated flows of dynamic stall. Several unsteady flow conditions corresponding to attached flow, light-stall, and deep-stall cases of an oscillating wing experiment were chosen as test cases for calculations. The comparison of results with experiments show that the RNG, the J-K, and the S-A models predict lift, drag, and pitching-moment hysteresis that are in good agreement for unsteady attached flow. All three models overpredict the extent of separation for the light-stall case and therefore the airloads have good agreement only for the upstroke. They have good qualitative agreement for lift and drag hysteresis for the downstroke, but they fail to predict pitching-moments correctly. The B-L model performs very poorly even for the attached flow. The B-B model also performs poorly in predicting lift and pitching-moment for this attached flow case. For the light-stall case, it predicts lower lift than experiment for the downstroke because of slow recovery. But the drag and pitching-moment are better predicted than other models. For the deep-stall cases, the RNG, the B-B, and S-A models all predict qualitatively correct airload hysteresis, but the RNG model yields oscillatory behavior during the downstroke for the extreme deep-stall case. The J-K results are not even qualitatively correct on the downstroke for the deep-stall cases. Overall, the RNG model provides significant improvement over the B-L model with no additional computational cost. Among the models considered here, the B-B model is the most expensive and costs about 2.5 times the cost required to run the code with the B-L or RNG models. The B-L model accounts for 15.6% of the total CPU time required to run the numerical code. Finally, visualization of unsteady flowfields by means of instantaneous streamlines will give a misleading representation of the flow. A Lagrangian description of particle motion using streaklines is perhaps more cumbersome but better. Such a description gives a totally different flow picture compared to the streamline pattern.

A modified version of the TURNS code with Baldwin-Lomax turbulence model was used to calculate the unsteady flowfields of an oscillating wing for the deep-stall case. Just like in two-dimensional case, the simple algebraic model was found to be inadequate and produced very little separation and poor agreement for the results with experiments.

11. REFERENCES

1. Caradonna, F. X., Desopper, A., and Tung, C., "Finite Difference Modeling of Rotor Flows Including Wake Effects," Paper No. 2.7, ***Eigth European Rotorcraft Forum***, Aix-en Provence, France, Aug. 1982.

2. Strawn, R. C. and Caradonna, F. X., "Conservative Full-Potential Model for Unsteady Transonic Rotor Flows," ***AIAA Journal***, Vol. 25, No. 2, Feb. 1987, pp. 193-198.

3. Strawn, R. C. and Tung, C., "The Prediction of Transonic Loading on Advancing Helicopter Rotors," NASA Technical Memorandum 88238, April 1986.

4. Chang, I-C. and Tung, C., "Numerical Solution of the Full-Potential Equation for Rotor and Oblique Wings using a New Wake Model," AIAA Paper 85-0268, Jan. 1985.

5. Egolf, T. A. and Sparks, S. P., "A Full Potential Flow Analysis with Realistic Wake Influence for Helicopter Rotor Airload Prediction," NASA Contractor Report 4007, Jan. 1987.

6. Chang, I-C. and Tung. C., "Euler Solution of the Transonic Flow for a Helicopter Rotor," AIAA Paper 87-0523, Jan. 1987.

7. Agarwal, R. K. and Deese, J. E., "Euler Calculations for a Flowfield of a Helicopter Rotor in Hover," ***Journal of Aircraft***, Vol. 24, No. 4, April 1987, pp. 231-238.

8. Sankar, N. L., Wake, B. E., and Lekoudis, S. G.. "Solution of the Unsteady Euler Equations for Fixed and Rotor Wing Configurations," ***Journal of Aircraft***, Vol. 23, No. 4, April 1986.

9. Srinivasan, G. R. and McCroskey, W. J., "Navier-Stokes Calculations of Hovering Rotor Flowfields," ***Journal of Aircraft***, Vol. 25, No. 10, October 1988, pp. 865-874.

10. Wake, B. E. and Sankar. N. L., "Solutions of the Navier-Stokes Equations for the Flow About a Rotor Blade," ***Journal of the American Helicopter Society***, Vol. 34, No. 2, April 1989, pp. 13-23.

11. Agarwal, R. K. and Deese, J. E., "Navier-Stokes Calculations of the Flowfield of a Helicopter Rotor in Hover," AIAA Paper 88-0106, 1988.

12. Narramore, J. C. and Vermeland, R., "Use of Navier-Stokes Code to Predict Flow Phenomena Near Stall as Measured on a 0.658-Scale V-22 Tiltrotor Blade," AIAA Paper 89-1814, June 1989.

13. Ramachandran, K., Tung. C., and Caradonna, F. X., "Rotor Hover Performance Prediction Using a Free-Wake, Computational Fluid Dynamics Method," ***Journal of Aircraft***, Vol. 26, No. 12, Dec. 1989, pp. 1105-1110.

14. Kramer, E., Hertel, J., and Wagner, S., "Computation of Subsonic and Transonic Helicopter Rotor Flow Using Euler Equations," ***Vertica***, Vol. 12, No. 3, 1988, pp. 279-291.

15. Kroll, N., "Computation of the Flow Fields of Propellers and Hovering Rotors Using Euler Equations," Paper No. 28, ***Twelfth European Rotorcraft Forum***, Garmisch-Partenkirchen, Federal Republic of Germany, Sept. 1986.

16. Roberts, T. W. and Murman, E M., "Solution Method for a Hovering Helicopter Rotor Using the Euler Equations," AIAA Paper 85-0436, Jan. 1985.

17. Chen, C.-L. and McCroskey, W. J., "Numerical Simulation of Helicopter Multi-Bladed Rotor Flow," AIAA Paper 88-0046, Jan. 1988.

18. Chen, C. S., Velkoff, H. R., and Tung, C., "Free-Wake Analysis of a Rotor in Hover," AIAA Paper 87-1245, June 1987.

19. Rajagopalan, R. G. and Lim, C. K., "Laminar Flow Analysis of a Rotor in Hover," ***Journal of the American Helicopter Society***, Vol. 36, No. 1, January 1991, pp. 12-23.

20. Vatsa, V. N., Thomas, J. L. and Wedan, B. W., "Navier-Stokes Computations of Prolate Spheroids at Angle of Attack," AIAA Paper 87-2627, Aug. 1987.

21. Obayashi, S., "Numerical Simulation of Underexpanded Plumes Using Upwind Algorithms," AIAA Paper 88-4360-CP, Aug. 1988.

22. Schmitz, F. H. and Yu, Y. H., "Helicopter Impulsive Noise: Theoretical and Experimental Status," in ***Recent Advances in Aeroacoustics***, Eds. A. Krothapalli and C. A. Smith, Springer-Verlag, New York, 1986, pp. 149-243.

23. Srinivasan, G. R. and Baeder, J. D., "Recent Advances in Euler and Navier-Stokes Methods for Calculating Helicopter Rotor Aerodynamics and Acoustics," ***Proceedings of the Fourth International Symposium on Computational Fluid Dynamics***, September 1991, Davis, California, Vol. II, pp. 1095-1100.

24. Pulliam, T. H. and Steger, J. L., "Implicit Finite-Difference Simulations of Three-Dimensional Compressible Flow," ***AIAA Journal***, Vol. 18, No. 2, Feb. 1980, pp. 159-167.

25. Vinokur, M., "An Analysis of Finite-Difference and Finite-Volume Formulations of

Conservation Laws," *Journal of Computational Physics*, Vol. 81, No. 1, Mar. 1989, pp. 1-52.

26. Baldwin, B. S. and Lomax, H., "Thin Layer Approximation and Algebraic Model for Separated Turbulent Flow," AIAA Paper 78-0257, Jan. 1978.

27. Roe, P. L., "Approximate Riemann Solvers, Parameter Vectors, and Difference Schemes," *Journal of Computational Physics*, Vol. 43, 1981, pp. 357-372.

28. Anderson, W. K., Thomas, J. L. and van Leer, B., "A Comparison of Finite Volume Flux Vector Splittings for the Euler Equations," AIAA Paper 85-0122, Jan. 1985.

29. Jameson, A. and Yoon, S., "Lower-Upper Implicit Schemes with Multiple Grids for the Euler Equations," *AIAA Journal*, Vol. 25, No. 7, July 1987, pp. 929-935.

30. Yoon, S. and Jameson, A., "An LU-SSOR Scheme for the Euler and Navier-Stokes Equations," AIAA Paper 87-0600, Jan. 1987.

31. Koren, B., "Upwind Schemes, Multigrid and Defect Correction for the Steady Navier-Stokes Equations," *Proceedings of 11th International Conference on Numerical Methods in Fluid Dynamics*, June 1988.

32. Srinivasan, G. R., Chyu, W. J. and Steger, J. L., "Computation of Simple Three-Dimensional Wing-Vortex Interaction in Transonic Flow," AIAA Paper 81-1206, June 1981.

33. Caradonna, F. X. and Tung, C., "Experimental and Analytical Studies of a Model Helicopter Rotor in Hover," NASA Technical Memorandum 81232, Sept. 1981.

34. Sorenson, R. L., "A Computer Program to Generate Two-Dimensional Grids About Airfoils and Other Shapes by the Use of Poisson's Equation," NASA Technical Memorandum 81198, May 1980.

35. Srinivasan, G. R., McCroskey, W. J., Baeder, J. D., and Edwards, T. A., "Numerical Simulation of Tip Vortices of Wings in Subsonic and Transonic Flows," *AIAA Journal*, Vol. 26, No. 10, Oct. 1988, pp. 1153-1162.

36. Hertel, J., Kramer, E., and Wagner, S., "Complete Euler Solution for a Rotor in Hover and a Propeller in Forward Flight," Paper I.4.2, *Sixteenth European Rotorcraft Forum*, Glasgow, Scotland, Sept. 1990.

37. Srinivasan, G. R., Raghavan, V., and Duque, E. P. N., "Flowfield Analysis of Modern Helicopter Rotors in Hover by Navier-Stokes Method," *Proceedings of the American Heli-*

copter Society - Royal Aeronautical Society International Technical Specialists Meeting on Rotorcraft Acoustics and Rotor Fluid Dynamics, Philadelphia, Pennsylvania, October 1991.

38. Strawn, R. C., "Wing-Tip Vortex Calculations with an Unstructured Adaptive-Grid Euler Solver," *Proceedings of the 47th Annual Forum of the American Helicopter Society*, Phoenix, Arizona, May 1991, pp. 65-76.

39. Lorber, P. F., Stauter, R. C., and Landgrebe, A. J., "A Comprehensive Hover Test of the Airloads and Airflow on an Extensively Instrumented Model Helicopter Rotor," *Proceedings of the 45th Annual Forum of the American Helicopter Society*, Boston, Mass., May 1989.

40. Duque, E. P. N., "A Numerical Analysis of the British Experimental Rotor Program Blade," *Journal of the American Helicopter Society*, Vol. 37, No. 1, January 1992, pp. 46-54.

41. Johnson, W., *Helicopter Theory*, Princeton University Press, 1980.

42. Perry, F. J., "Aerodynamics of the Helicopter World Speed Record," *Proceedings of the 43rd Annual Forum of the American Helicopter Society*, May 1987.

43. Kramer, E., Hertel, J., and Wagner, S., "Euler Procedure for Calculation of the Steady Rotor Flow with Emphasis on Wake Evolution," AIAA Paper 90-3007, AIAA 8th Applied Aerodynamics Conference, Portland, OR, August 1990.

44. Caradonna, F. X., Laub, G. H., and Tung, C., "An Experimental Investigation of the Parallel Blade-Vortex Interaction," Paper No. 4, *Proceedings of the Tenth European Rotorcraft Forum*, The Hague, Netherlands, Aug. 1984.

45. Caradonna, F. X., Lautenschlager, J. L., and Silva, M. J., "An Experimental Study of Rotor-Vortex Interaction," AIAA Paper 88-0045, Jan.1988.

46. Srinivasan, G. R. and Baeder, J. D., "TURNS: A Free-Wake Euler/Navier-Stokes Numerical Method for Helicopter Rotors," *AIAA Journal*, Vol. 31, No. 5, May 1993, pp. 959-962.

47. Srinivasan, G. R. and McCroskey, W. J., "Euler Calculations of Unsteady Interaction of Advancing Rotor with a Line Vortex," *AIAA Journal*, Vol. 31, No. 9, September 1993, pp. 1659-1666.

48. Srinivasan, G. R., "Computations of Two-Dimensional Airfoil-Vortex Interactions," NASA CR-3885, May 1995.

49. Srinivasan, G. R., McCroskey, W. J., and Baeder, J. D., "Aerodynamics of Two-Dimensional Blade-Vortex Interaction," *AIAA Journal*, Vol. 24, No. 10, Oct. 1986, pp. 1569-1576.

50. Boxwell, D. A., Yu, Y. H., and Schmitz, F. H., "Hovering Impulsive Noise: Some Measured and Calculated Results," *Vertica*, Vol. 3, No. 1, 1979, pp. 35-45.

51. Purcell, T. W., "A Prediction of High Speed Rotor Noise," AIAA Paper 89-1130, July 1989.

52. Schmitz, F. H., Boxwell, D. A., Splettstoesser, W. R., and Schultz, K. J., "Model Rotor High-Speed Impulsive Noise : Full-Scale Comparisons and Parametric Variations," *Vertica*, Vol. 8, No. 4, 1984, pp. 395-422.

53. McCroskey, W. J., "Some Current Research in Unsteady Fluid Dynamics - 1976 Freeman Scholar Lecture," *Journal of Fluids Engineering*, Vo. 99, March 1977, pp. 8.38.

54. McCroskey, W. J., "Unsteady Airfoils," *Annual Reviews of Fluid Mechanics*, Vol. 14, Van Dyke et al. Eds., Annual Reviews, Inc., Palo Alto, Calif., 1982, pp. 285-311.

55. Carr, L. W., "Progress in Analysis and Prediction of Dynamic Stall," *Journal of Aircraft*, Vol. 25, No. 1, January 1988, pp. 6-17.

56. "AFOSR Workshop on Supermaneuverability: Physics of Unsteady Separated Flows at High Angle-of-Attack," Lehigh University, April 1992.

57. Ghia, K. N., Yang, Y., Oswald, G. A., and Ghia, U., "Study of the Role of Unsteady Separation in the Formation of Dynamic Stall Vortex," AIAA Paper 92-0196, Jan. 1992.

58. Visbal, M. R. and Shang, J. S., "Investigation of the Flow Structure Around a Rapidly Pitching Airfoil," *AIAA Journal*, Vol. 27, No. 8, Aug. 1989, pp. 1044-1055.

59. Wu, J.-C., Huff, D. L., and Sankar, L. N., "Evaluation of Three Turbulence Models in Static Air Loads and Dynamic Stall Predictions," *Journal of Aircraft*, Vol. 27, No. 4, April 1990, pp. 382-384.

60. Rizetta, D. P. and Visbal, M. R., "Comparitive Numerical Study of Two Turbulence Models for Airfoil Static and Dynamic Stall," *AIAA Journal*, Vol. 31, No. 4, April 1993, pp. 784-786.

61. Rumsey, C. L. and Vatsa, V. N., "A Comparison of the Predictive Capabilities of

Several Turbulence Models Using Upwind and Central-Difference Computer Codes," AIAA Paper 93-0192, Jan. 1993.

62. Dindar, M. and Kaynak, U., "Effect of Turbulence Modeling on Dynamic Stall of a NACA0012 Airfoil," AIAA PAPER 92-0027, Jan. 1992.

63. Geissler, W. and Vollmers, H., "Unsteady Separated Flows on Rotor-Airfoils - Analysis and Visualization of Numerical Data," *Proceedings of the Eighteenth European Rotorcraft Forum*, Paper No. 79, Sept. 1992, Avignon, France.

64. Knight, D. D. and Choudhuri, P. G., "Two-Dimensional Unsteady Leading- Edge Separation on a Pitching Airfoil," AIAA Paper 93-2977, July 1993.

65. Yakhot, V. and Orzag, S. A., "Renormalization Group Analysis of Turbulence. 1-Basic Theory," *Journal of Scientific Computing*, Vol. 1, 1986.

66. Johnson, D. A. and King, L. S., "A Mathematically Simple Turbulence Closure Model for Attached and Separated Turbulent Boundary Layers," *AIAA Journal*, Vol. 23, No. 11, Nov. 1985, pp. 1684-1692.

67. Johnson, D. A., "Nonequilibrium Algebraic Turbulence Modeling Considerations for Transonic Airfoils and Wings," AIAA Paper 92-0026, Jan. 1992.

68. Baldwin, B. S. and Barth, T. J., "A one-equation Turbulence Transport Model for High Reynolds Number Wall-Bounded Flows," AIAA Paper 91-0610, Jan. 1991; also NASA TM-102847, Aug. 1990.

69. Spalart, P. R. and Allmaras, S. R., "A One-Equation Turbulence Model for Aerodynamic Flows," AIAA Paper 92-0439, Jan. 1992.

70. Piziali, R. A., "An Experimental Investigation of 2D and 3D Oscillating Wing Aerodynamics for a Range of Angle of Attack Including Stall," NASA Technical Memorandum, 1993 (To be published).

71. Steger, J. L., "Implicit Finite Difference Simulation of Flow About Arbitrary Two-Dimensional Geometries," *AIAA Journal*, Vol. 18, No. 7, July 1978, pp. 679-686.

72. Jameson, A., Schmidt, W., and Turkel, E., "Numerical Solutions of the Euler Equations by Finite Volume Methods Using Runge-Kutta Time Stepping Schemes," AIAA Paper 81-1259, June 1981.

73. Cebeci, T. and Smith, A. M. O., *Analysis of Turbulent Boundary Layers*, Academic

Press, New York, 1974.

74. McCroskey, W. J. and Pucci, S. L., "Viscous-Inviscid Interaction on Oscillating Airfoils in Subsonic Flow," *AIAA Journal*, Vol. 20, No. 2, Feb. 1982, pp. 167-174.

75. Lane, D. A., "Unsteady Flow Analysis Kit - UFAT," Report RND-93-009, NASA Ames Research Center, May 1993.

12. FIGURES AND TABLES

Table 1
Calculated and experimental hover performance parameters for the UH-60A Black Hawk and BERP rotors for $M_{tip} = 0.628$

Rotor	Methods of results	θ_c	C_T/σ	C_Q/σ	FM
UH-60A model rotor	Experiments	Restricted information	0.085	0.0069	0.73
	N-S results	9°	0.084	0.0068	0.73
	N-S results with new farfield BC	9°	0.087	0.0069	0.76
UH-60A equivalent rectangular blade rotor	N-S results	9°	0.078	0.0065	0.69
UH-60A linear twist blade rotor	N-S results	9°	0.083	0.0072	0.68
UH-60A model rotor	N-S results	13°	0.140	0.0149	0.72
BERP rotor	N-S results	9°	0.098	0.0100	0.72
	N-S results	13°	0.162	0.0202	0.75

Table 2
Thrust and power coefficients for the UH-60A and BERP rotors

Rotor	θ_c	C_T	$C_{Q_{pr}}$	C_{Q_s}	C_Q
UH-60A Black Hawk model rotor	9°	0.007038	0.0004857	0.0000867	0.000572
	13°	0.011821	0.0011866	0.0000694	0.001256
BERP rotor	9°	0.010741	0.0009638	0.0001291	0.001093
	13°	0.017628	0.002072	0.0001288	0.002201

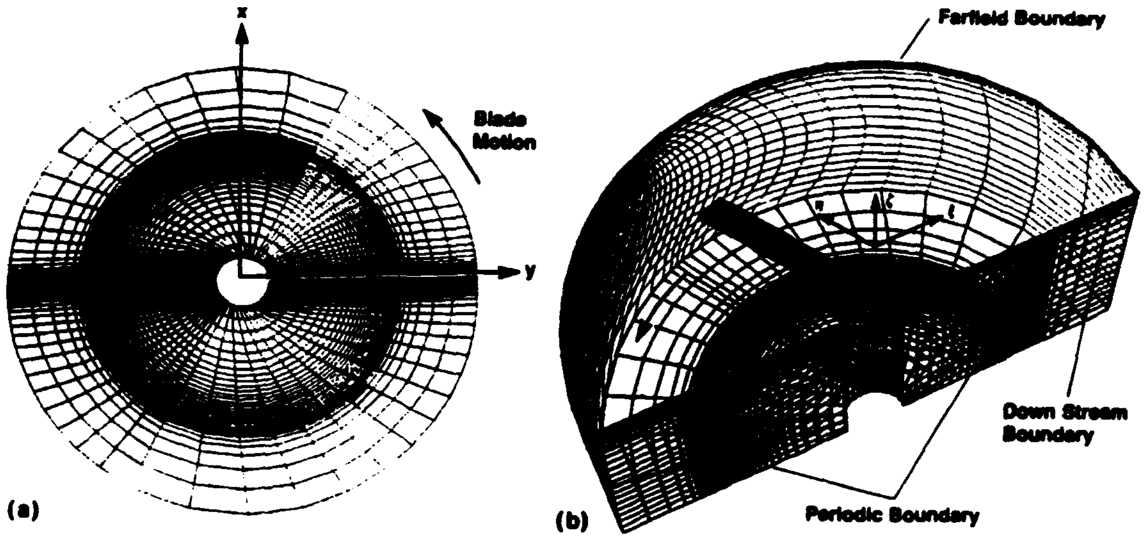
x
Blade Motion
y
(a)
Farfield Boundary
η
ζ
ξ
Down Stream Boundary
Periodic Boundary
(b)

Fig. 1 A C-H cylindrical grid topology for a two-bladed rotor; a) view in the plane of the rotor, and b) isometric view showing the grid boundaries for a single blade.

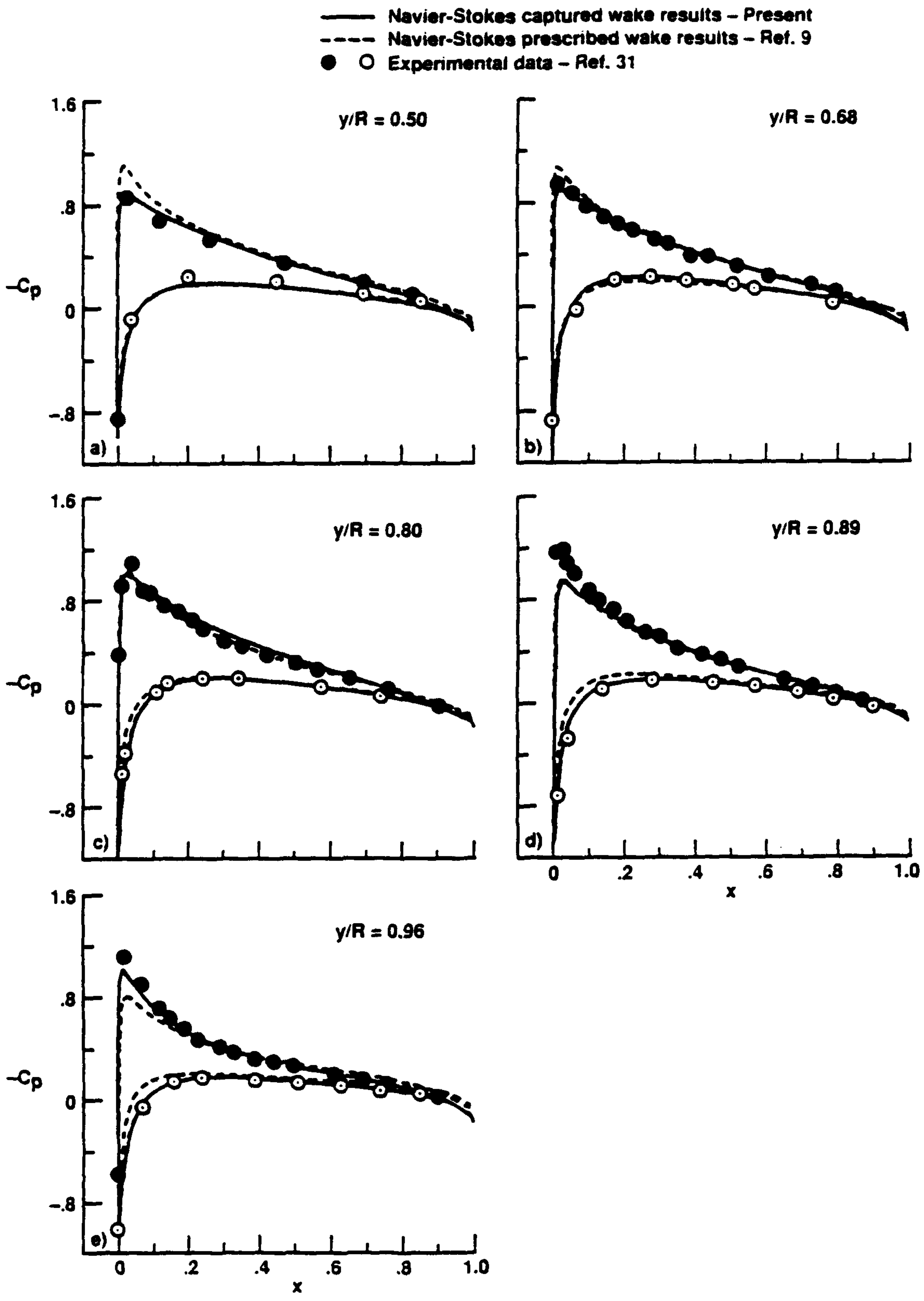

Fig. 2 Comparison of surface pressures for a lifting rotor in hover; $M_{tip} = 0.44$, $\theta_c = 8°$, and $Re = 1.92\times10^6$.

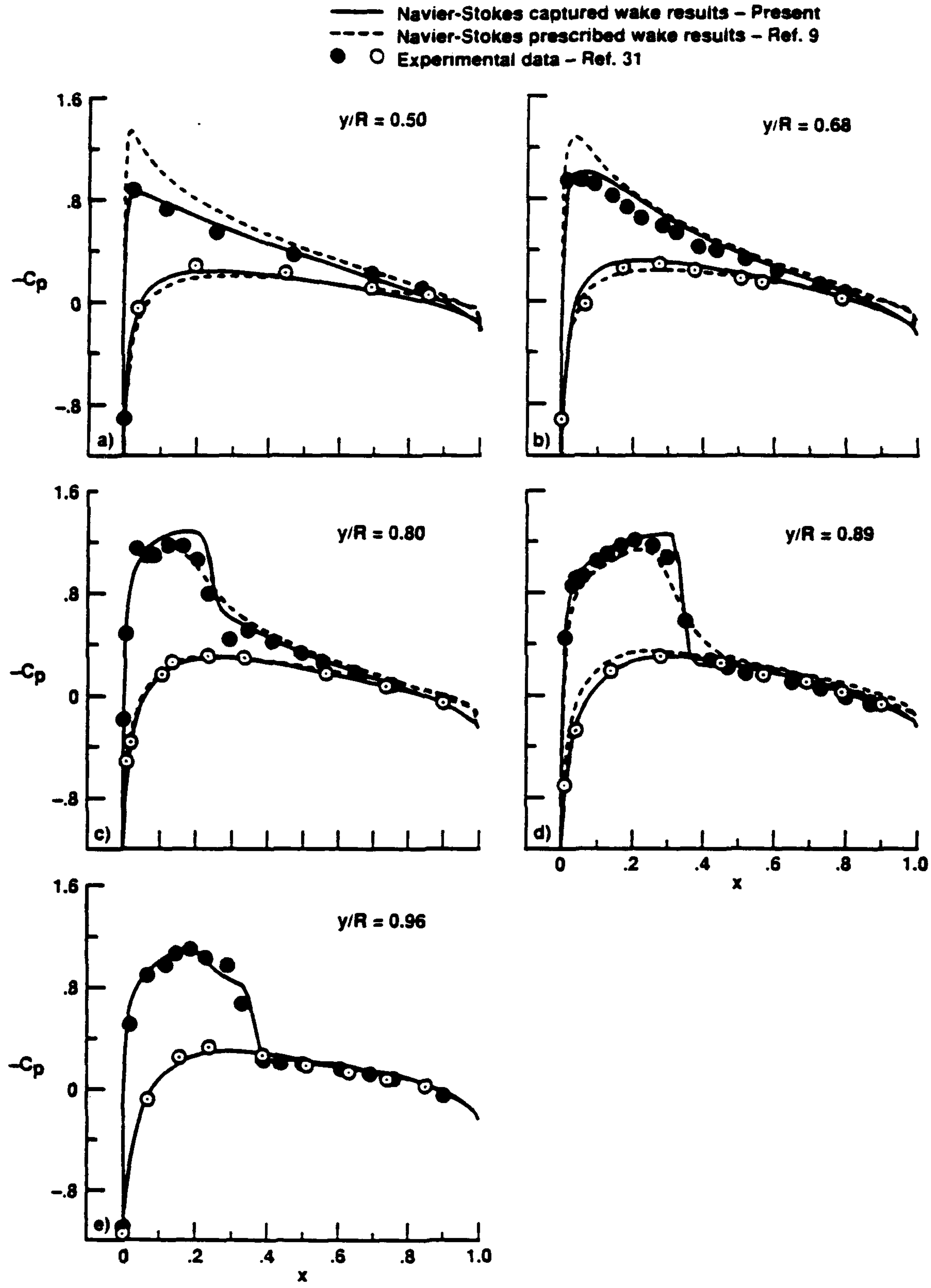

Fig. 3 Comparison of surface pressures for a lifting rotor in hover; $M_{tip} = 0.877$, $\theta_c = 8°$, and $Re = 3.93 \times 10^6$.

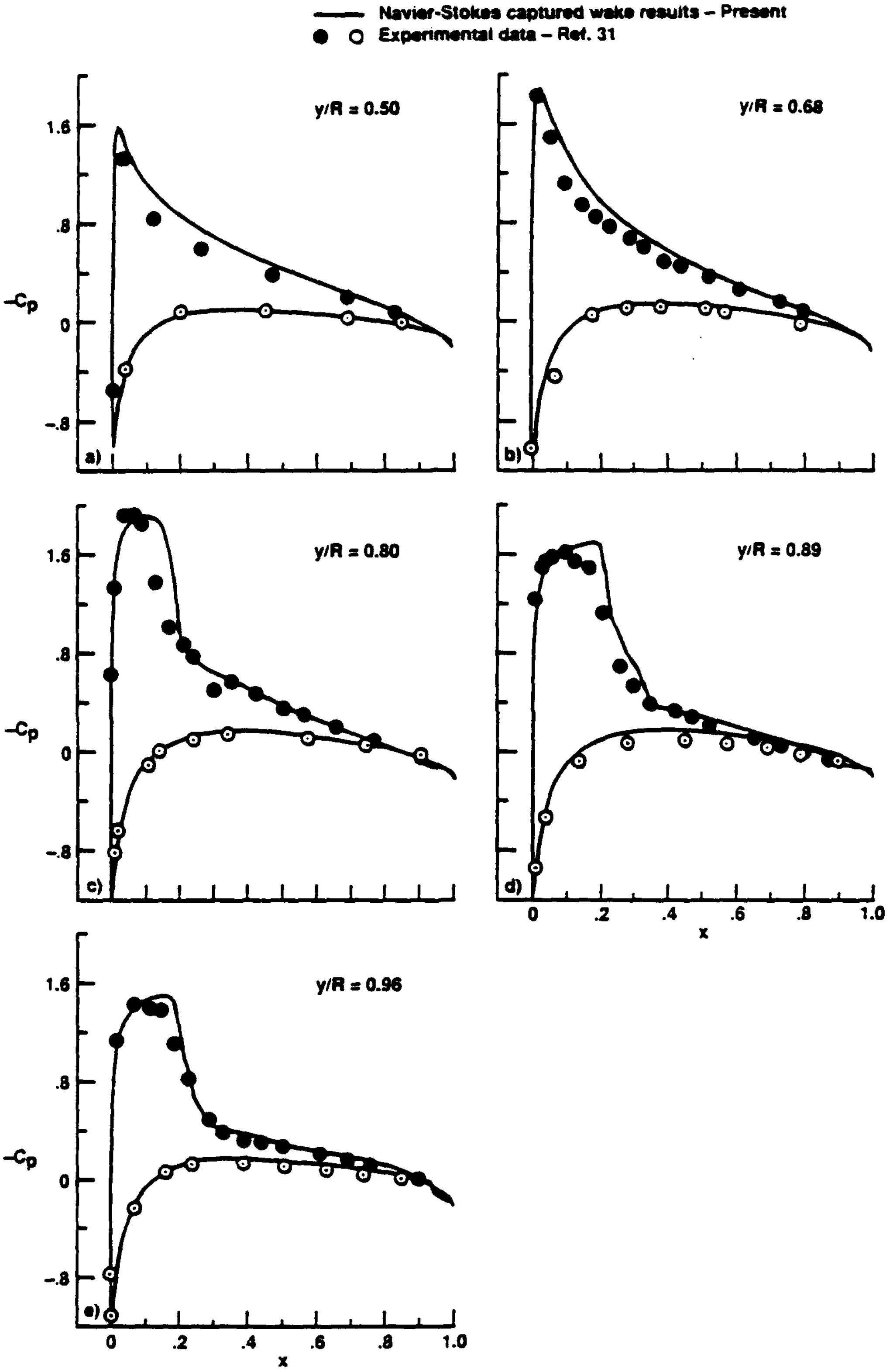

Fig. 4 Comparison of surface pressures for a lifting rotor in hover; $M_{tip} = 0.794$, $\theta_c = 12°$, and $Re = 3.55 \times 10^6$.

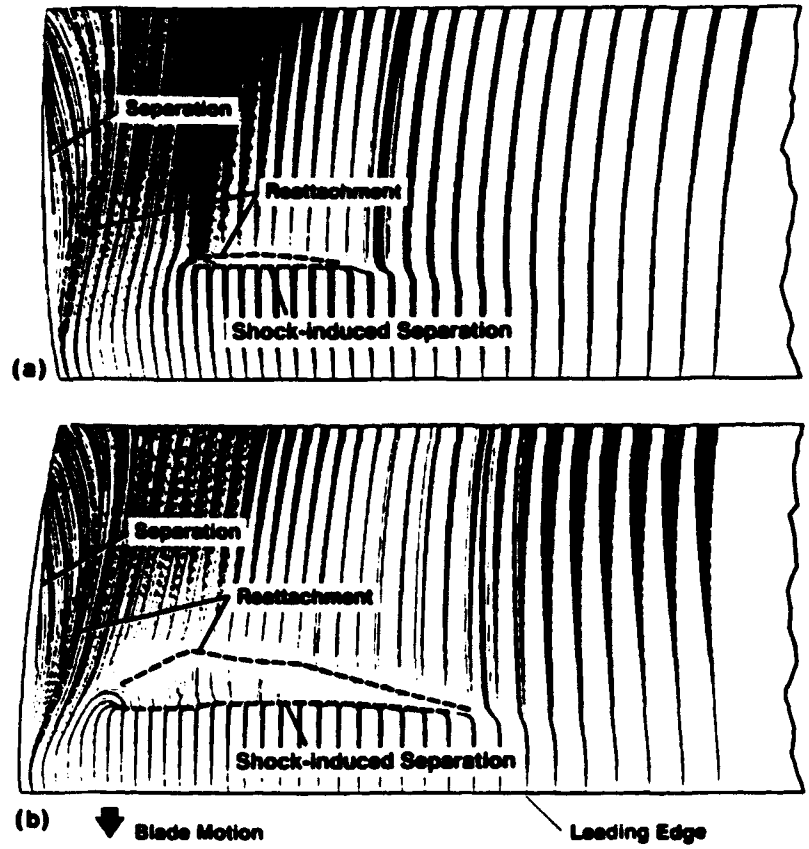
Separation
Reattachment
Shock-induced Separation
(a)
Separation
Reattachment
Shock-induced Separation
(b)
Blade Motion
Leading Edge

Fig. 5 Computed surface particle flow detail highlights the shock-induced boundary layer separation for the flow conditions of a) $M_{tip} = 0.877$, $\theta_c = 8°$, and $Re = 3.93\times10^6$, and b) $M_{tip} = 0.794$, $\theta_c = 12°$, and $Re = 3.55\times10^6$.

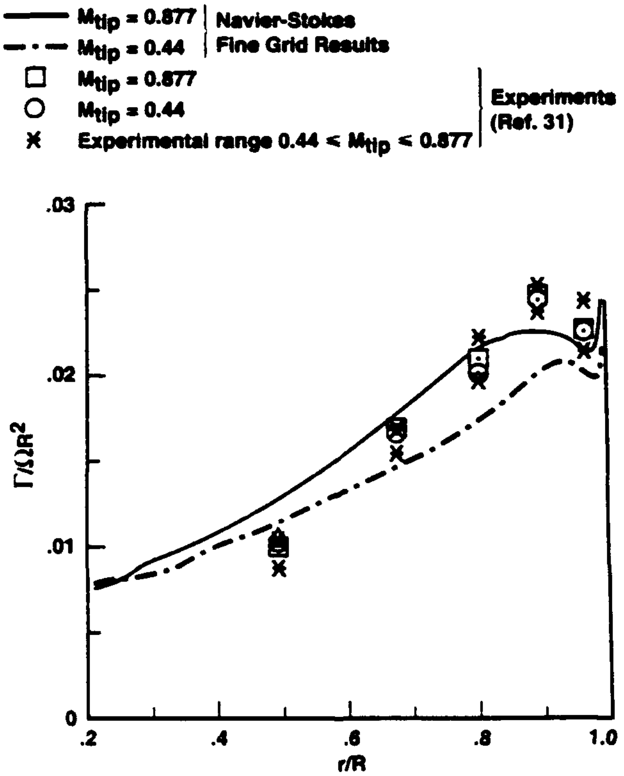

Fig. 6 Comparison of bound circulation distribution for the case of collective pitch $\theta_c = 8°$ with tip speeds of $M_{tip} = 0.44$ and 0.877.

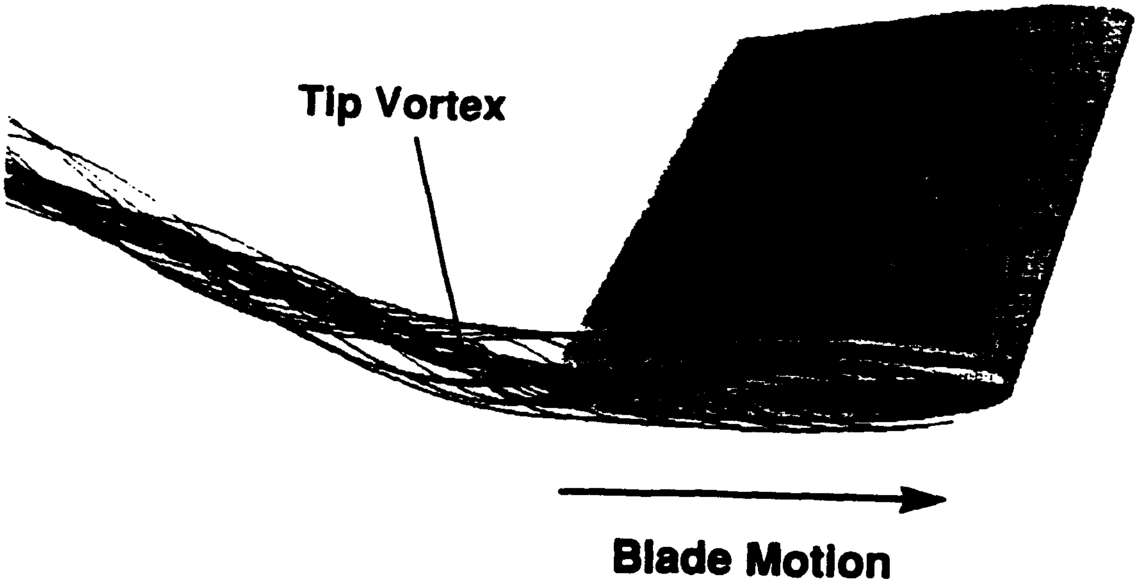

Fig. 7 Calculated tip vortex particle flow details showing the near-field view for the flow condition of $M_{tip} = 0.794$, $\theta_c = 12°$, and $Re = 3.55\times10^6$.

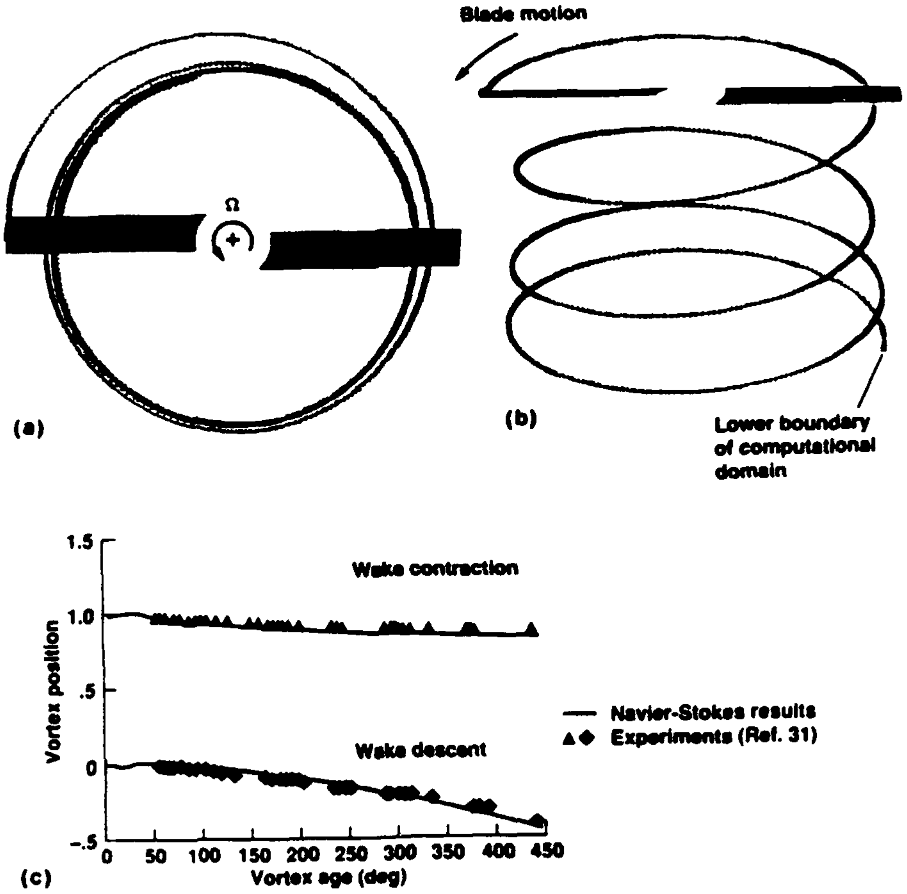

Fig. 8 Calculated tip vortex trajectory for the flow conditions of $M_{tip} = 0.44$, $\theta_c = 8°$, and $Re = 1.92\times10^6$; views show (a) contraction of wake (looking from the top), (b) captured tip vortex path and its vertical descent, and (c) comparison of the calculated trajectory over 450° of vortex age with experments.

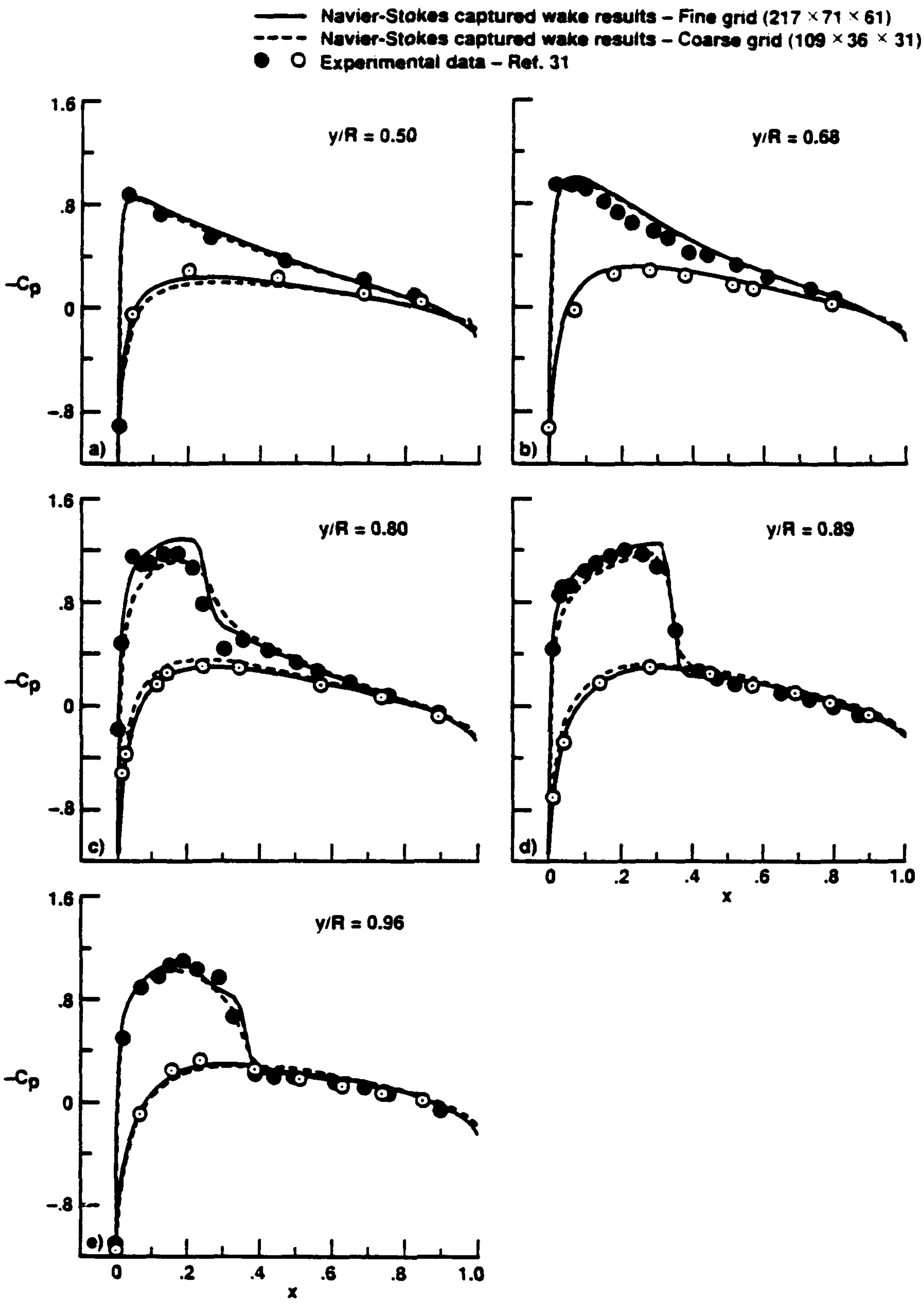

Fig. 9 Comparison of surface pressures with coarse and fine grids for the case of $M_{tip} = 0.877$, $\theta_c = 8°$, and $Re = 3.93\times10^6$.

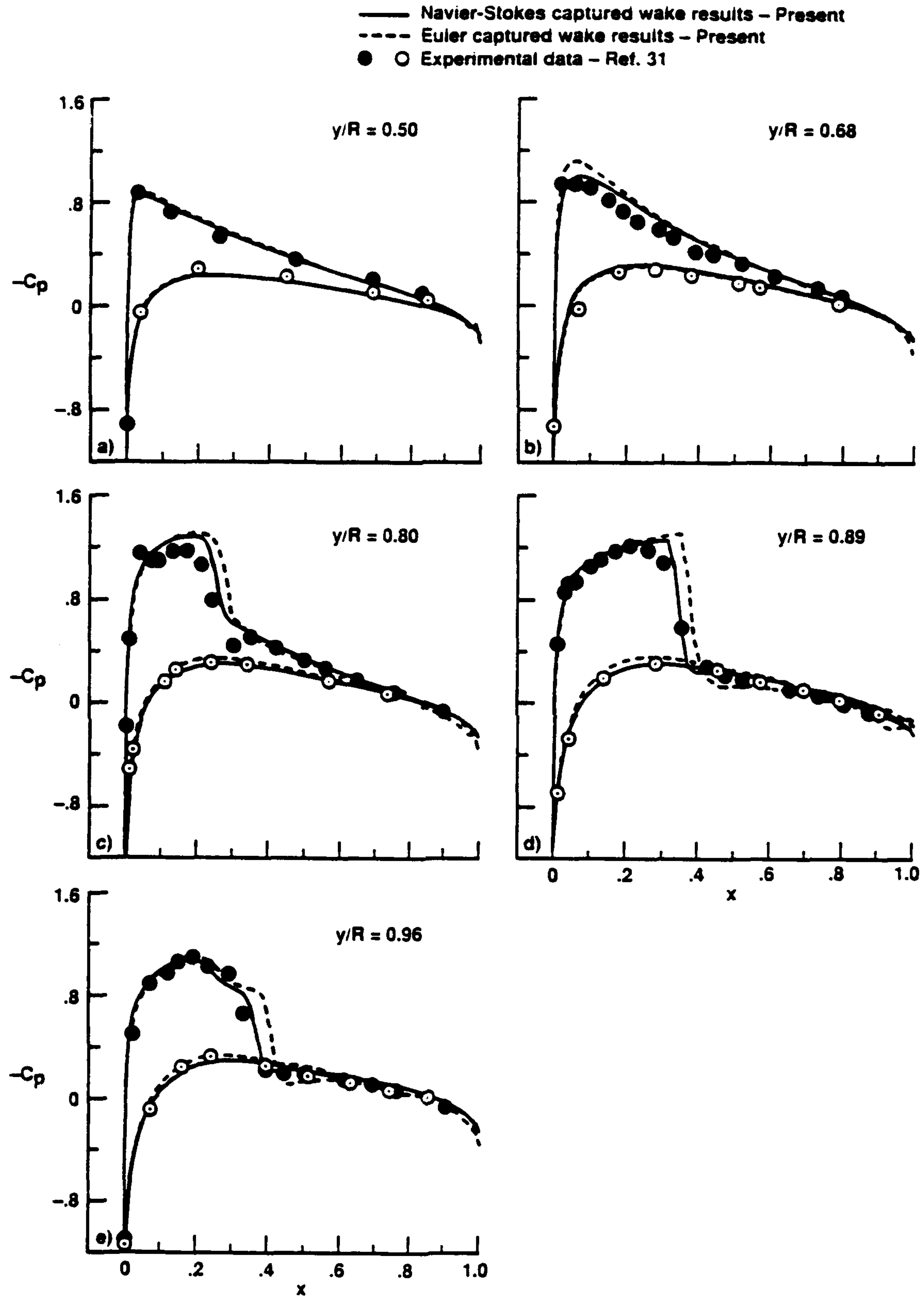

Fig. 10 Comparison of surface pressures for Euler and Navier-Stokes solutions; $M_{tip} = 0.877$, $\theta_c = 8°$, and $Re = 3.93\times10^6$.

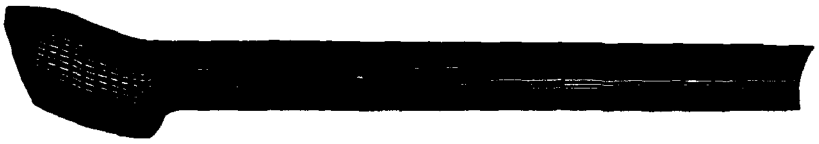

(a) BERP rotor blade

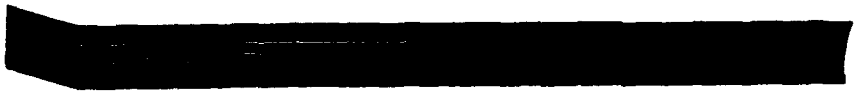

(b) UH-60A Black Hawk rotor blade

Fig. 11 Planform views and surface grids for the a) BERP and b) UH-60A rotor blades.

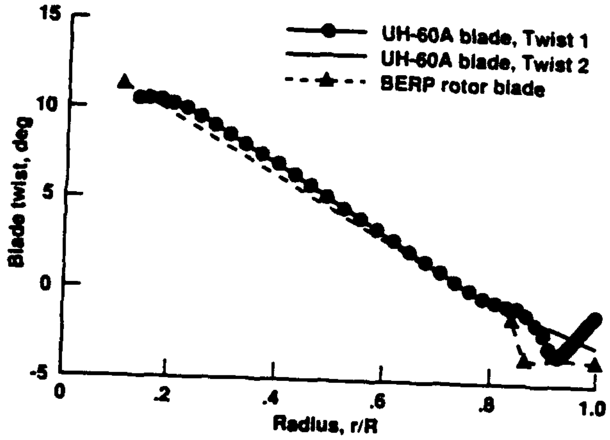

Fig. 12 Radial twist distributions for the UH-60A and BERP rotor blades.

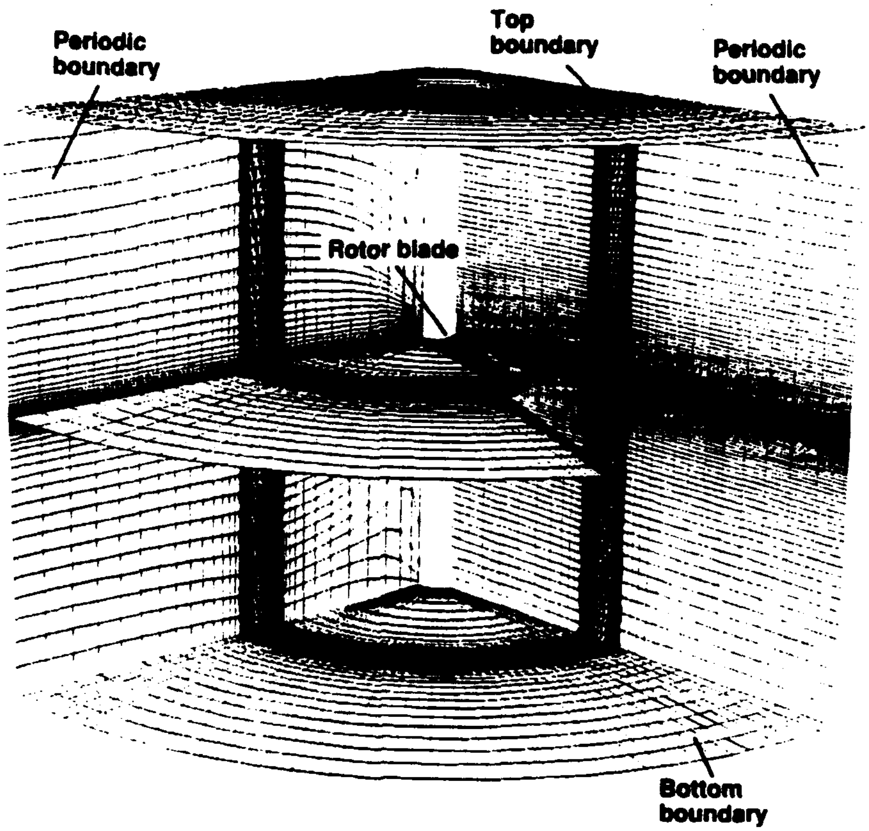
Periodic boundary
Top boundary
Periodic boundary
Rotor blade
Bottom boundary

Fig. 13 View of a C-H grid for a single BERP blade showing outer boundaries and grid in the plane of the blade.

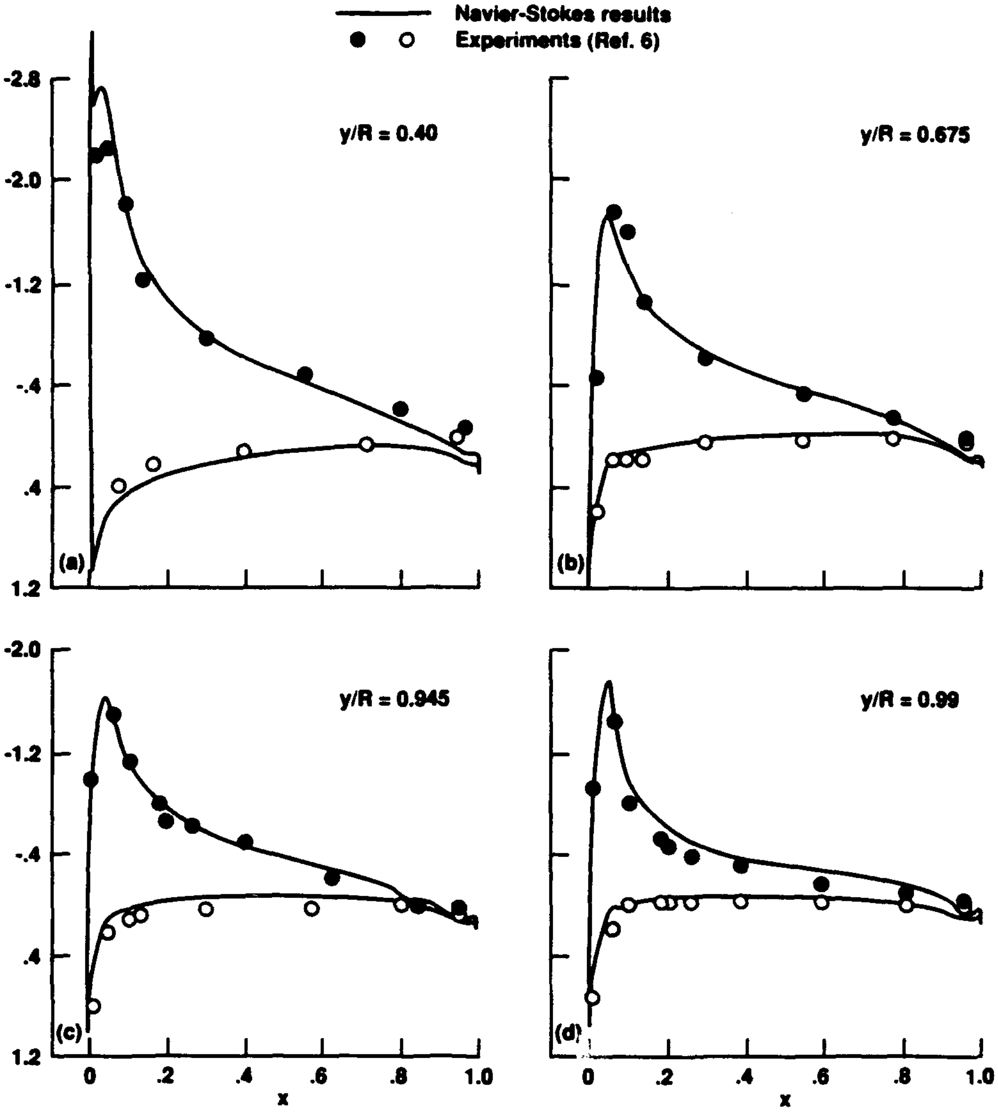

Fig. 14 Surface pressure distributions at various span stations for the UH-60A blade compared with experiments. $M_{tip} = 0.628$, Re = 2.75 x 10^6, and calculated $C_T/\sigma = 0.084$.

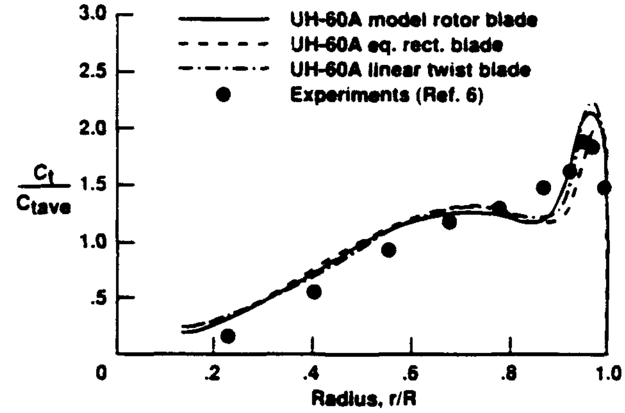

Fig. 15 Sectional thrust loading for the UH-60A blade, equivalent UH-60A rectangular blade, and the UH-60A blade with linear twist distribution in the tip region. $M_{tip} = 0.628$, $\theta_c = 9°$, and Re = 2.75 x 10^6.

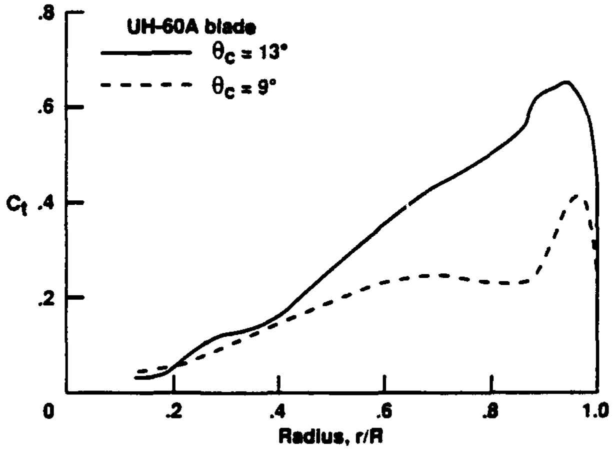

Fig. 16 Comparison of calculated sectional thrust loading for the UH-60A blade for two thrust conditions. $M_{tip} = 0.628$, and Re = 2.75 x 10^6.

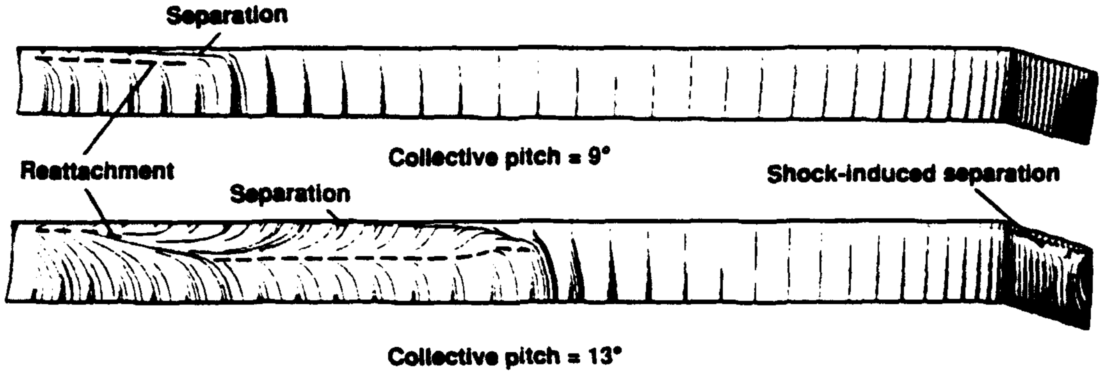
Separation
Reattachment
Collective pitch = 9°
Shock-induced separation
Separation
Collective pitch = 13°

Fig. 17 Upper surface particle flow (skin friction) patterns of UH-60A blade for $\theta_c = 9°$ and 13° cases at $M_{tip} = 0.628$ and Re = 2.75 x 10^6.

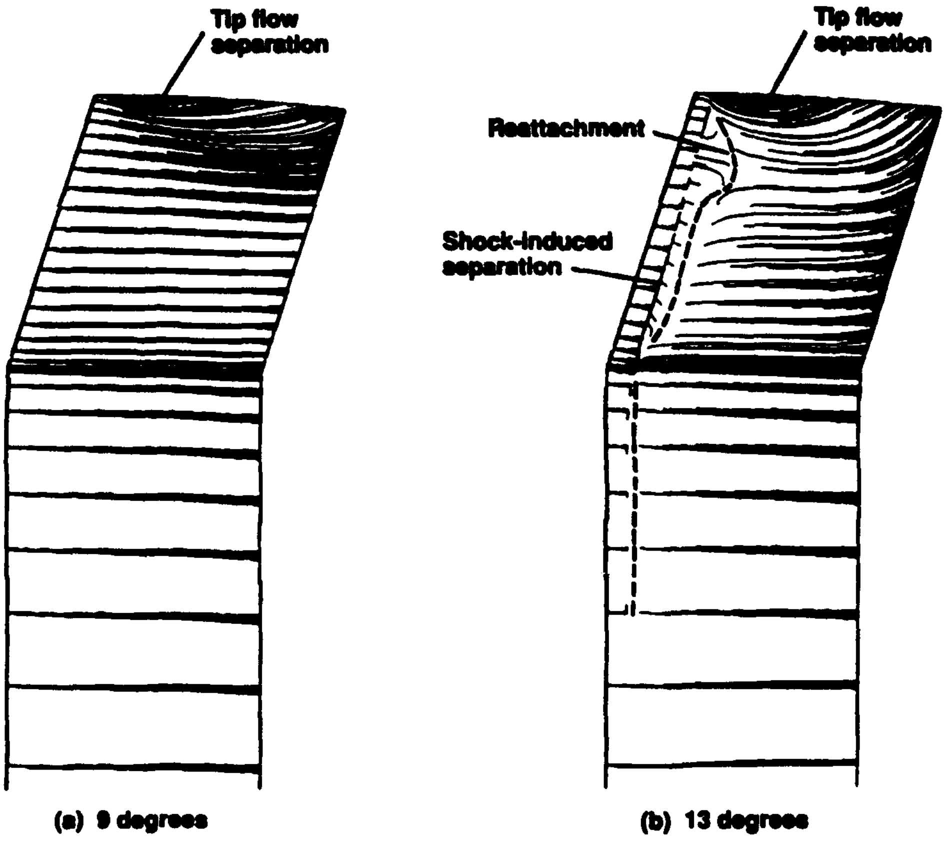
Tip flow separation
Tip flow separation
Reattachment
Shock-induced separation

(a) 9 degrees

(b) 13 degrees

Fig. 18 Close-up view of surface particle flow in the tip region for the UH-6A0 blade at $\theta_c = 9°$ and $\theta_c = 13°$. $M_{tip} = 0.628$, and Re = 2.75 x 10^6.

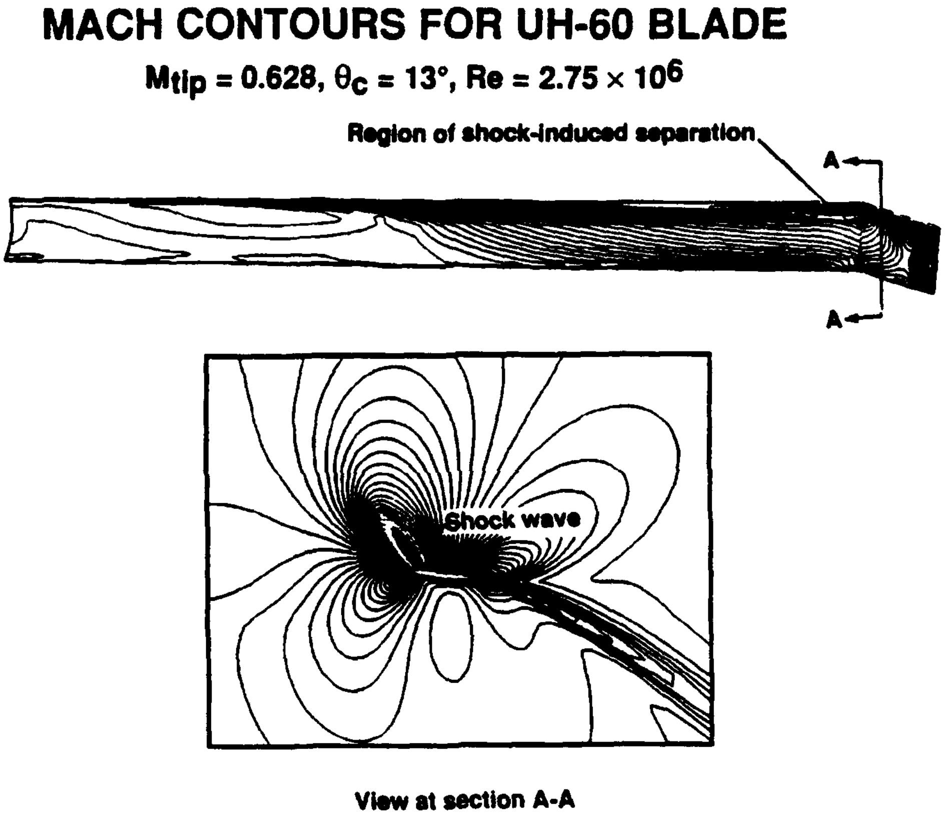
MACH CONTOURS FOR UH-60 BLADE

$M_{tip} = 0.628$, $\theta_C = 13°$, $Re = 2.75 \times 10^6$

Fig. 19 Mach contours for the UH-60A blade for the conditions of $M_{tip} = 0.628$, $\theta_c = 13°$, and $\mathrm{Re} = 2.75 \times 10^6$. Views show upper surface contours at $L = 8$ (away from the wall), and cross-sectional plane at $r/R = 0.94$.

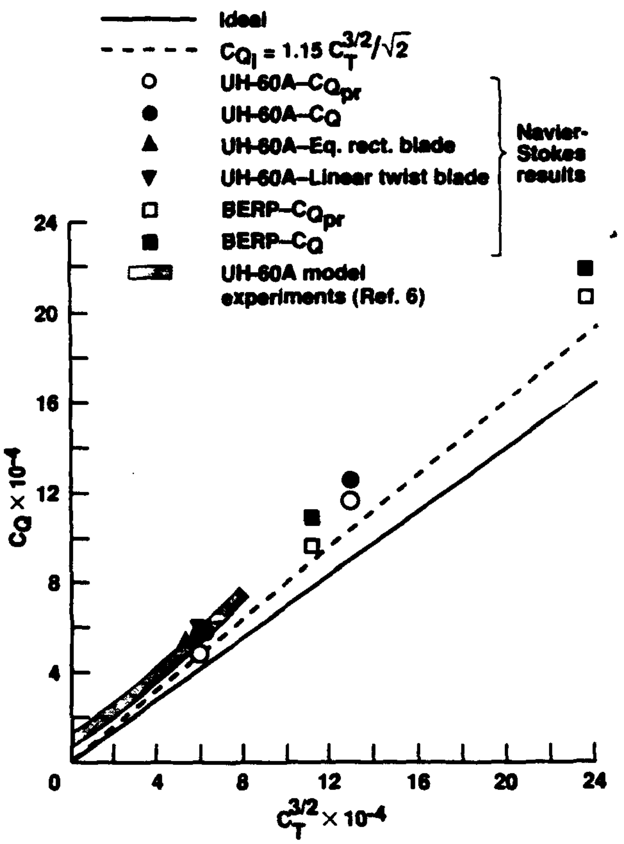

Fig. 20 Comparison of calculated and experimental hover performance for four-bladed UH-60A Blackhawk and BERP rotors.

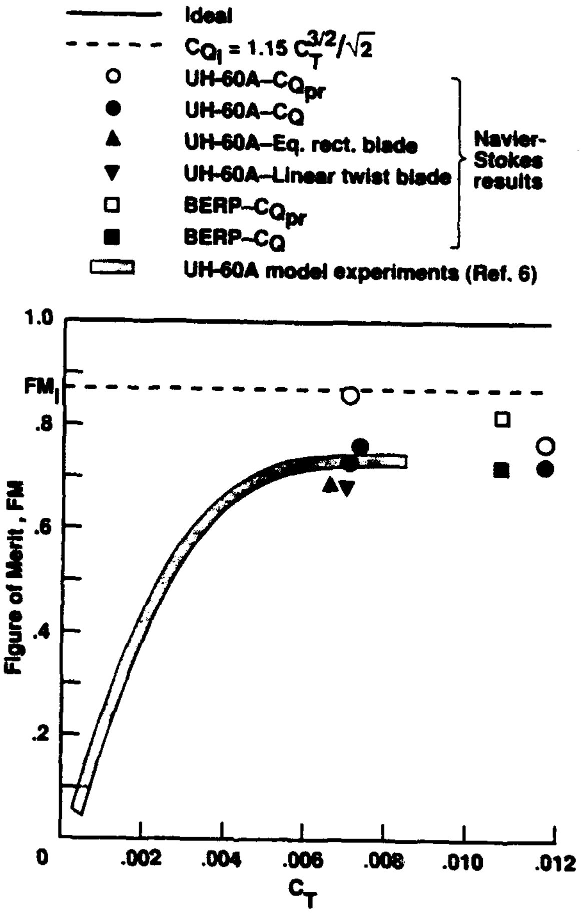

Fig. 21 Comparison of calculated and experimental Figure of Merit for four-bladed UH-60A Blackhawk and BERP rotors.

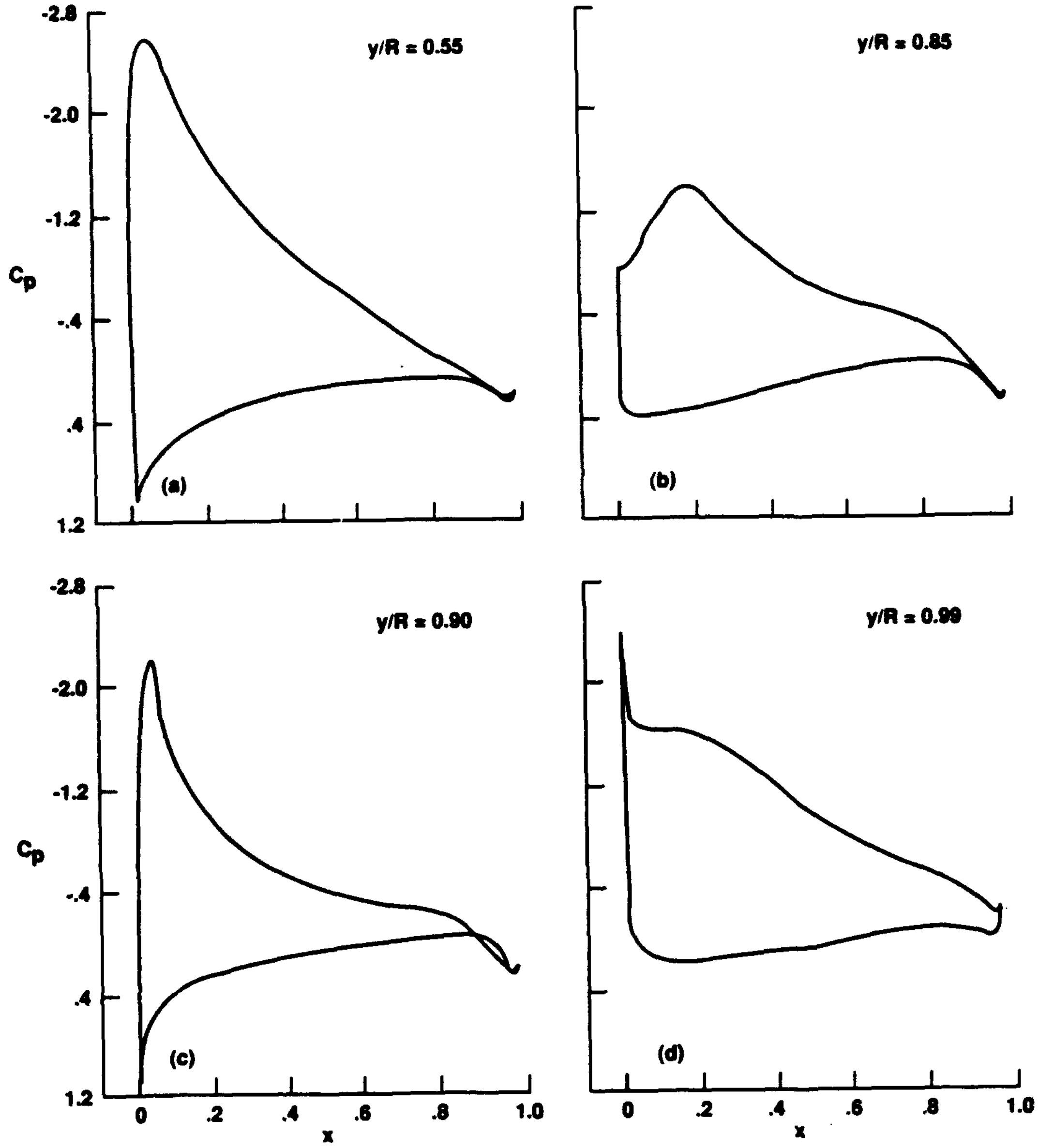

Fig. 22 Surface pressure distributions for the BERP rotor blade at different span stations; $M_{tip} = 0.628$, $\theta_c = 13°$ and Re = 2.94×10^6.

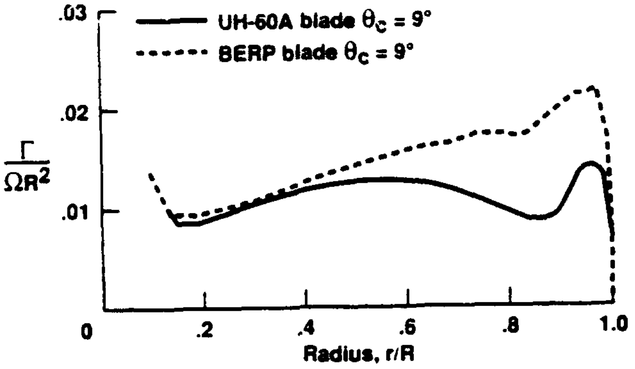

Fig. 23 Radial circulation distributions for the UH-60A and BERP blades at a collective pitch setting of $\theta_c = 9°$ with $M_{tip} = 0.628$.

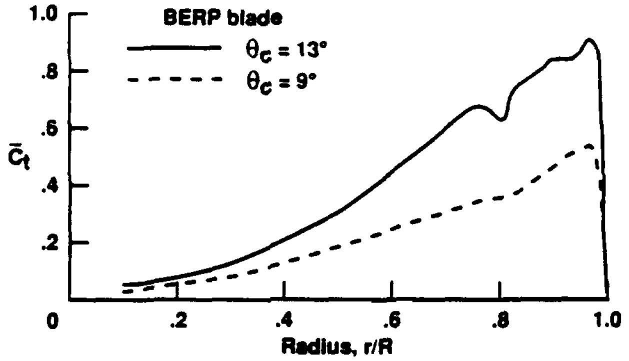

Fig. 24 Comparison of radial thrust loadings for the BERP blade at $\theta_c = 9°$ and 13° with $M_{tip} = 0.628$ and Re = 2.94 x 10^6.

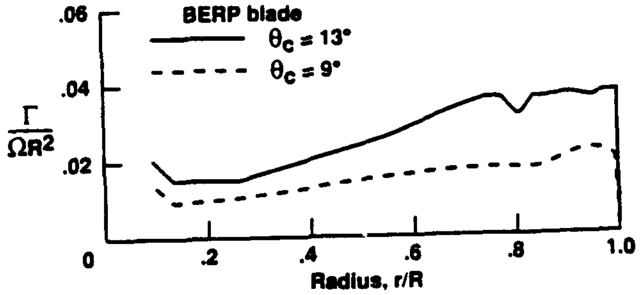

Fig. 25 Bound circulation distributions for the BERP blade for the conditions of Fig. 24.

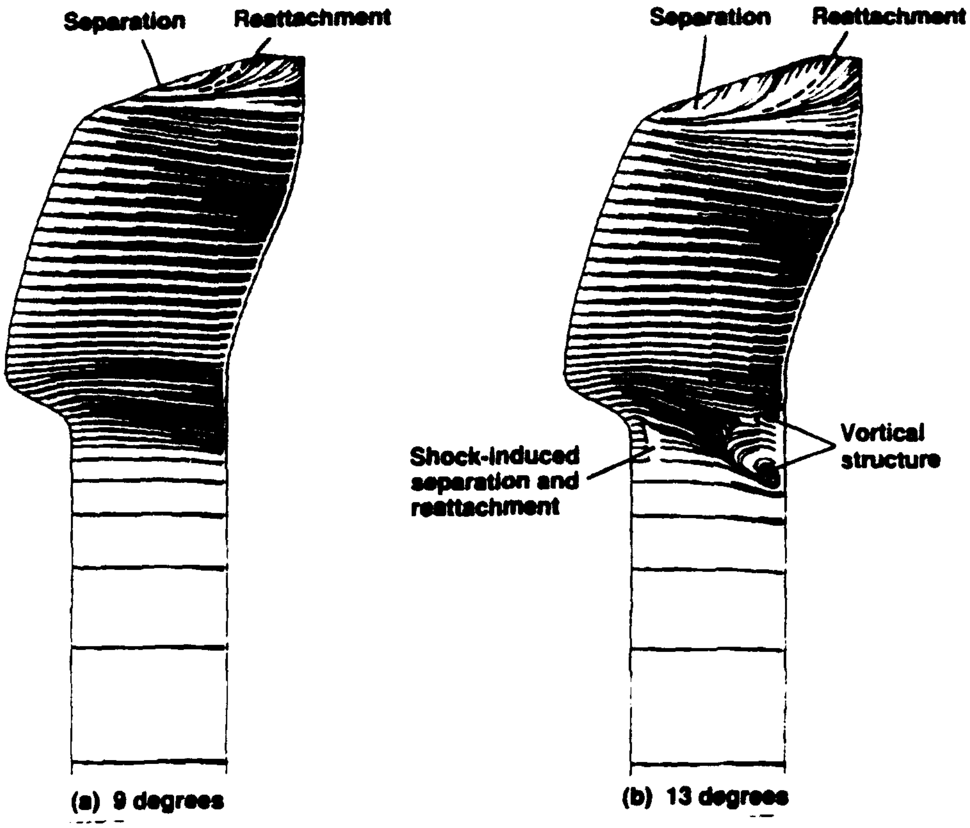
Separation
Reattachment
Separation
Reattachment
Vortical structure
Shock-induced separation and reattachment
(a) 9 degrees
(b) 13 degrees

Fig. 26 Upper surface particle flow details for the BERP blade at $\theta_c = 9°$ and $13°$; $M_{tip} = 0.628$ and Re = 2.94 x 10^6.

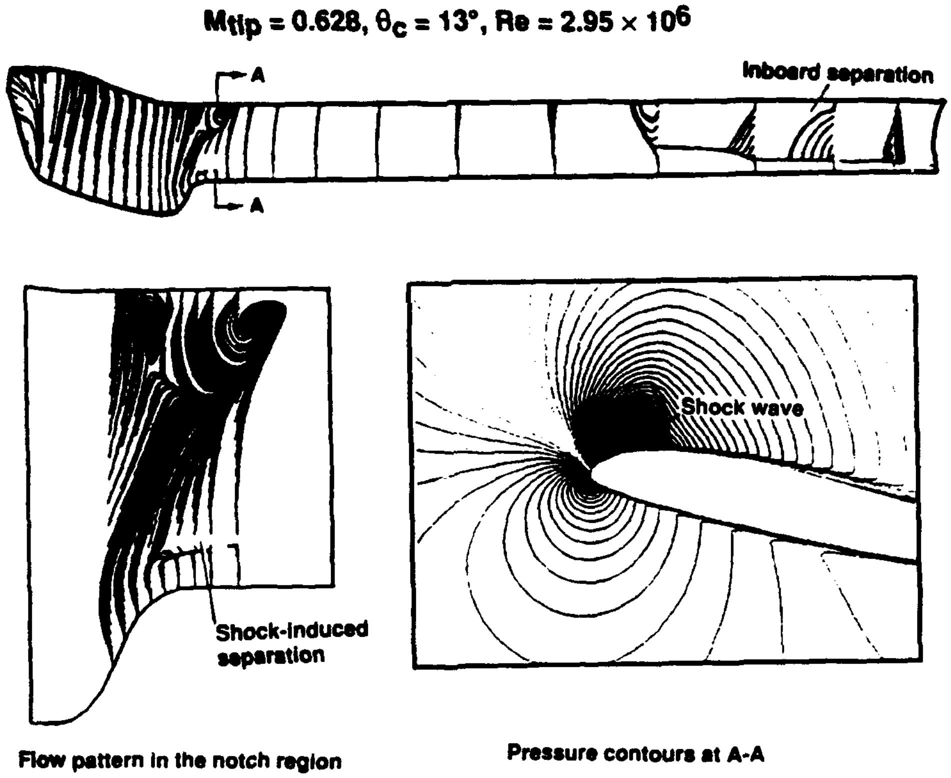
Mtip = 0.628, θc = 13°, Re = 2.95 × 10^6
A
A
Inboard separation
Shock-induced separation
Shock wave
Flow pattern in the notch region
Pressure contours at A-A

Fig. 27 Upper surface particle flow pattern and pressure contours at the notch region for the BERP blade at $M_{tip} = 0.628$, $\theta_c = 13°$, and Re = 2.94 x 10^6.

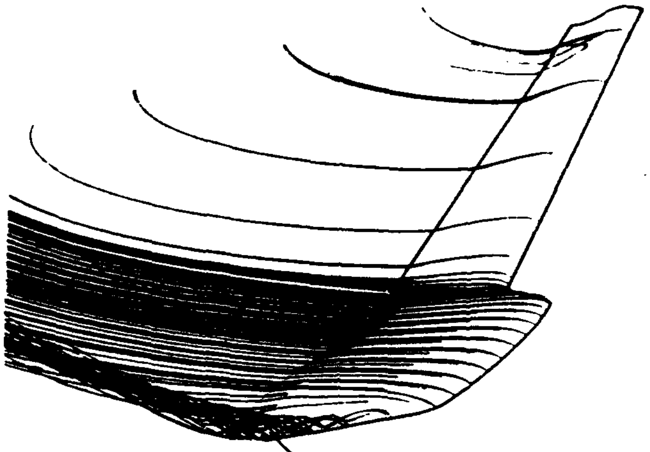

Fig. 28 Near-field view of tip vortex formation and roll-up process for the BERP blade at $\theta_c = 13°$, $M_{tip} = 0.628$.

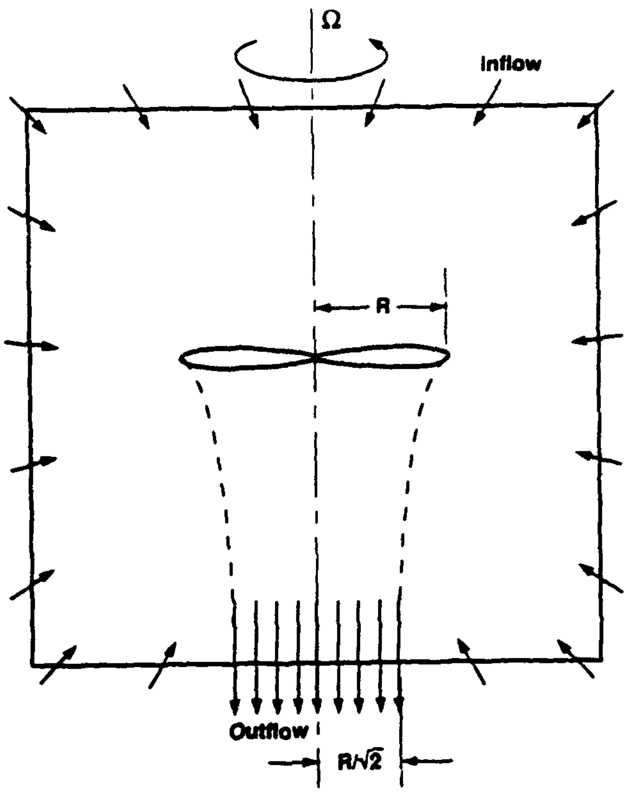

Fig. 29 Schematic of new farfield boundary conditions for the hovering rotor.

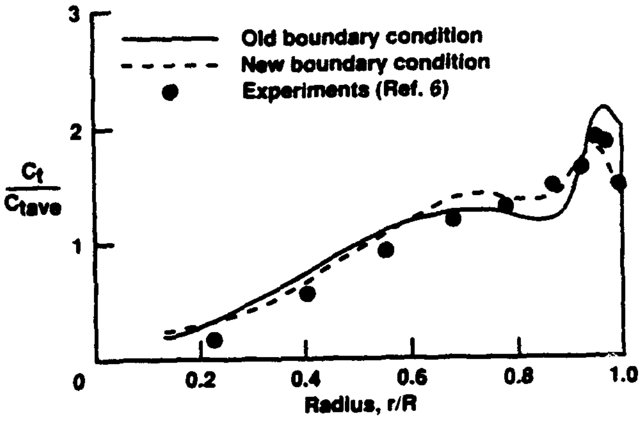

Fig. 30 Sectional thrust distributions for the UH-60A blade with old and new farfield boundary conditions compared with experimental data. $M_{tip} = 0.628$, $\theta_c = 9°$, and $Re = 2.75 \times 10^6$.

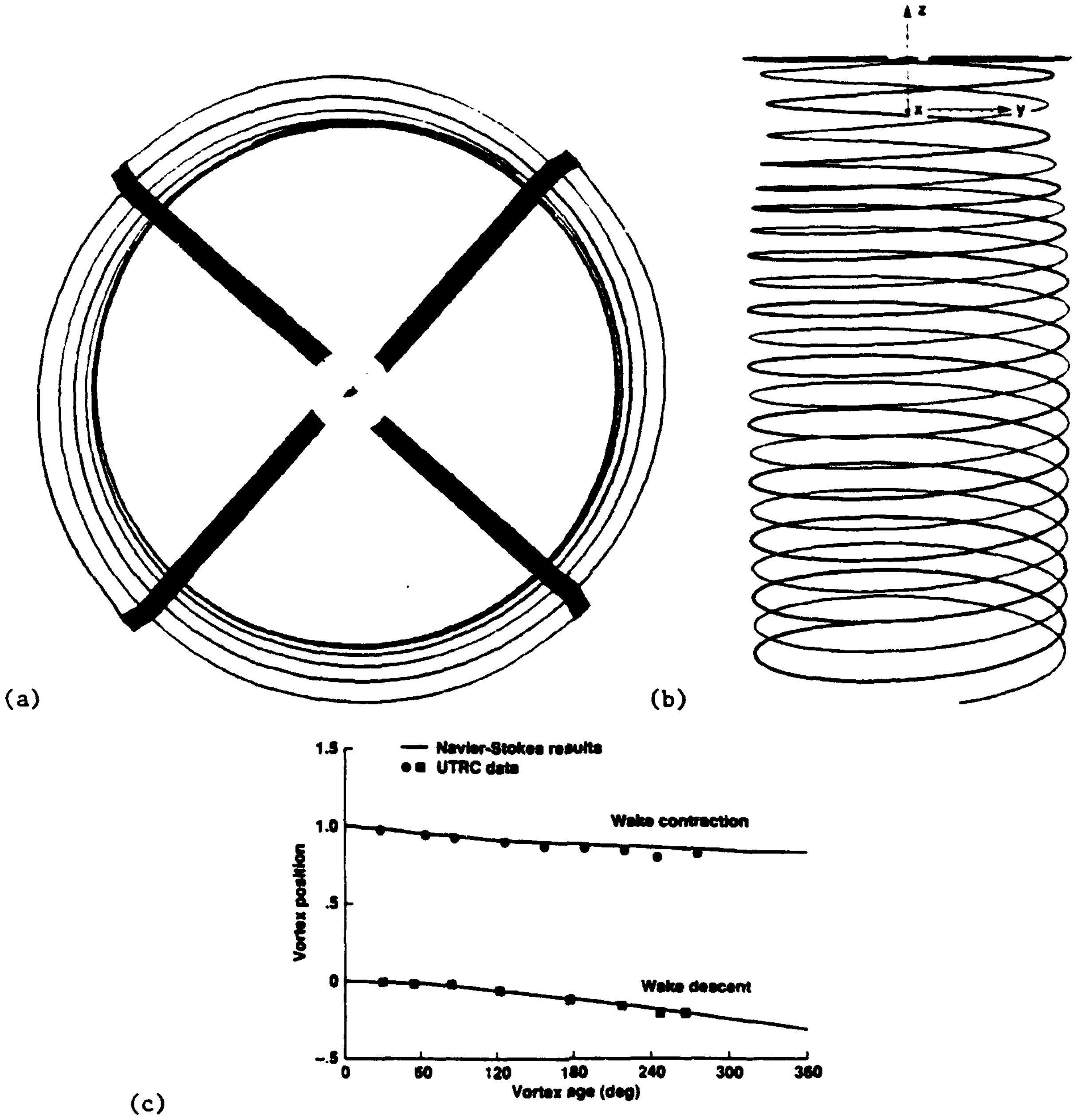

Fig. 31 Calculated wake contraction and descent for the 4-bladed UH-60A Black Hawk rotor. Views show (a) planform view of wake contraction looking from top; (b) wake contraction and descent looking from side; and (c) comparison calculated results with experimental data for the flow condition of $M_{tip} = 0.628$, $\theta_c = 9°$, and $Re = 2.75 \times 10^6$.

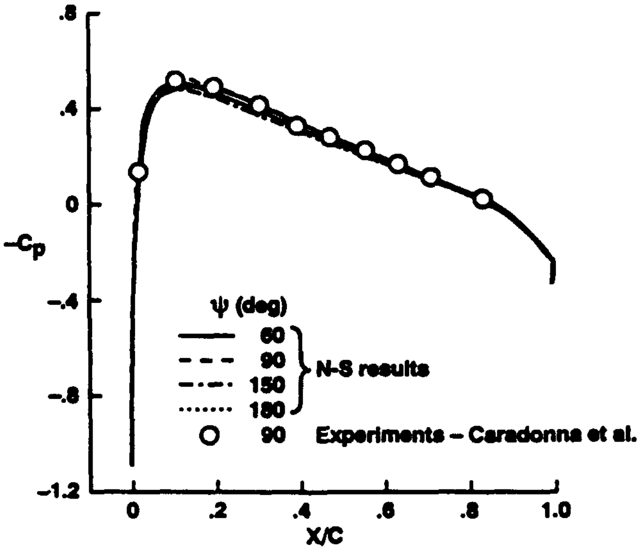

Fig. 32 Comparison of instantaneous surface pressures for a nonliftng two-bladed rotor in forward flight. $M_{tip} = 0.6$, $\mu = 0.2$, and $Re = 2.22\text{x}10^6$ at $r/R = 0.893$.

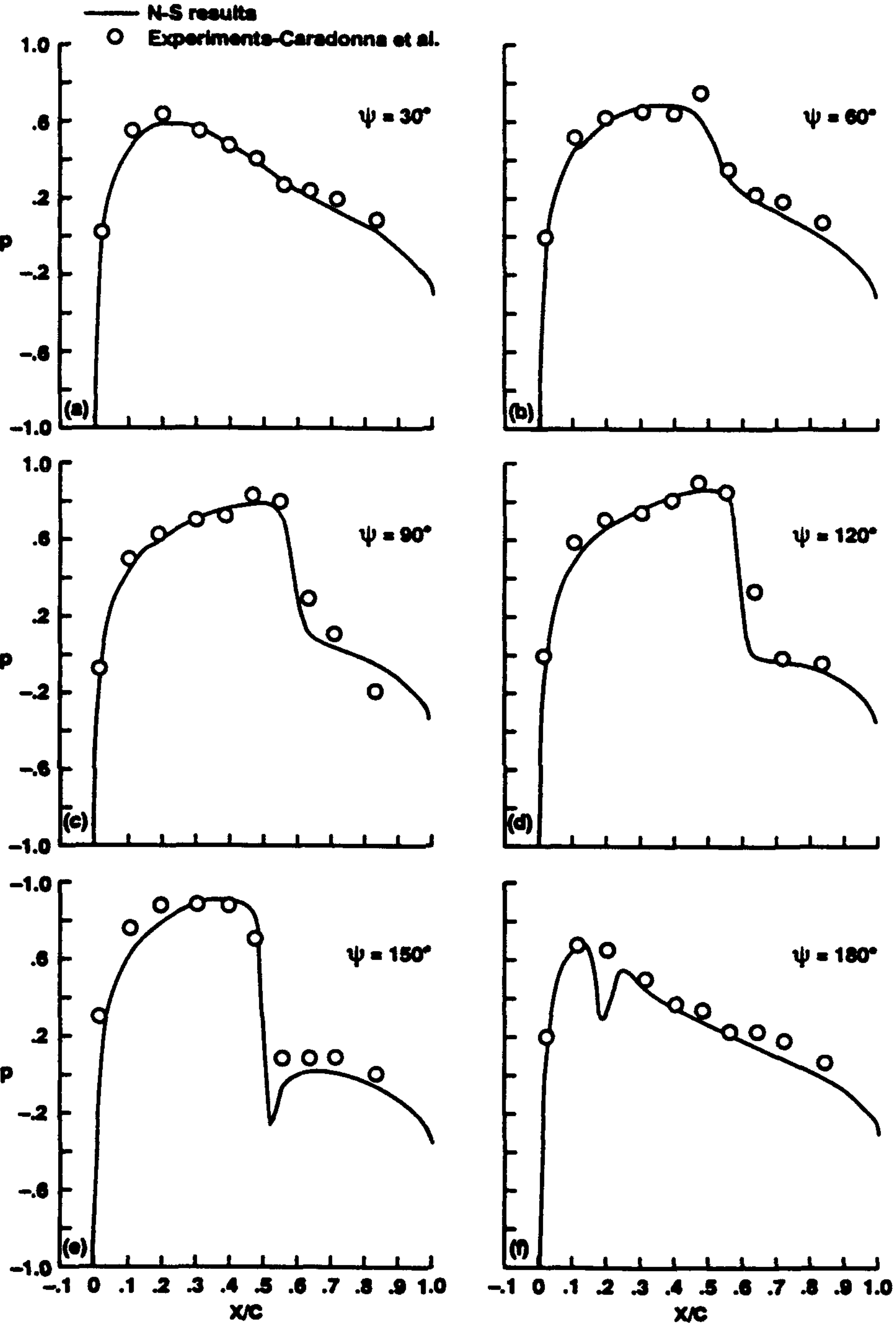

Fig. 33 Instantaneous surface pressures of a nonlifting rotor in forward flight at different azimuthal locations compared with experiments. $M_{tip} = 0.8$, $\mu = 0.2$, and $Re = 2.89\text{x}10^6$ at $r/R = 0.893$.

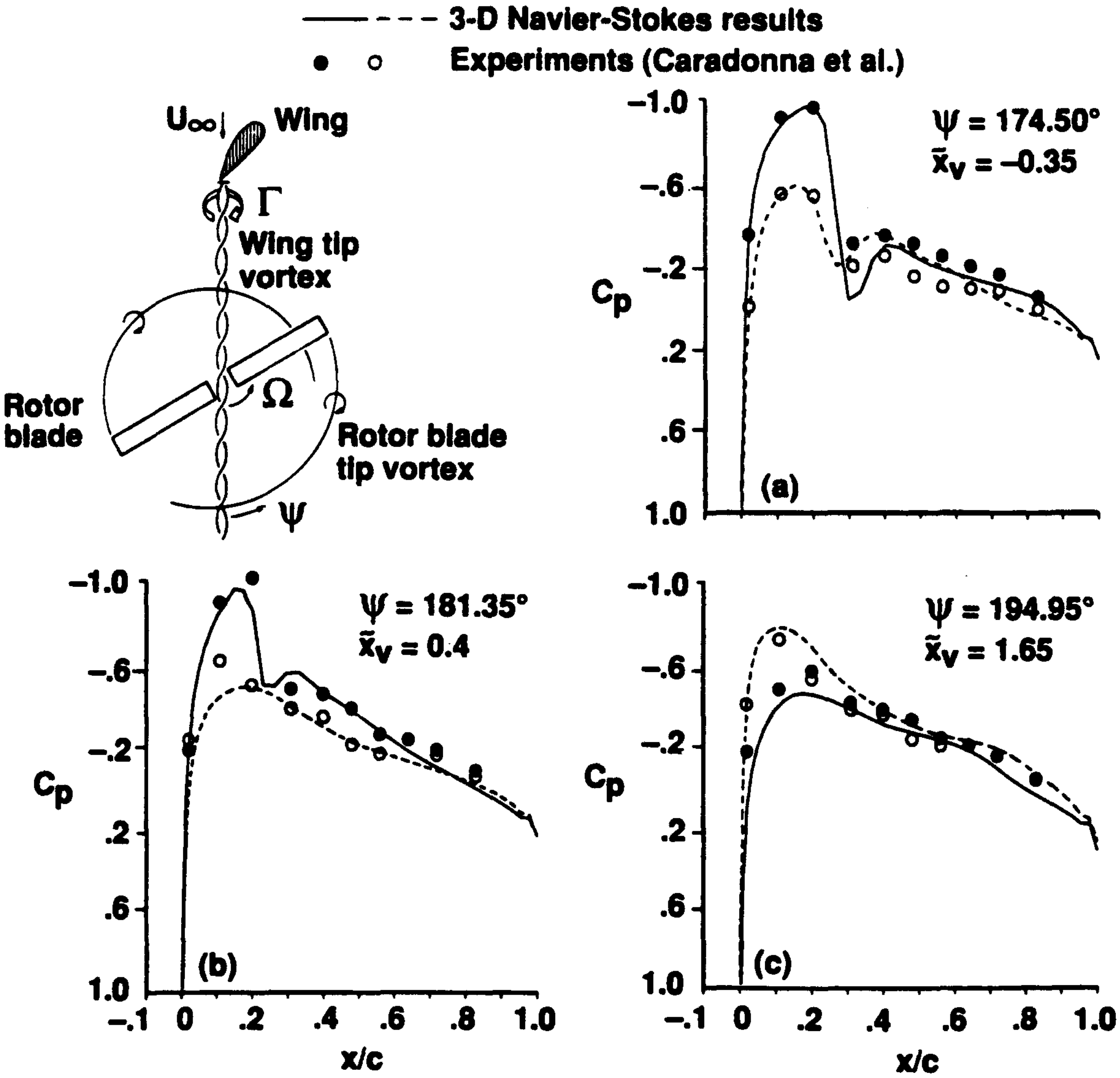

Fig. 34 Instantaneous surface pressures during transonic parallel BVI at $\Psi = 174.5°$ azimuth compared with experiments. $M_{tip} = 0.8$, $\mu = 0.2$, $Re = 2.89\text{x}10^6$, $\tilde{\Gamma} = 0.177$, $x_o = 0.0$, $z_o = -0.4$, at $r/R = 0.893$.

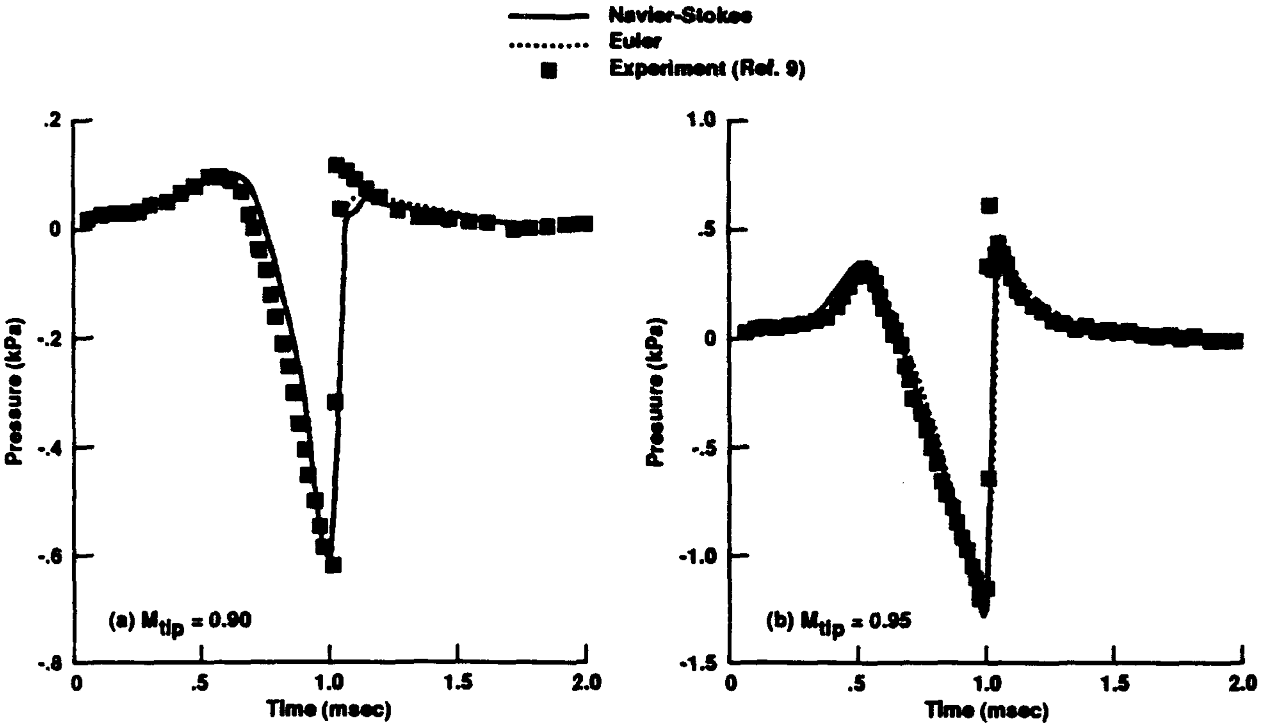

Fig. 35 Pressure-time histories of high-speed impulsive noise of a hovering rectangular blade rotor in-plane at $r/R = 3.09$ and at a blade-tip Mach number of (a) $M_{tip} = 0.90$, and (b) $M_{tip} = 0.95$.

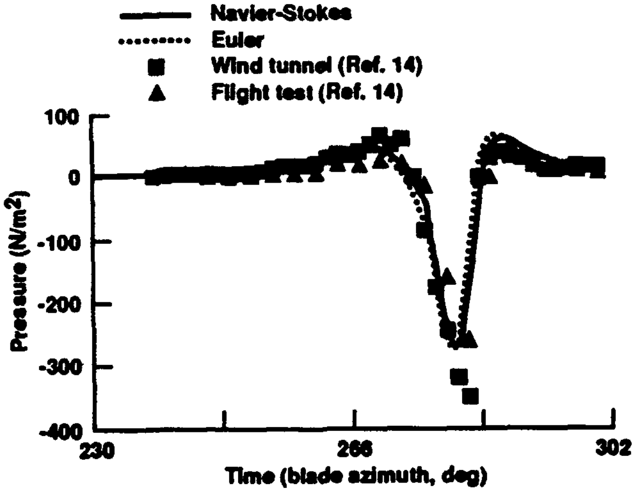

Fig. 36 Pressure-time histories of high-speed impulsive noise for an advancing rotor in-plane at 1.8 rotor diameters directly in front of the blade at $M_{tip} = 0.896$, $\mu = 0.348$, and $Re = 2.17\text{x}10^6$ compared to wind tunnel and flight test data.

TABLE 3: QUASI-STEADY AIRLOADS

Mean angle	$\alpha = 13°$			$\alpha = 17°$		
Airloads / Turb. model	c_l	c_d	c_m	c_l	c_d	c_m
B-L model	1.401	0.0209	0.0146	1.624	0.0559	0.0267
J-K model	1.175	0.0254	0.0371	1.093	0.0664	0.0391
B-B model	1.13	0.0295	0.0329	0.7466	0.1276	–0.0119
Experiments (Piziali)	1.15	0.0331	0.028	0.65–1.18	0.151	–0.028

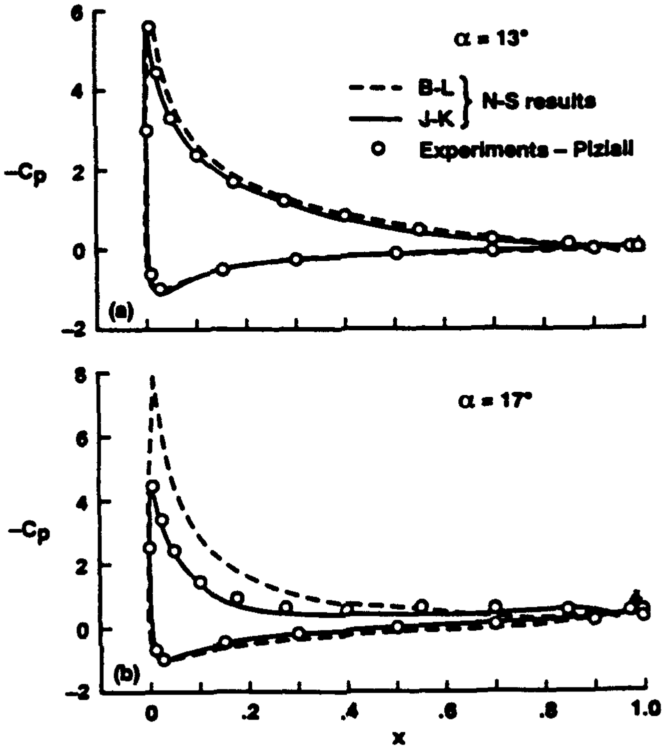

Fig. 37 Quasi-steady surface pressure distributions of NACA 0015 airfoil compared to experiments (Ref. 19) at flow conditions of $M_\infty = 0.29$, $Re = 1.95\text{x}10^6$; a) $\alpha = 11°$; b) $\alpha = 17°$.

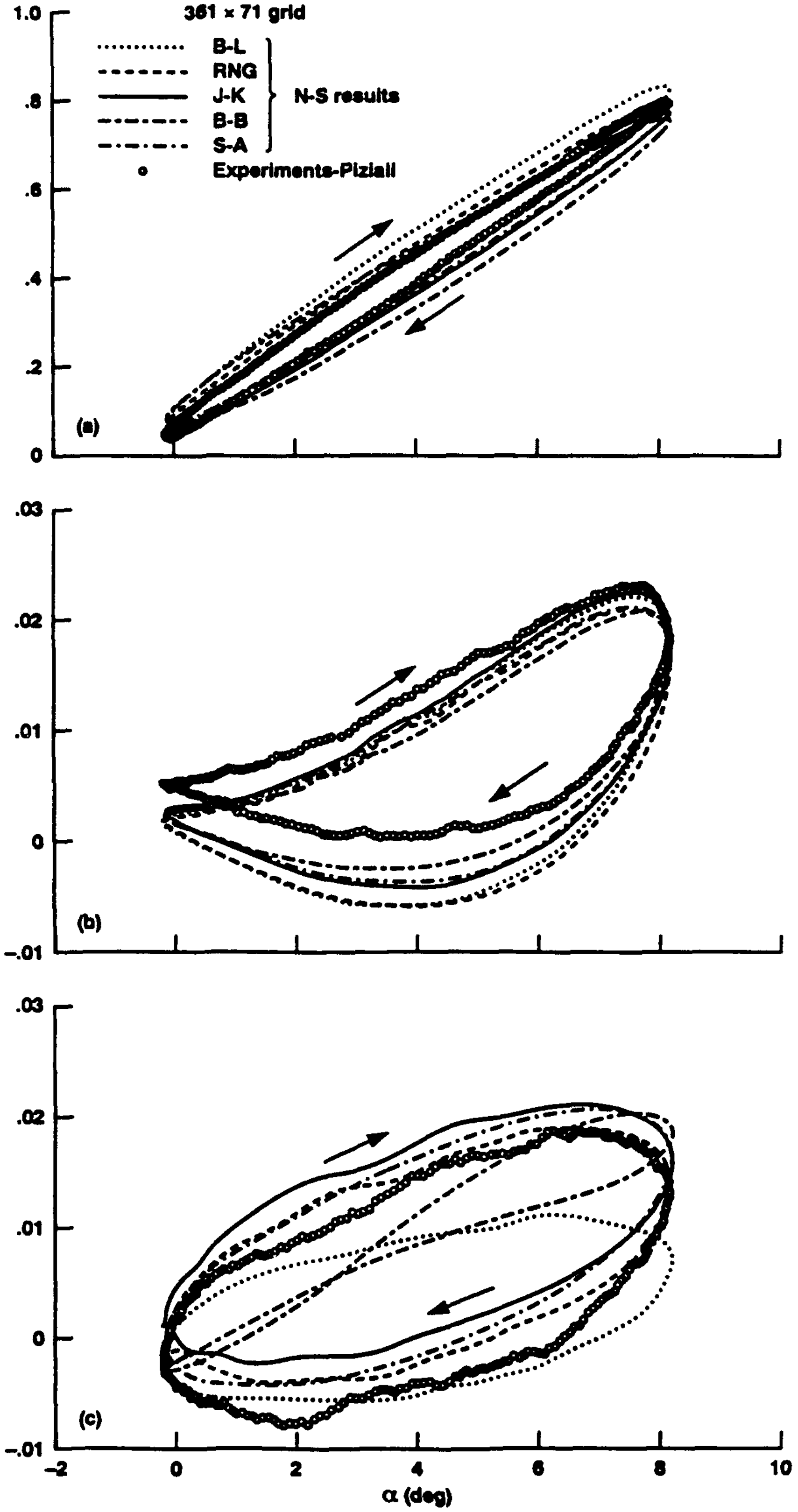

Fig. 38 Comparison of calculated unsteady airloads hysteresis of oscillating wing for different turbulence models with experiments. $M_\infty = 0.29$, $\alpha(t) = 4° + 4.2° sin(Kt)$, $k = 0.1$, $Re = 1.95\text{x}10^6$.

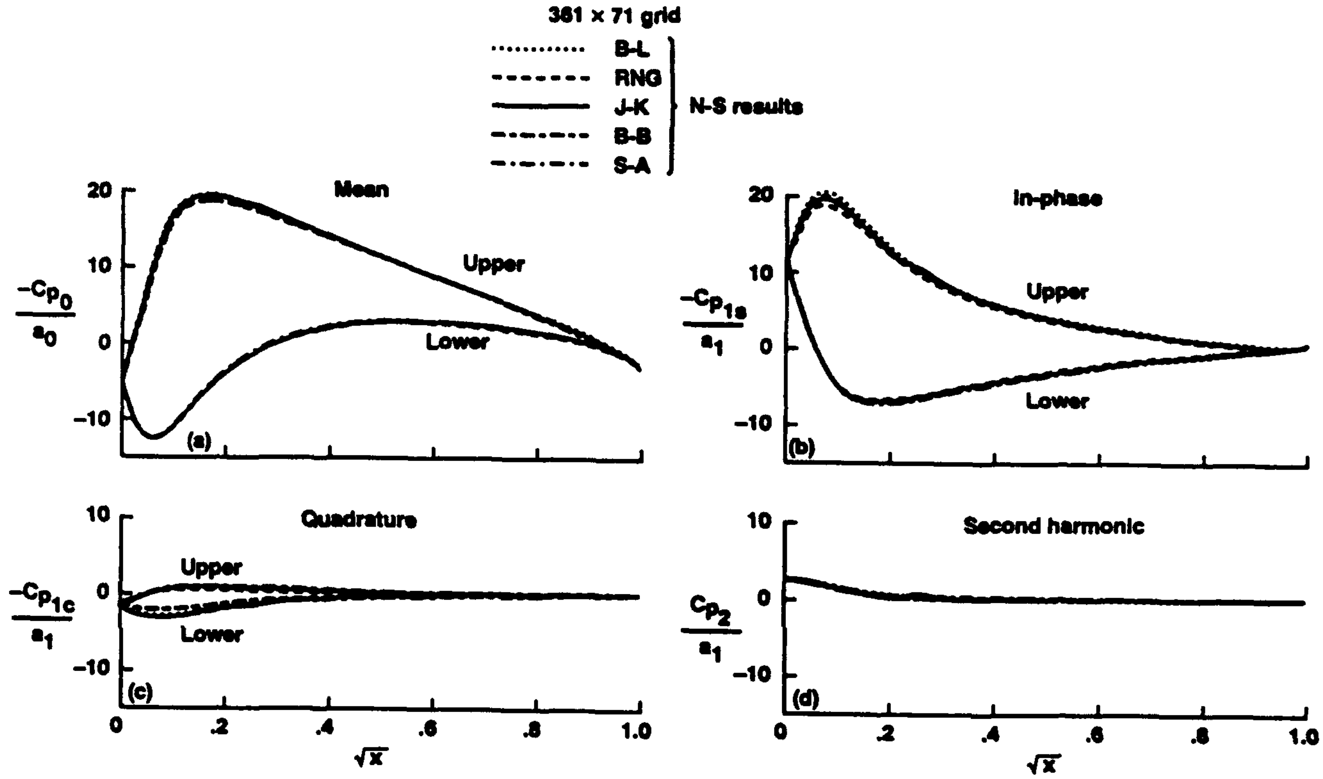

Fig. 39 Comparison of harmonic components of unsteady pressures for different turbulence models at the experimental conditions of Fig. 38.

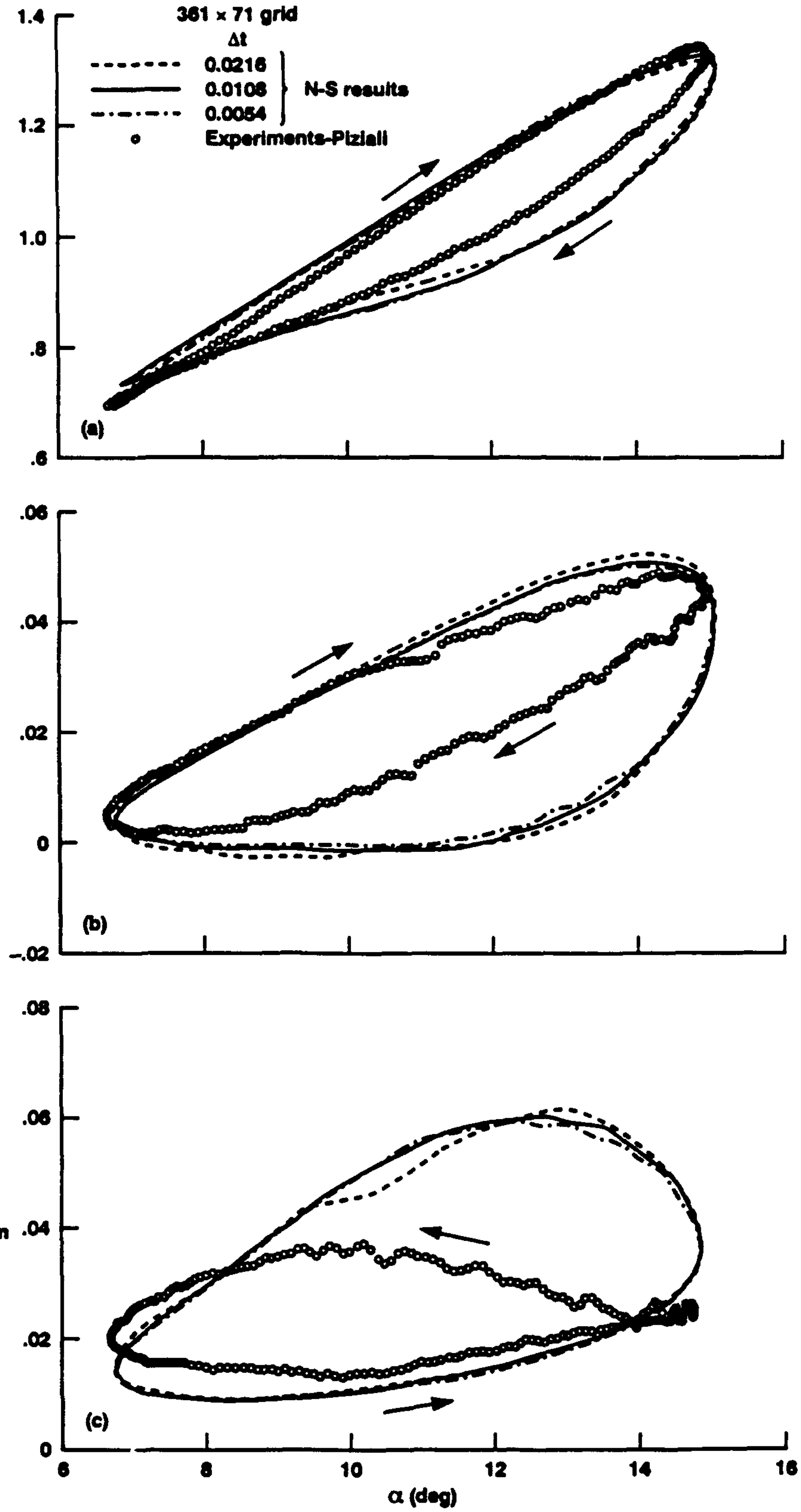

Fig. 40 Comparsion of unsteady airloads hysteresis for J-K model with different constant time-steps for the oscillating cycle and experiments. $M_\infty = 0.29$, $\alpha(t) = 11° + 4.2° sin(Kt)$, $k = 0.1$, and $Re = 1.95x10^6$.

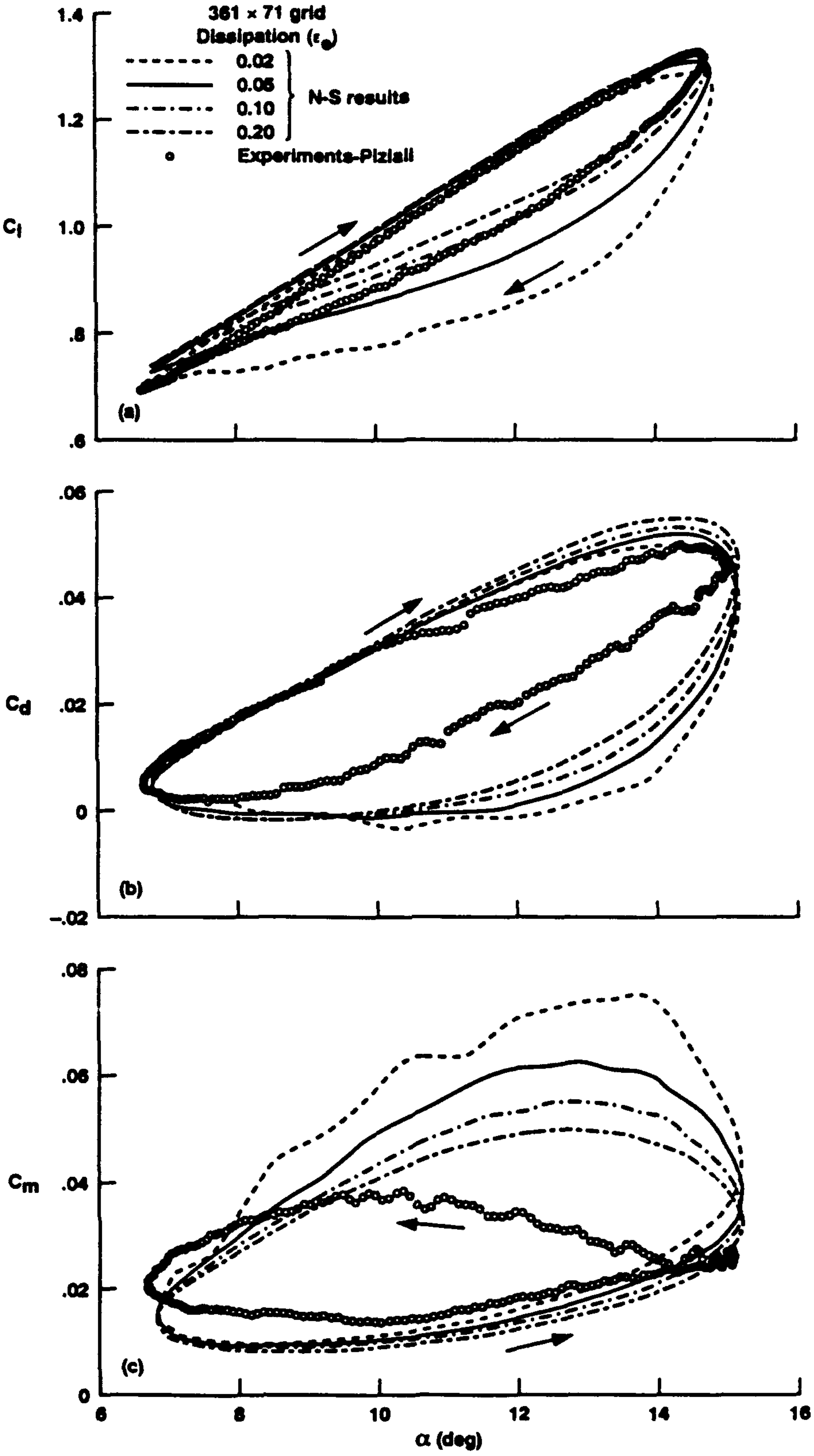

Fig. 41 Effect of numerical dissipation on the solution accuracy with J-K model for the experimental conditions of Fig. 40.

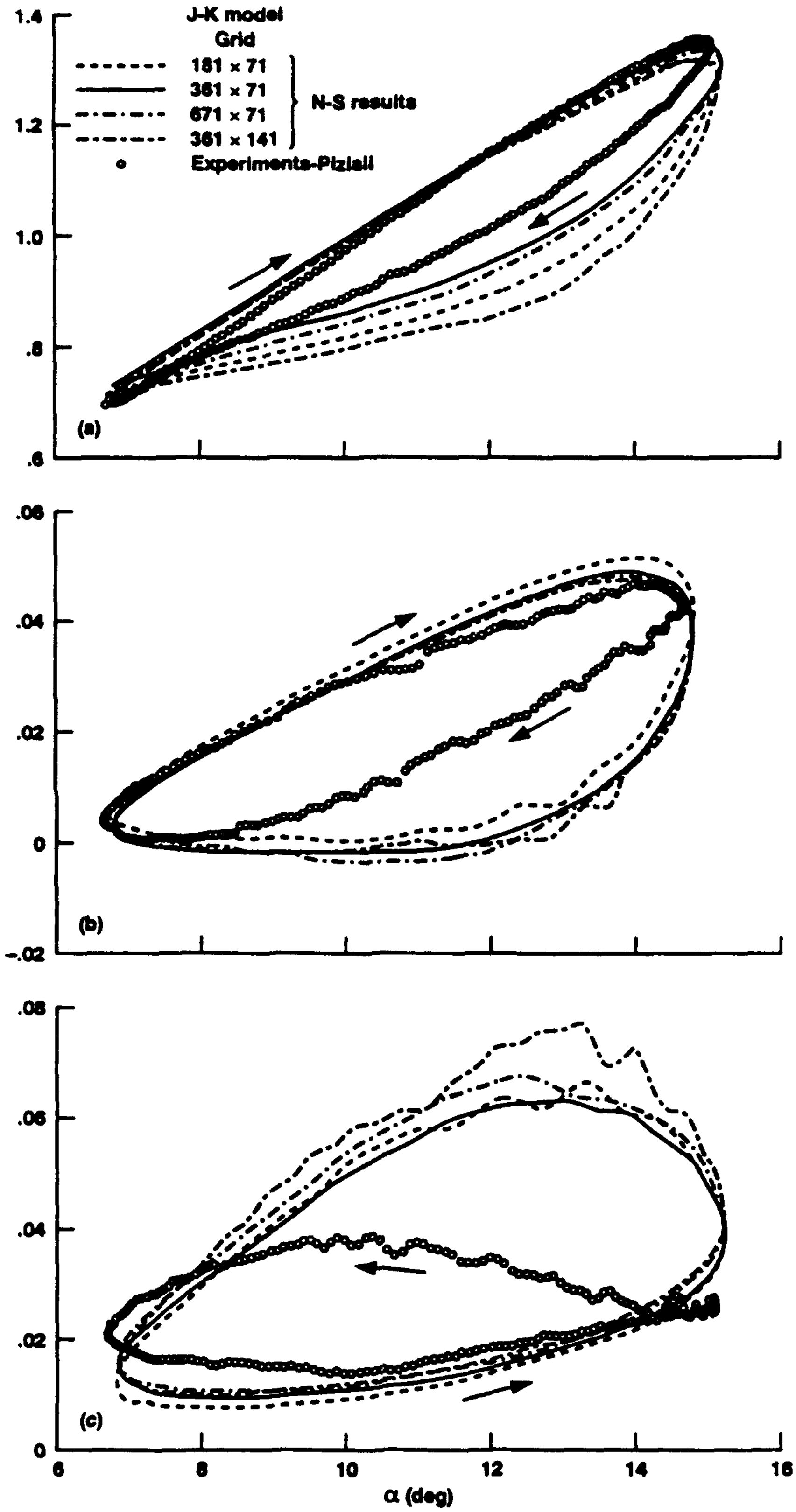

Fig. 42 Effect of grid sensitivity on the solution accuracy with J-K model for the experimental conditions of Fig. 40.

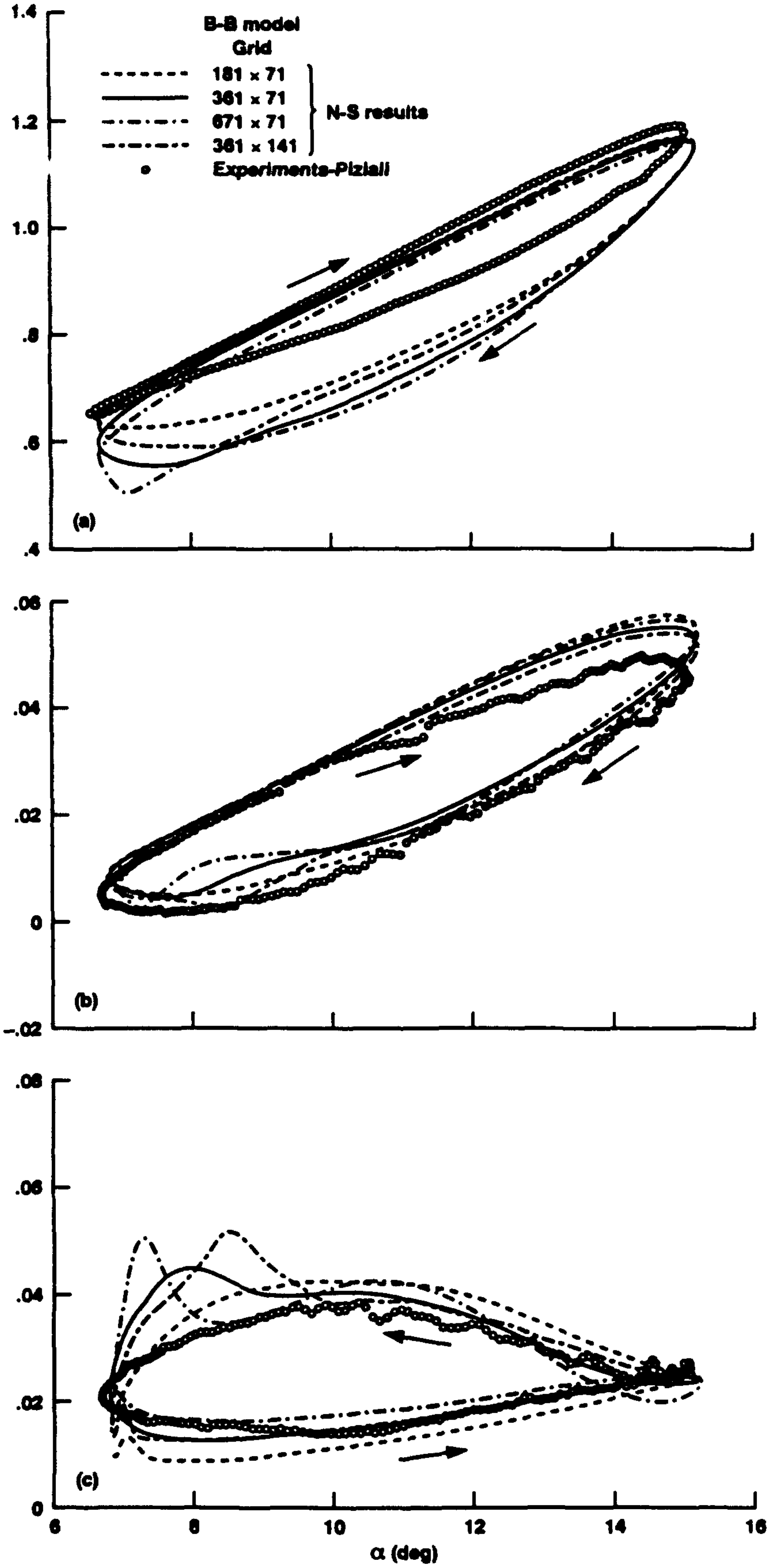

Fig. 43 Effect of grid sensitivity on the solution accuracy with B-B model for the experimental conditions of Fig. 40.

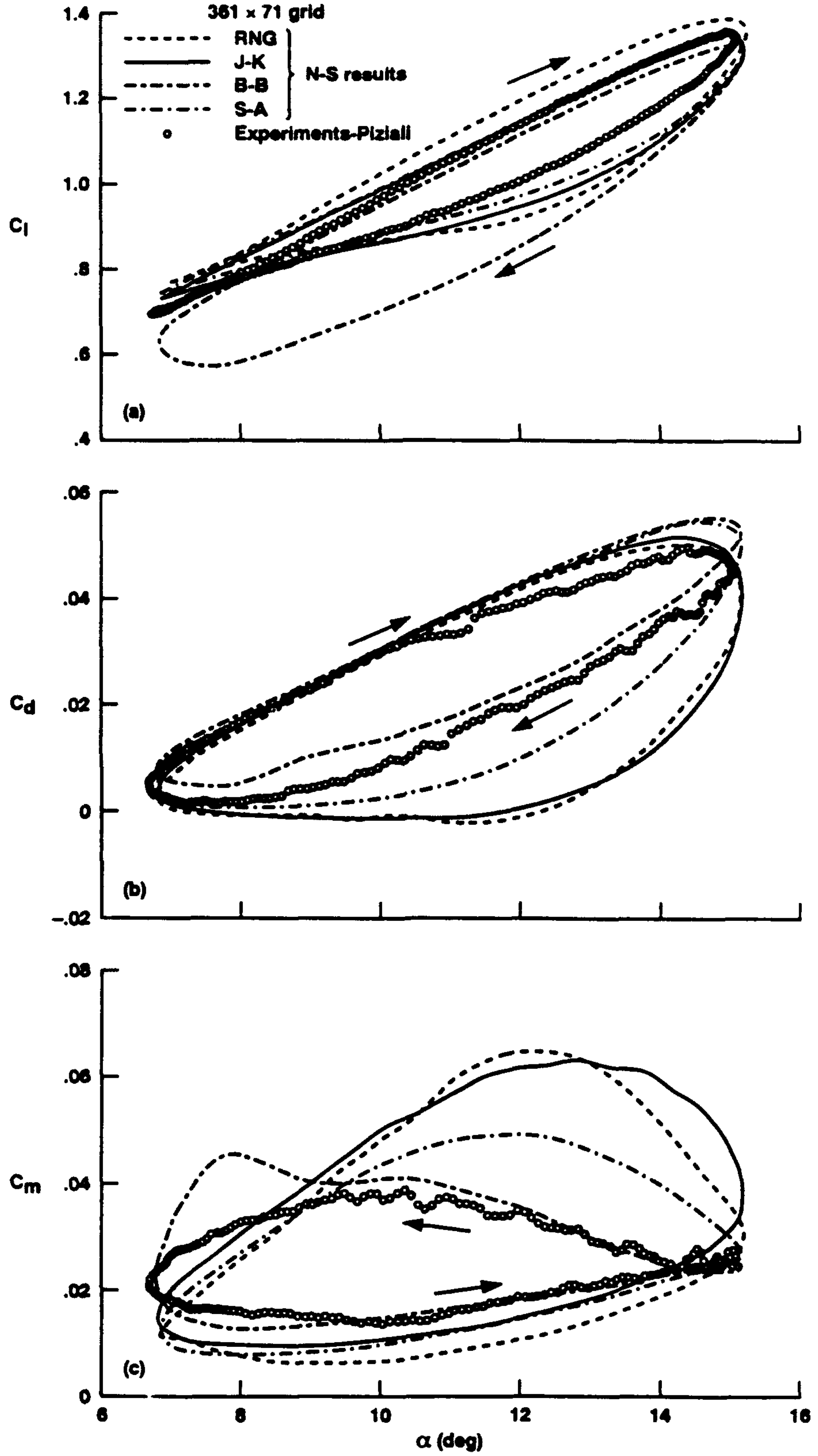

Fig. 44 Comparison of unsteady airloads hysteresis for different turbulence models with experiments for the flow conditions of Fig. 40.

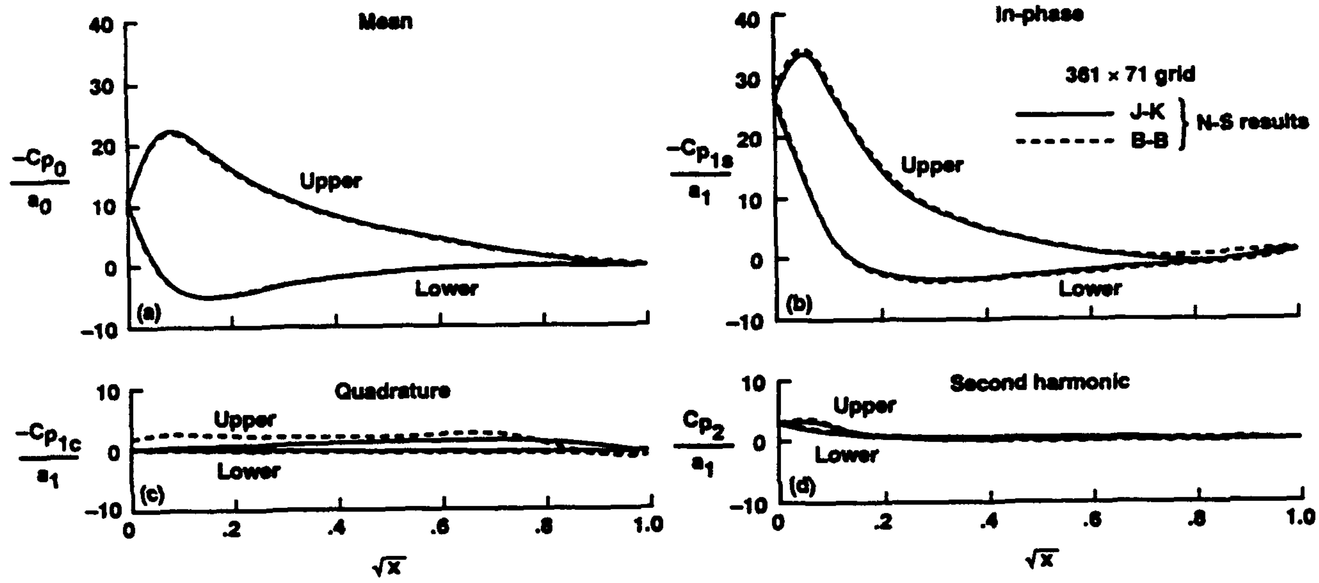

Fig. 45 Comparison of harmonic components of unsteady pressures for the J-K and B-B turbulence models at the flow conditions of Fig. 40.

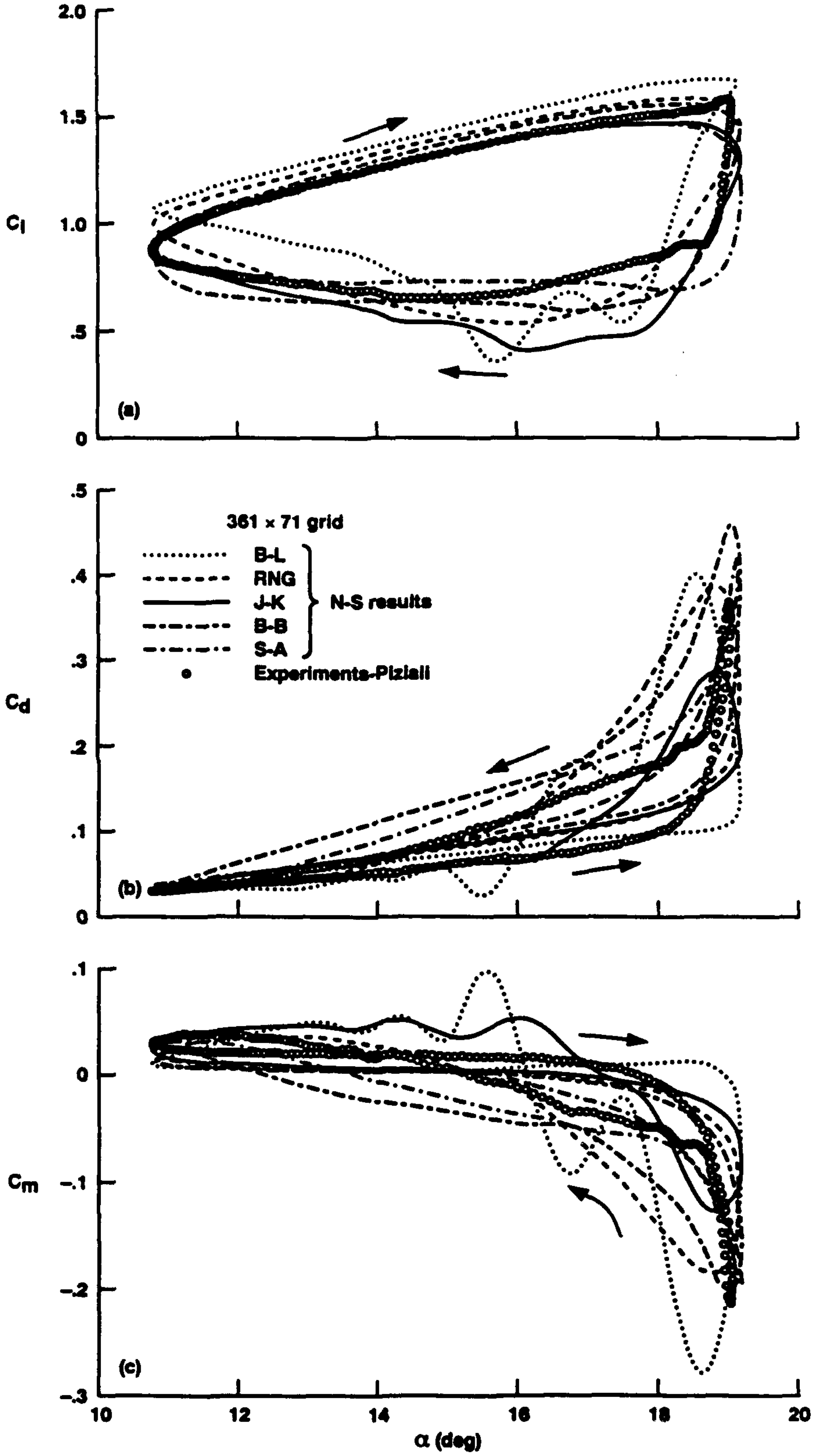

Fig. 46 Comparison unsteady airloads hysteresis for different turbulence models with experiments. $M_\infty = 0.29$, $k = 0.1$, $Re = 1.95\text{x}10^6$, and $\alpha(t) = 15° + 4.2° sin(Kt)$.

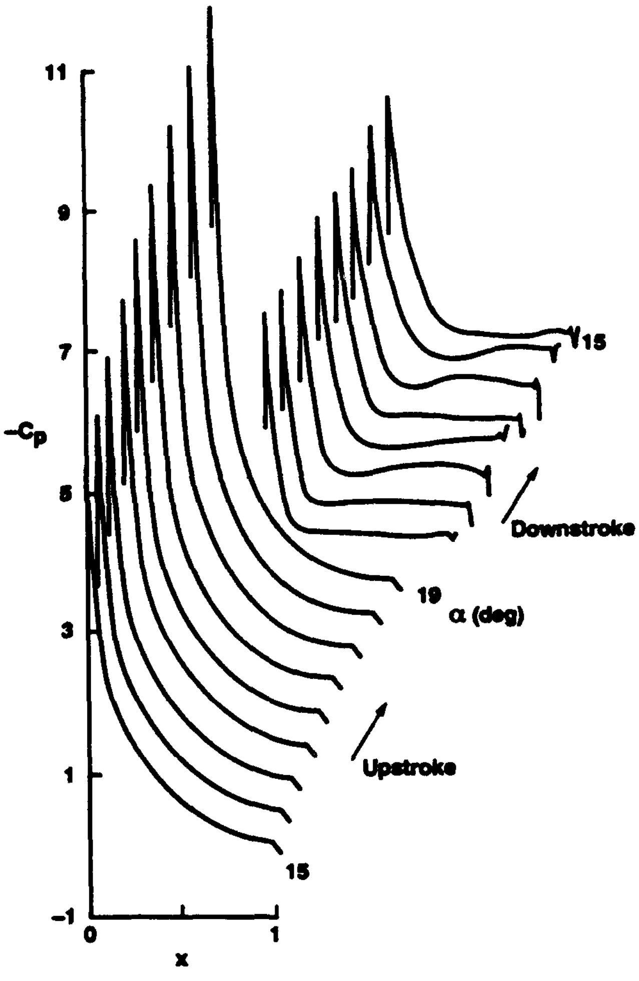

Fig. 47 Calculated unsteady surface pressures during an oscillatory cycle for the flow conditions of Fig. 46 using the B-B turbulence model.

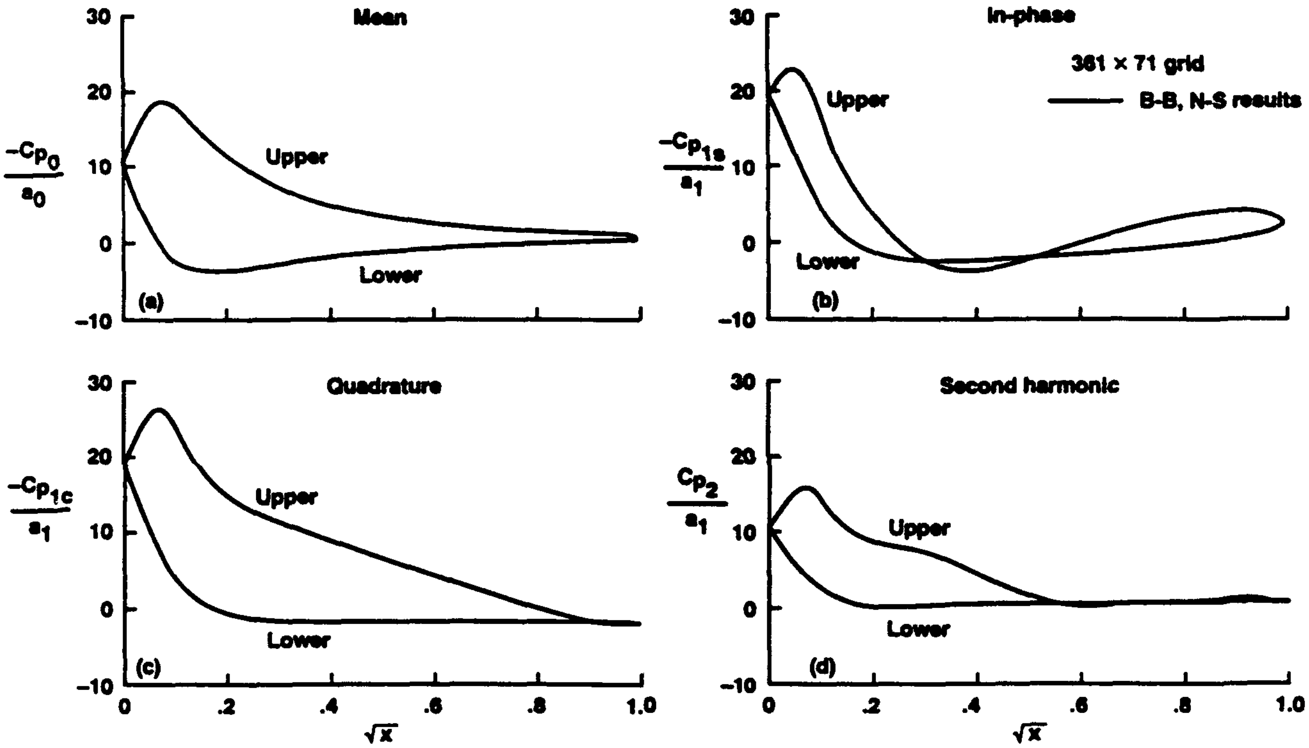

Fig. 48 Calculated harmonic components of unsteady pressures for the flow conditions of Fig. 46 using the B-B turbulence model.

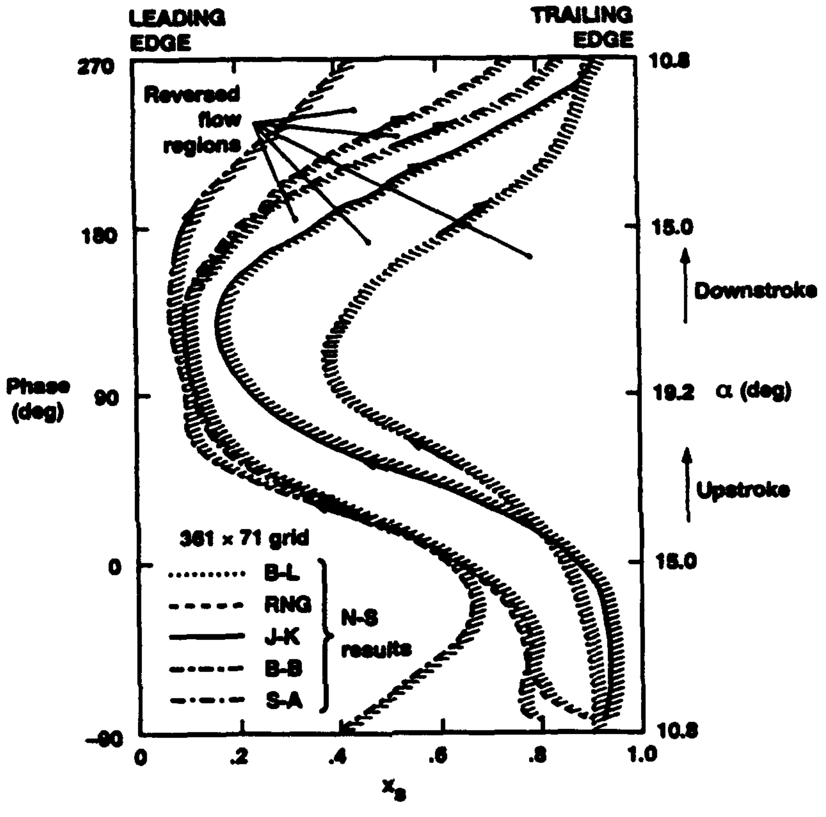

Fig. 49 Locus of flow reveral point during the oscillatory cycle for different turbulence models for the flow conditions of Fig. 46.

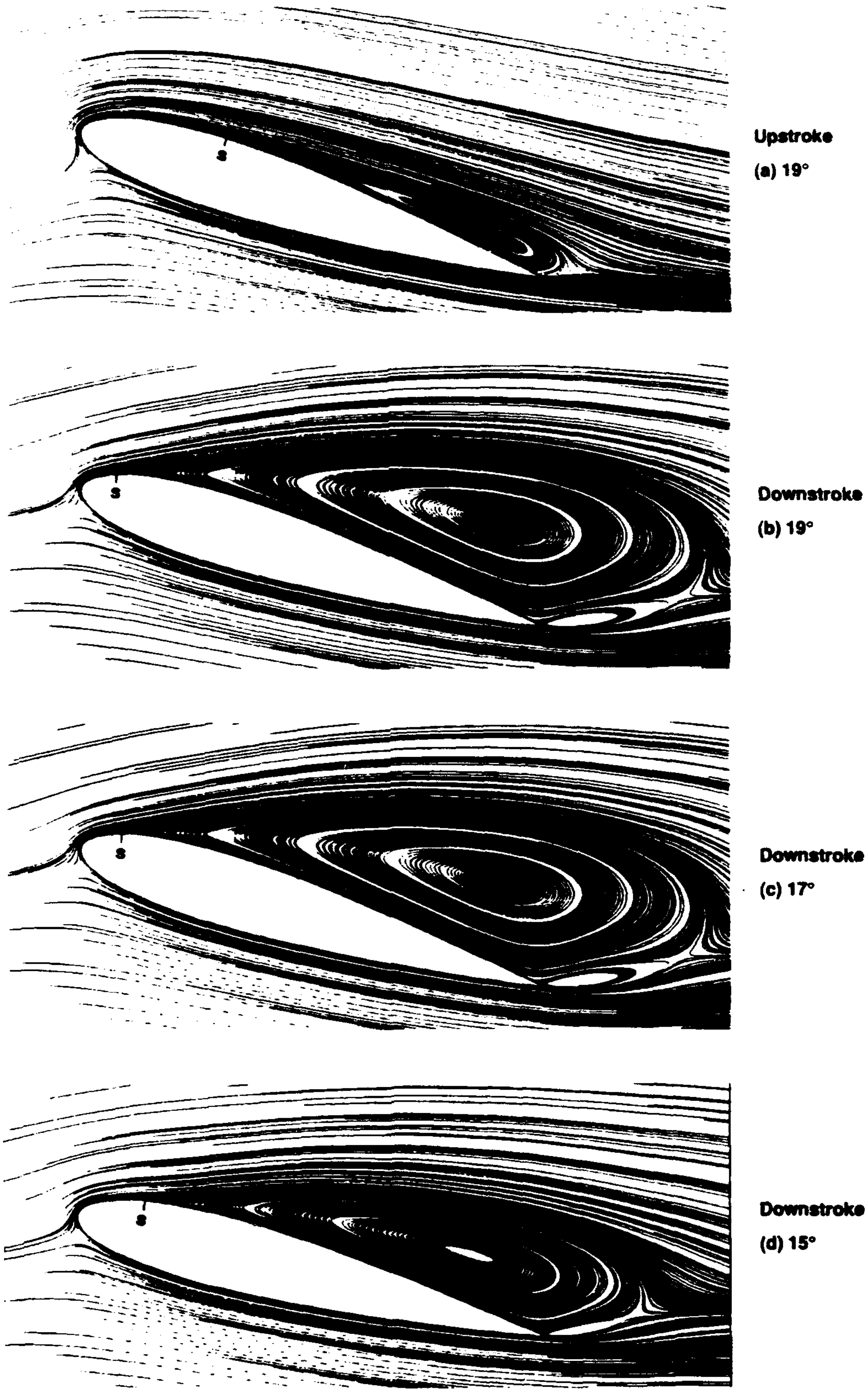

Upstroke
(a) 19°

Downstroke
(b) 19°

Downstroke
(c) 17°

Downstroke
(d) 15°

Fig. 50 Instantaneous steamline patterns at four different time instants during the oscillatory cycle for the B-B turbulence model and for the flow conditions of Fig. 46.

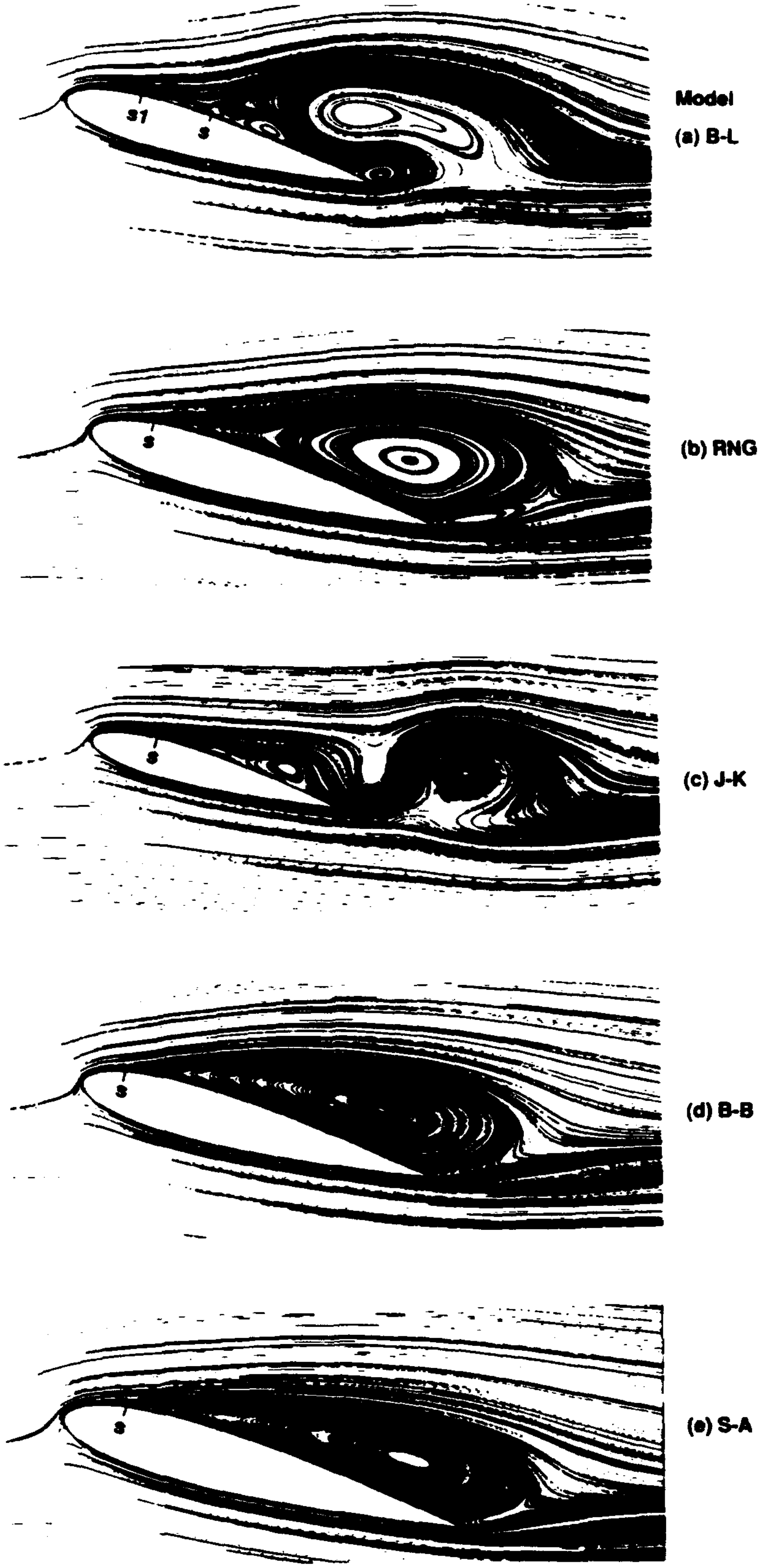
Model
(a) B-L
S1
S
(b) RNG
S
(c) J-K
S
(d) B-B
S
(e) S-A
S

Fig. 51 Comparison of instantaneous streamline patterns for different turbulence models at 16° downstroke during the oscillatory cycle for the flow conditions of Fig. 46.

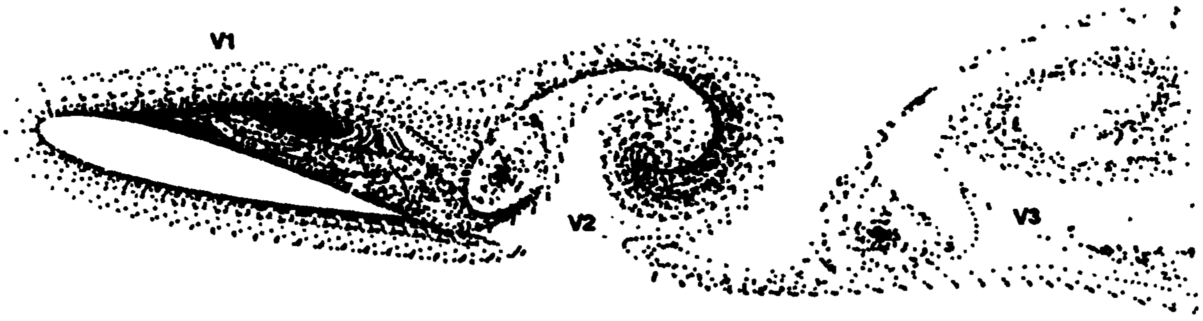

Fig. 52 Instantaneous streakline pattern for flow at 16° downstroke using the Baldwin-Barth model and for the flow conditions of Fig. 51.

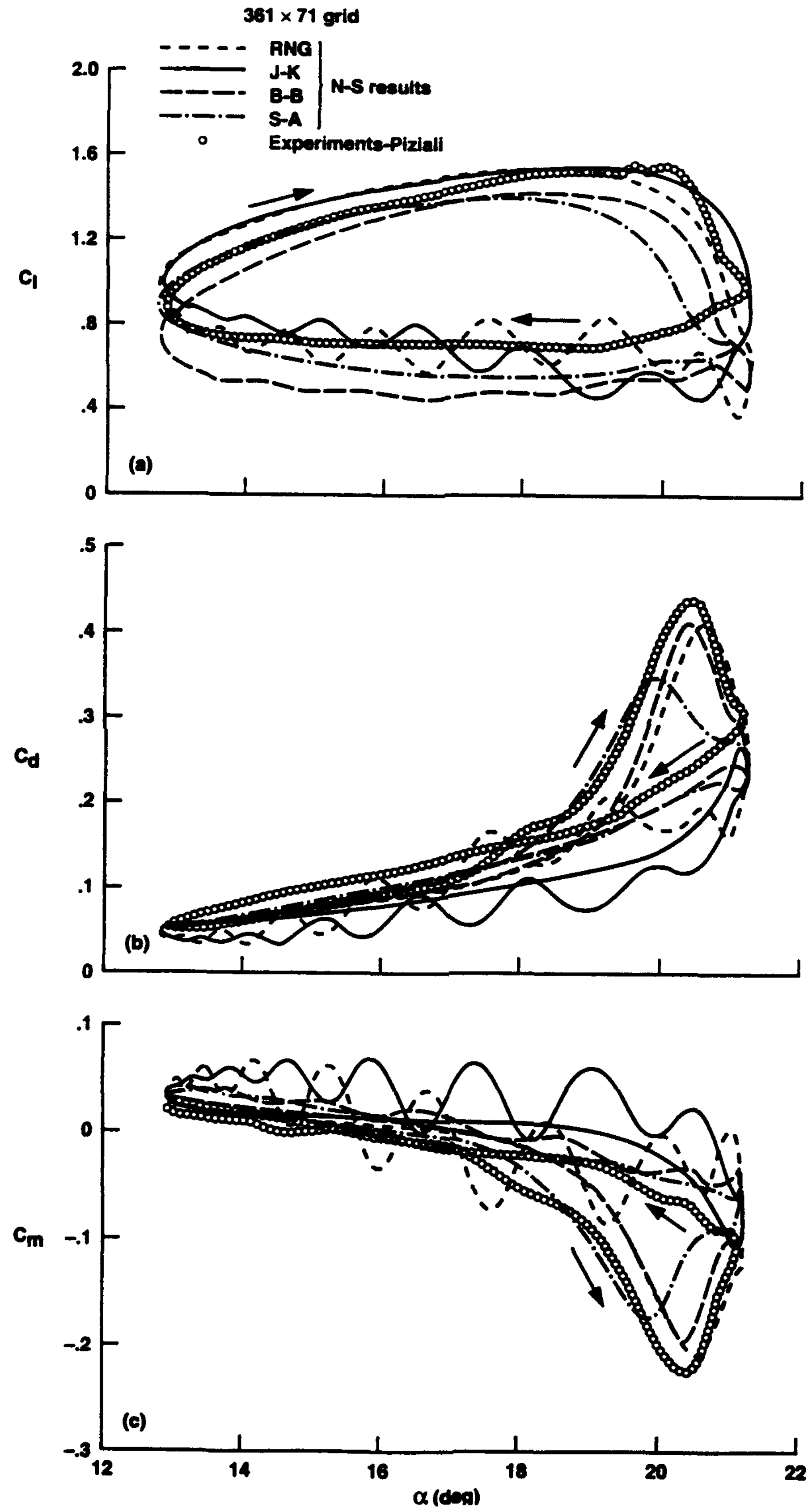

Fig. 53 Comparison of unsteady airloads hysteresis for different turbulence models with experiments. $M_\infty = 0.29$, $k = 0.1$, $Re = 1.95\text{x}10^6$, and $\alpha(t) = 17° + 4.2° sin(Kt)$.

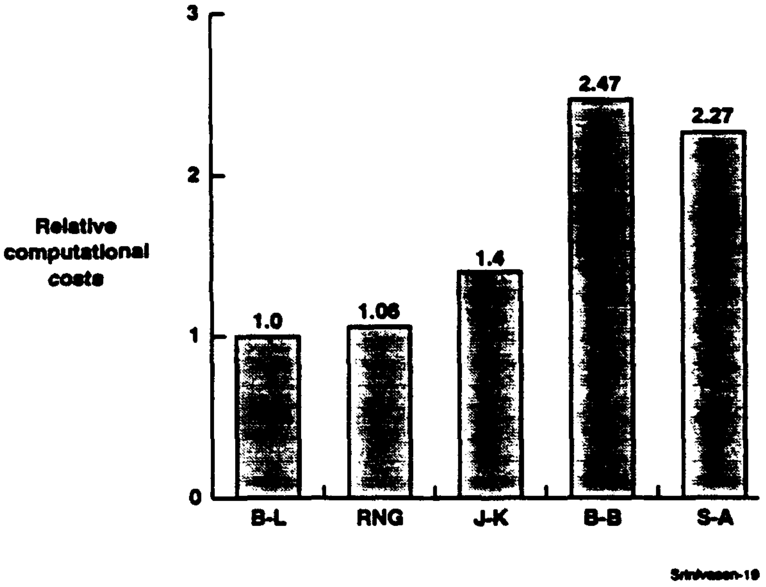

Fig. 54 Comparison of relative costs of computations with different turbulence models.

13. APPENDIX I

List of Technical Papers Published

1. G. R. Srinivasan, V. Raghavan, E. P. N. Duque, and W. J. McCroskey, "Flowfield Analysis of Modern Helicopter Rotors in Hover by Navier-Stokes Method," **Journal of the American Helicopter Society**, Vol. 38, No.3, July 1993, pp. 3-13.

2. G. R. Srinivasan and W. J. McCroskey, "Euler Calculations of Unsteady Interaction of Advancing Rotor with a Line Vortex," **AIAA Journal**, Vol. 31, No. 9, September 1993, pp. 1659-1666.

3. G. R. Srinivasan, J. A. Ekaterinaris, and W. J. McCroskey, "Dynamic Stall of an Oscillating Wing: Part-1: Evaluation of Turbulence Models," AIAA Paper 93-3403, AIAA 11th Applied Aerodynamics Conference, Aug. 1993, Monterey, California.

4. G. R. Srinivasan and J. D. Baeder, "TURNS: A Free-Wake Euler/Navier-Stokes Numerical Method for Helicopter Rotors," **AIAA Journal**, Vol. 31, No. 5, May 1993, pp. 959-962.

5. G. R. Srinivasan, J. D. Baeder, S. Obayashi, and W. J. McCroskey, "Flowfield of a Lifting Rotor in Hover - A Navier-Stokes Simulation," **AIAA Journal**, Vol. 30, No. 10, October 1992, pp. 2371-2378.

6. G. R. Srinivasan and J. Ekaterinaris, "Dynamic Stall of Oscillating Wing - 2-D and 3-D Navier-Stokes Simulations," Paper presented at the *International Dynamic Stall Workshop*, NASA Ames Research Center, June 1992.

7. G. R. Srinivasan, V. Raghavan, and E. P. N. Duque, "Flowfield Analysis of Modern Helicopter Rotors in Hover by Navier-Stokes Method," *AHS-RAeS Proceedings of the International Technical Specialists Meeting on Rotorcraft Acoustics and Rotor Fluid Dynamics*, Philadelphia, Pennsylvania, October 1991.

8. G. R. Srinivasan and J. D. Baeder, "Recent Advances in Euler and Navier-Stokes Methods for Calculating Helicopter Rotor Aerodynamics and Acoustics," (Invited) *Proceedings of the Fourth International Symposium on Computational Fluid Dynamics*, University of California, Davis, California, September 1991, pp. 1095-1100.

9. G. R. Srinivasan, "Navier-Stokes Solutions of a Helicopter Rotor in Hover and Forward Flight," *Proceedings of the International Aerospace Congress 1991*, Melbourne, Australia, May 1991, pp. 601-609.

10. G. R. Srinivasan, J. D. Baeder, S. Obayashi, and W. J. McCroskey, "Flowfield of a Lifting Hovering Rotor - A Navier-Stokes Simulation," Paper No. I.3.5, *Proceedings of the*

Sixteenth European Rotorcraft Forum, Glasgow, Scotland, September 1990; also NASA TM - 102862 and USAAVSCOM TR 90-A-006, August 1990.

TURNS Code Distribution List

1. Dr. W. J. McCroskey
2. Dr. Yung Yu
3. Dr. Chee Tung
4. Dr. Soogab Lee and Dr. Sungho Ko
5. Mr. E. P. N. Duque, U. S. Army Aeroflightdynamics Directorate, NASA Ames

6. Prof. J. D. Baeder, U. of Maryland
7. Dr. W. Warmbrodt and Ms. G. Yamauchi, NASA Ames Research Center
8. Mr. A. Egolf and Dr. B. Wake, UTRC/Sikorsky
9. Prof. J. Steinhoff, U. Tennessee and Flow Analysis, Inc.
10. Mr. J. Bridgeman, Flow Analysis, Inc.
11. Prof. G. Rajagopalan, Iowa State University
12. Dr. C. Burley, NASA Langley Research Center
13. Prof. A. Chattopadyay, Arizona State University
14. Dr. A. Hassan, McDonnel Douglas Helicopter Company

Some Recent Publications

Euler Calculations of Unsteady Interaction of Advancing Rotor with a Line Vortex

G. R. Srinivasan and W. J. McCroskey

Reprinted from

AIAA Journal

Volume 31, Number 9, September 1993, Pages 1659–1666

A publication of the
American Institute of Aeronautics and Astronautics, Inc.
The Aerospace Center, 370 L'Enfant Promenade, SW
Washington, DC 20024-2518

AIAA JOURNAL
Vol. 31, No. 9, September 1993

Euler Calculations of Unsteady Interaction of Advancing Rotor with a Line Vortex

G. R. Srinivasan* and W. J. McCroskey†
NASA Ames Research Center, Moffett Field, California 94035

The unsteady, three-dimensional flowfield of a helicopter rotor blade in forward flight encountering a concentrated line vortex is calculated using an implicit, finite difference numerical procedure for the solution of Euler equations. A prescribed vortex method is adopted to preserve the structure of the interacting vortex. The test cases considered for computation correspond to the two-bladed model rotor experimental conditions of Caradonna et al. and consist of parallel and oblique interactions. Comparison of numerical results with the test data show good agreement for the surface pressures for both parallel and oblique interactions at subsonic and transonic flow conditions. The results indicate that the subsonic parallel blade-vortex interaction is nearly two-dimensional-like and the unsteady time-lag effects appear to be negligible. However, both the three-dimensional and unsteady time-lag effects are found to be important under supercritical flow conditions and these effects are accentuated in the presence of transonic shocks. In contrast, the oblique blade-vortex interaction is unsteady and three dimensional at both the subsonic and transonic flow conditions.

Nomenclature

a = speed of sound
a_o = vortex core radius, see Eq. (8)
C = characteristic length scale, chord of the rotor blade
C_k = constant, see Eq. (8)
C_p = pressure coefficient based on local dynamic pressure
C_w = chord of the vortex generating wing
e = total energy per unit volume
$\hat{F}, \hat{G}, \hat{H}$ = flux vectors
J = Jacobian of the coordinate transformation
M_∞ = freestream Mach number, forward speed of the rotor
M_{tip} = tip Mach number of the rotor blade
p = static pressure
$\hat{Q}$ = vector of conserved flow variables
R = rotor radius
r = radial distance from the vortex center
r_B = rotor reference station normalized by R
$\mathcal{R}(t)$ = rotational matrix, see Eq. (4)
U, V, W = contravariant velocity components
u_∞ = forward flight speed
u, v, w = velocity components in physical space
v_θ = tangential velocity of the vortex
x, y, z, t = inertial coordinates
x_o, z_o = vortex offset position relative to the rotor axis
$\tilde{x}_v, \tilde{z}_v$ = distance from blade leading edge to the line vortex
$\tilde{x}, \tilde{y}, \tilde{z}, \tilde{t}$ = blade-fixed coordinates
γ = ratio of specific heats
Γ = vortex strength
$\hat{\Gamma}$ = dimensionless strength of the vortex, $\Gamma/(a_\infty C)$
μ = advance ratio, $u_\infty/\Omega R$
ξ, η, ζ, τ = generalized curvilinear coordinates
ρ = density
Ψ = azimuthal angle
Ω = angular velocity of the rotor

Subscripts

∞ = freestream
o = interacting vortex flowfield

Introduction

THE accurate simulation of the flowfield of a helicopter rotor is still one of the most complex and challenging problems of applied aerodynamics. This is true in spite of the availability of the present-day supercomputers of Cray-2 class and improved numerical algorithms. The major reason for this is that the flowfield of a rotor in forward flight is very complex. It is highly three dimensional, unsteady, and viscous, with pockets of transonic flow near the blade tips on the advancing blades and regions of dynamic stall on the retreating blades. In addition, the blades also shed complex vortical wakes. The concentrated tip vortices shed by these blades generally have a close encounter with the following blades. Such a close encounter of the force-free concentrated vortices with the rotor blades is often the cause of unsteady load fluctuations and impulsive noise. These and other complex problems associated with such a flowfield are delineated in a schematic of a helicopter in forward flight in Fig. 1.

The spiralling vortex sheet emanating from each of the blades of the rotor has a profound influence on the performance of the helicopter. It not only alters the effective pitch angle of the blades and thus the airloads, but also produces highly nonlinear interactions of the vortex with the rotor flowfield. It is possible that such interactions might produce

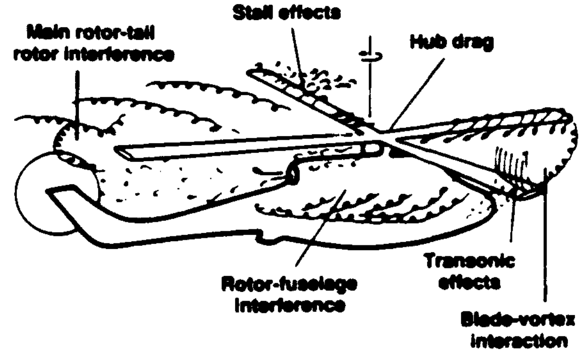

Fig. 1 Schematic of the complex flowfield of a helicopter in forward flight.

Presented as Paper 89-1848 at the AIAA 20th Fluid Dynamics, Plasma Dynamics, and Lasers Conference, Buffalo, NY, June 12-14, 1989; received July 10, 1989; revision received Dec. 31, 1992; accepted for publication Feb. 2, 1993. This paper is declared a work of the U.S. Government and is not subject to copyright protection in the United States.

*Senior Staff Scientist, JAI Associates, Inc., P.O. Box 293, Mountain View, CA. Associate Fellow AIAA.

†Senior Research Scientist, U. S. Army Aeroflightdynamics Directorate—ATCOM. Fellow AIAA.

vortex-induced boundary-layer separation which results in a sudden loss of lift and increase in drag. An accurate simulation of the rotor flowfield, therefore, must consider the induced effects of the vortex wake including the blade-vortex interactions (BVI).

Numerical simulations of vortex wakes are being attempted only recently as bigger and faster computers have become available.[1] This and other investigations have had some limited success to date. On the other hand, carefully measured experimental data on the three-dimensional BVI have been made available recently.[2,3] But much of the progress in modeling these blade-vortex interactions has been hampered by the lack of development of theoretical and/or numerical techniques to preserve the structure of the concentrated vortices in the flowfield without significant diffusion. The study of blade-vortex interaction has been the subject of numerous recent research papers.[4-15] These studies have considered different methods of preserving the structure of the concentrated vortex while convecting in the flowfield. Among these, the vortex-fitting (also called the prescribed-vortex or perturbation method or split-potential formulation) technique has been demonstrated to be a very effective method in preserving the vortex even when the computational grid is sparse. The major drawback of this method is that it does not allow for the distortion of the vortex core. For interactions where the vortex does not impinge head-on onto the blade, this method has proven to have worked very effectively and economically[7,8] compared to a more exact formulation[5] that allows for vortex distortion.

The purpose of this study is to devise a numerical method for the solution of the Euler equations to calculate accurately the unsteady blade-vortex interactional flowfield. In particular, this paper will focus on demonstrating the ability to calculate an interaction flowfield, which is three dimensional and unsteady, for parallel and oblique blade-vortex interactions on a model helicopter rotor tested in a wind tunnel[2,3] at subsonic and transonic flow conditions.

Governing Equations and Numerical Scheme

The governing partial differential equations are the unsteady Euler equations. For generality, the equations are transformed from the inertial Cartesian reference frame (x, y, z, t) to the arbitrary curvilinear coordinate frame (ξ, η, ζ, τ) that moves with the blade, while retaining strong conservation law form to capture shock waves. The transformed equations can be written as[16]

$$\partial_\tau(\hat{Q}-\hat{Q}_o)+\partial_\xi(\hat{F}-\hat{F}_o)+\partial_\eta(\hat{G}-\hat{G}_o)+\partial_\zeta(\hat{H}-\hat{H}_o)=0 \quad (1)$$

where

$$\hat{Q}=\frac{1}{J}\begin{bmatrix}\rho\\ \rho u\\ \rho v\\ \rho w\\ e\end{bmatrix}, \qquad \hat{F}=\frac{1}{J}\begin{bmatrix}\rho U\\ \rho uU+\xi_x p\\ \rho vU+\xi_y p\\ \rho wU+\xi_z p\\ UH-\xi_t p\end{bmatrix}$$

$$\hat{G}=\frac{1}{J}\begin{bmatrix}\rho V\\ \rho uV+\eta_x p\\ \rho vV+\eta_y p\\ \rho wV+\eta_z p\\ VH+\eta_t p\end{bmatrix}, \qquad \hat{H}=\frac{1}{J}\begin{bmatrix}\rho W\\ \rho uW+\zeta_x p\\ \rho vW+\zeta_y p\\ \rho wW+\zeta_z p\\ WH-\zeta_t p\end{bmatrix} \quad (2)$$

Here $\hat{Q}$ is the vector of the conserved flow variables, namely, the density ρ, the three mass fluxes ρu, ρv, and ρw in the three coordinate directions, and the total energy per unit volume e. Similarly, $\hat{Q}_o$ is a vector of the conserved flow variables corresponding to the solution of the Euler equations for a prescribed line vortex aligned with the uniform freestream of Mach number M_∞ in the y direction and convecting with the flow as shown in Fig. 2. The vectors $\hat{F}$, $\hat{G}$, $\hat{H}$, and $\hat{F}_o$, $\hat{G}_o$, $\hat{H}_o$ represent the appropriate flux terms for the two flows, respectively. These flux vectors, as shown, are scaled by the Jacobian J, e.g., $\hat{Q} = J^{-1}Q$, etc. The contravariant velocity components U, V, and W are defined as

$$U = \xi_t + \xi_x u + \xi_y v + \xi_z w$$

$$V = \eta_t + \eta_x u + \eta_y v + \eta_z w$$

$$W = \zeta_t + \zeta_x u + \zeta_y v + \zeta_z w$$

In the present formulation, ξ lies in the chordwise or wraparound direction, η is in the spanwise direction, and ζ is normal to the blade surface. The terms ξ_t, ξ_x, ξ_y, ξ_z, etc., are the coordinate transformation metrics.[16]

The velocity components u, v, w, and the pressure p are related to the total energy per unit volume e through the equation of state for a perfect gas by

$$p = (\gamma - 1)\,[e - (\rho/2)(u^2 + v^2 + w^2)] \quad (3)$$

This equation of state, together with Eq. (1), completes the necessary equations that give the entire flowfield description. These equations are nondimensional. The reference length and velocity scales used are the chord of the blade C and the freestream speed of sound a_∞, respectively. All length scales are normalized by C and time by C/a_∞. The primitive variables of Eq. (1), namely, the density ρ, the mass fluxes ρu, ρv, ρw, and the energy per unit volume e, are normalized by the freestream reference quantities made up of ρ_∞ and a_∞ and the pressure p by γp_∞.

In the present formulation, Eq. (1) is solved in the inertial reference frame with the boundary conditions applied on the rotating blade. The terms u, v, and w are the Cartesian com-

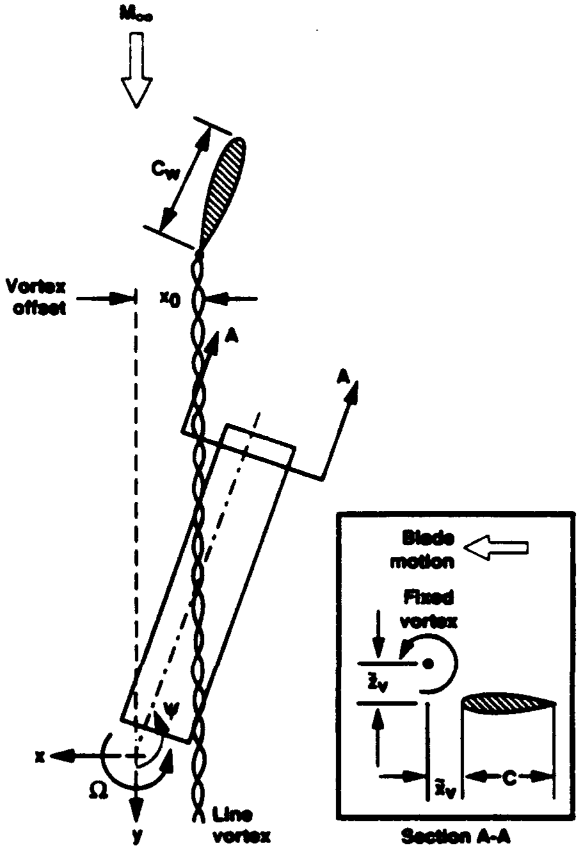

Fig. 2 Schematic of an advancing rotor blade passing a line vortex in a wind-tunnel experiment (Ref. 3).

ponents of velocity in the inertial coordinate system (x, y, z, t). The inertial coordinates $X = (x, y, z, t)$ are related to the blade-fixed coordinates $X_b = (\tilde{x}, \tilde{y}, \tilde{z})$ through the relation given by[17]

$$X(x, y, z) = \mathcal{R}(t) X_b(\tilde{x}, \tilde{y}, \tilde{z}), \qquad t = \tilde{t} \tag{4}$$

where $\mathcal{R}(t)$ is the rotational matrix.[18] For a rigid rotor that neglects the rotor disk attitude, blade flapping, and pitching motions, the rotational matrix can be written as

$$\mathcal{R}(t) = \frac{1}{J}\begin{bmatrix} \cos\Omega\tilde{t} & -\sin\Omega\tilde{t} & 0 \\ \sin\Omega\tilde{t} & \cos\Omega\tilde{t} & 0 \\ 0 & 0 & 1 \end{bmatrix} \tag{5}$$

Here Ω is the angular velocity of the rotor and Ωt represents the azimuthal sweep of the rotor blade.

The governing equations are solved using a two-factor, implicit, finite difference numerical scheme. The numerical algorithm that was originally developed by Ying et al.[19] has been modified to accommodate a prescribed-vortex perturbation formulation for a rotating blade environment. The numerical scheme uses spatial central differencing in the η and ζ directions and upwind differencing in the ξ direction. The two-factored scheme containing the vortex-fitting terms is given by

$$\begin{aligned}
&[I + h\delta_\xi^b(\hat{A}^+)^n + h\delta_\zeta\hat{C}^n - D_i|_\zeta] \\
&\quad\times [I + h\delta_\xi^f(\hat{A}^-)^n + h\delta_\eta\hat{B}^n - D_i|_\eta](\Delta\hat{Q}^n - \Delta\hat{Q}_o^n) \\
&\quad= -\Delta t\{\delta_\xi^b[(\hat{F}^+)^n - (\hat{F}_o^+)^n] + \delta_\xi^f[(\hat{F}^-)^n - (\hat{F}_o^-)^n] \\
&\quad+ \delta_\eta(\hat{G}^n - \hat{G}_o^n) + \delta_\zeta(\hat{H}^n - \hat{H}_o^n)\} \\
&\quad- (D_e|_\eta + D_e|_\zeta)(\hat{Q}^n - \hat{Q}_o^n)
\end{aligned} \tag{6}$$

where $h = \Delta t$ for first-order time accuracy; δ is typically a three-point, second-order-accurate, central difference operator; and the operators δ_ξ^b and δ_ξ^f are backward and forward three-point difference operators. The time index is denoted by n such that $t = (n\Delta t)$, and $\Delta\hat{Q}^n = \hat{Q}^{n+1} - \hat{Q}^n$. The flux vector $\hat{F}$ has been split into $\hat{F}^+$ and $\hat{F}^-$, according to its eigenvalues,[20] and the Jacobian matrices $\hat{A}^\pm$, $\hat{B}$, and $\hat{C}$ result from the local linearization of fluxes about the previous time level.[16] In writing Eq. (6), it is assumed that $\hat{A}_o^\pm \approx \hat{A}^\pm$, $\hat{B}_o \approx \hat{B}$, and $\hat{C}_o \approx \hat{C}$ where the Jacobian matrices $\hat{A}_o^\pm$, $\hat{B}_o$, and $\hat{C}_o$ correspond to the prescribed-vortex flowfield. In the absence of vortex interaction, the prescribed-disturbance flowfield reduces to a freestream. The finite difference scheme described in Eq. (6) uses flux splitting in ξ direction and central differencing in the η and ζ directions. As a consequence, numerical dissipation terms D_i and D_e are used in the η and ζ directions, and are given as combinations of second and fourth differences. For example, these terms in η direction are given by

$$\begin{aligned}
D_e|_\eta &= (\Delta t)J^{-1}(|\eta|_x + |\eta|_t + |\eta|_z) \\
&\quad\times\left[\epsilon_2\bar{\delta}\,\frac{|\bar{\delta}^2 p|}{|(1+\bar{\delta}^2)p|}\,\bar{\delta} + \epsilon_4\bar{\delta}^4\right]\Bigg|_\eta J
\end{aligned} \tag{7a}$$

$$\begin{aligned}
D_i|_\eta &= (\Delta t)J^{-1}(|\eta|_x + |\eta|_y + |\eta|_z) \\
&\quad\times\left[\epsilon_2\bar{\delta}\,\frac{|\bar{\delta}^2 p|}{|(1+\bar{\delta}^2)p|}\,\bar{\delta} + 3\epsilon_4\bar{\delta}^4\right]\Bigg|_\eta J
\end{aligned} \tag{7b}$$

where ϵ_2 and ϵ_4 are constants and $\bar{\delta}$ is a midpoint operator. In the vicinity of shock waves, the fourth-difference terms can cause oscillations, so it is desirable to drop these terms and rely only on the second-difference terms.

The factored operators are solved by sweeping in the ξ direction and inverting tridiagonal matrices with 5×5 blocks for the other two directions. Currently, a significant part of the computational time is taken to form the plus and minus Jacobian matrices for the flux vector $\hat{F}$ with this numerical scheme. However, this effort has been reduced by computing $\hat{A}^+$ and $\hat{A}^-$ at every other point (in both η and ζ directions) and averaging to obtain the matrices at the intermediate points. The numerical algorithm is second-order accurate in space and first order in time and the code is vectorized for the Cray-2 supercomputer.

A body-conforming finite difference grid has been used for the rectangular blade having an aspect ratio of 7 and consists of a warped spherical O–O grid topology. The flowfield grid is generated using the three-dimensional hyperbolic grid solver of Steger and Chaussee[21] with proper clustering in the leading- and trailing-edge regions and in the tip region. The grid is nearly orthogonal at the surface, the spacing in the normal direction at the surface is chosen to be $0.02C$, and all of the calculations were done on a $21 \times 101 \times 15$ points grid. The grid boundary is located at 8 chords in all directions.

The boundary conditions, both surface and far field, are applied explicitly. The slip conditions use an extrapolation of contravariant velocities to the surface. The density at the wall is determined by the zeroth-order extrapolation. The pressure along the body surface is calculated from the normal momentum relation (see, e.g., Ref. 16). Having calculated the density and pressure, the total energy is determined from the equation of state.

At the far-field boundary, the flow quantities are either fixed or extrapolated from the interior depending on whether the flow is subsonic or supersonic and if it is of inflow- or outflow-type at the boundary.[22,23] The characteristic velocities of the Euler equations determine the number of flow properties to be specified to control the reflections of waves from the boundaries. For the subsonic-inflow boundary, four quantities are specified and one quantity is determined. The four specified here are a Riemann invariant, the entropy, and two tangential velocities; the quantity that is calculated is also a Riemann invariant. For the supersonic inflow, all flow quantities are specified. At the subsonic-outflow boundaries, only one quantity is specified. For the supersonic-outflow condition all flow quantities are extrapolated from the interior. The plane containing the blade root is chosen very close to the rotation axis of the blade (at $R = 1.0C$) and is also treated as a far-field boundary.

The concentrated line vortex generated upstream of the rotor by a rectangular wing is fixed in the inertial space along a line of constant x. It is assumed to have an analytical representation for the cylindrical velocity distribution given by

$$v_\theta = \frac{C_k\Gamma}{2\pi r}\left(\frac{r^2}{r^2 + a_o^2}\right) \tag{8}$$

The constant C_k in the preceding expression has been determined to be equal to 0.8 by matching the peak tangential velocity with the experimentally measured value at the measured radial distance.[8] The constant a_o is approximately equal to the radius of the viscous core of the vortex, and this is equal to the experimentally measured value of $0.167C$. The induced velocity field due to this line vortex is calculated using the Biot-Savart law and the pressure field is calculated by solving the radial momentum equation.

Results and Discussion

All of the calculations performed in this study are done in a time-accurate manner. Three test cases have been chosen for calculations from among the many test conditions of the two sets of experiments of Caradonna et al.[2,3] for parallel and oblique blade-vortex interactions. Since one of the purposes of the experiments was to collect data to validate numerical methods, the experimental apparatus was kept simple to ease the representation by numerical methods. The rotor geometry consists of a two-bladed rigid rotor of approximately 14-chord diameter. The blades have a rectangular planform and are made up of NACA 0012 airfoils with no twist or taper. The rotor blades are set at zero collective pitch and are, therefore, essentially nonlifting in the absence of the vortex interaction. The interacting vortex was generated upstream of this rotor by a lifting NACA 0015 rectangular wing. Parallel blade-vortex interaction flowfields were generated by positioning the line vortex along the y axis ($x_o = 0.0$). Similarly, the oblique BVI flowfields were generated by moving the position of the line vortex such that it is still aligned along the y axis with $x_o < 0.0$. This enables the advancing rotor blade to encounter the line vortex continuously in the first and second quadrants of the azimuthal travel as shown in Fig. 2.

Although the main focus of the present investigation is to calculate the parallel and oblique blade-vortex interactions, it is necessary to first calculate the baseline flowfields of rotor-alone configuration (in the absence of vortex interaction) at the same freestream conditions. Two sets of results for parallel blade-vortex interactions, corresponding to $M_{\text{tip}} = 0.6$ and 0.8 and $\mu = 0.2$, and one set of results for oblique blade-vortex interaction corresponding to $M_{\text{tip}} = 0.763$ and $\mu = 0.197$, will be presented in the following sections and compared with the experimental data.

Rotor-Alone Case

The calculation of the rotor-alone flowfield solutions serves two purposes. First, it enables an understanding of the importance of unsteady time-lag effects in shock-wave growth and decay as well as the three dimensionality of the flowfield of the advancing rotor under transonic flow conditions. Second, it provides the baseline solution for starting the unsteady calculations of the vortex-interaction flowfield.

Figure 3 shows the instantaneous surface pressure distributions for various azimuthal positions of advancing rotor for the flow condition of $M_{\text{tip}} = 0.6$ and $\mu = 0.2$. Examination of these results suggests that at this reference station of $r_B = 0.893$ and for the subcritical flow condition, the flow behaves as if it is quasisteady and quasi-two dimensional. In spite of the gradual increase of the blade-element relative speed in the first quadrant and gradual decrease of the same in the second quadrant, the flowfield appears to remain nearly the same at all azimuthal locations, indicating that the unsteady time-lag effects are virtually absent for this flow condition and that the flow behaves as if it is quasisteady. In fact, also shown in Fig. 3 is the quasisteady surface pressures for one azimuth location of $\Psi = 90$ deg, which is in perfect agreement with the unsteady surface pressures at different azimuthal positions. Also, the comparison of these three-dimensional results with the two-dimensional results of Ref. 8 further confirms that the two results are nearly identical, suggesting that the flow also behaves as if it is quasi-two dimensional.

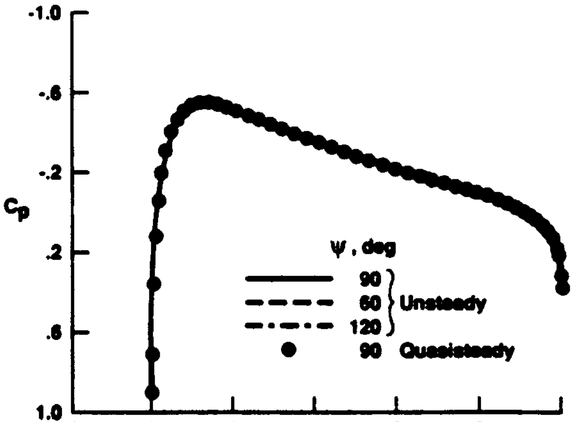

Fig. 3 Comparison of calculated surface pressures for an advancing rotor with the quasisteady surface pressures ($M_{\text{tip}} = 0.6$, $\mu = 0.2$, and $r_B = 0.893$).

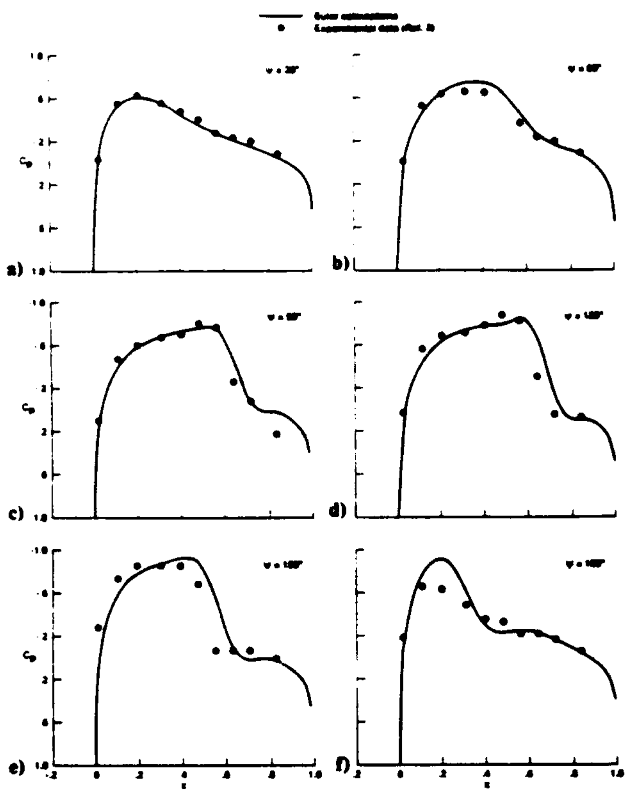

Fig. 4 Instantaneous surface pressure distributions at the reference blade section for advancing rotor ($M_{\text{tip}} = 0.8$, $\mu = 0.2$, and $r_B = 0.893$).

At the supercritical tip flow conditions, corresponding to $M_{\text{tip}} = 0.8$ and $\mu = 0.2$, the basic rotor flowfield is dominated by the presence of a strong shock wave on the advancing blade over large parts of the first and second quadrants. The instantaneous surface pressures for the advancing rotor are shown in Fig. 4 at the radial station $r_B = 0.893$ for different azimuthal positions of the rotor blade. The results show good agreement with the experiments for all azimuthal locations. The absence of viscosity and therefore the boundary layer causes the Euler results to overpredict the shock strength and position in the first and second quadrants of azimuthal travel. The experimental data shows that the strong shock wave which was present at the beginning of the second quadrant nearly decays by the time the blade reaches $\Psi = 180$-deg position. In contrast, the numerical method predicts that the shock wave continues to persist at least until after it passes the $\Psi = 180$-deg azimuthal location. In fact, it is completely absent by the time the rotor blade reaches $\Psi = 184$-deg position. Previous two-dimensional Navier-Stokes calculations of the same flow[8] had shown strong three dimensionality and unsteady time lags in shock-wave growth and decay. The two-dimensional assumption for this flow essentially overpredicted the shock-wave position and strength, unlike the subcritical flow condition. In contrast, the three-dimensional Euler results seem to follow the experimental observation correctly.

Thus at this transonic flow condition, the flowfield is highly three dimensional, and exhibits strong unsteady time-lag behavior in the shock-wave formation and eventual demise. The unsteady time-lag characteristic of the flowfield is demonstrated in the surface pressure distributions of Fig. 4 shown for $\Psi = 60$-deg and 120-deg azimuthal positions, which shows that the two results are very different from each other.

In principle, the shock wave should attain its maximum strength when the relative flow speed reaches a maximum

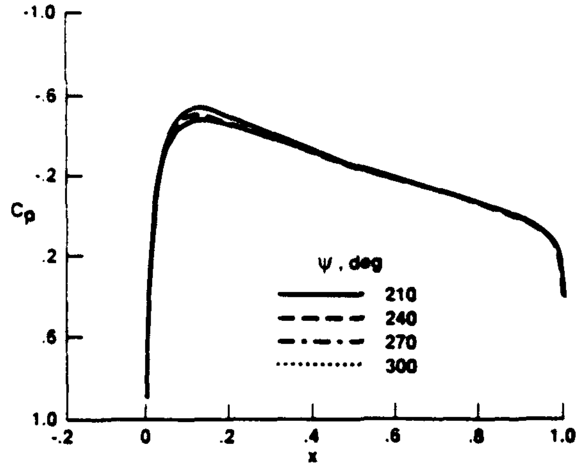

Fig. 5 Instantaneous surface pressure distributions at the reference blade section for retreating blade ($M_{tip} = 0.8$, $\mu = 0.2$, and $r_B = 0.893$).

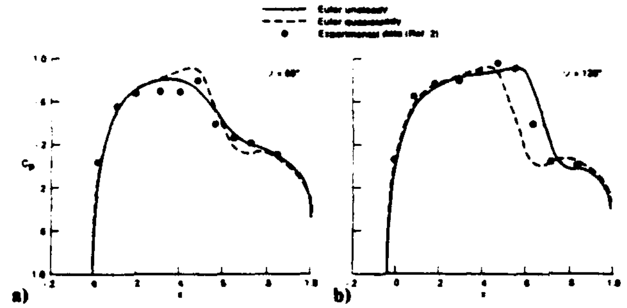

Fig. 6 Comparison of quasisteady and unsteady surface pressures for advancing rotor ($M_{tip} = 0.8$, $\mu = 0.2$, and $r_B = 0.893$).

value for Ψ = 90-deg blade azimuthal position. However, the shock wave keeps growing in strength even after the blade has passed the Ψ = 90-deg azimuthal position and a weak shock wave seems to persist even at the Ψ = 180-deg azimuth. The strengthening of the shock wave in the first quadrant and beyond, and the slow demise of it in the second quadrant, suggests the existence of a strong unsteady time-lag effect at this flow condition. Such a behavior was totally absent at the subcritical flow condition. The presence of the shock wave seems to introduce not only the time lag in the adjustment of the flow as the blade sweeps in azimuth, but also makes the flow highly three dimensional.

However, this behavior is confined to the advancing side of the rotor blade. In contrast, the flowfield of the retreating side appears really benign for this nonlifting rotor. The lingering effects of the shock wave, persisting at Ψ = 180 deg, soon die out as the blade sweeps into the third quadrant. Shown in Fig. 5 are the surface pressure distributions for several azimuthal locations of the blade in the third and fourth quadrants on the retreating cycle. Since the flowfield is basically subcritical on the retreating side, the instantaneous surface pressures of Fig. 5 appear to have the same behavior as those of Fig. 3.

The decay of the strong time-lag effects on the retreating blade allows a simplification in starting the unsteady calculations, but only if the strongest transonic region is avoided initially. To illustrate this point, Fig. 6 shows the quasisteady and unsteady surface pressures for the case of $M_{tip} = 0.8$ and $\mu = 0.2$ at the azimuthal locations of Ψ = 60 deg and 120 deg. For this flow condition, the results indicate that the quasisteady assumption overpredicts the shock strength at Ψ = 60 deg and underpredicts at Ψ = 120 deg. However, at Ψ = 0.0-deg position, the quasisteady and unsteady results are nearly identical, even for this flow condition. Therefore, it is still reasonable to start the unsteady calculations from the quasisteady solution calculated at Ψ = 0.0-deg azimuthal location.

Parallel Blade-Vortex Interaction

During the unsteady three-dimensional close encounter of a curved tip vortex with a rotating blade, the helicopter rotor undergoes a variety of blade-vortex interactions depending on the interaction angle between the leading edge of the rotating blade and the curved line vortex. These interactions are generally unsteady and three dimensional. One limiting case of such an encounter, for zero interaction angle, is termed parallel interaction (see, e.g., Ref. 7). In the experimental configuration considered here, this interaction occurs around Ψ = 180-deg azimuthal position. For an observer riding with the blade (at a given reference station along the span), it appears as though the observer is passing a fixed vortex in the flow. For this reason, this interaction is sometimes approximated as two-dimensional and unsteady.

To calculate accurately the blade-vortex interaction flowfield, it is necessary to preserve the vortex structure without numerical diffusion. As mentioned before, one method that has been demonstrated to work effectively and economically in achieving this is the prescribed-disturbance scheme.[7,8] The effectiveness of this scheme is illustrated in Fig. 7, showing the variation of lift coefficient as a function of vortex position during a two-dimensional airfoil-vortex interaction calculated using the Navier-Stokes, Euler, and transonic small-disturbance methods. Also shown in this figure is the Euler lift distribution calculated using a conventional (vortex capturing) technique.[24] Although the two Euler solutions are computed on the same grid, the numerical dissipation associated with the finite difference grids progressively weakens the gradients and reduces the effective vortex strength in the conventional method. Also, this numerical error is grid dependent (the finer the grid the lesser the error); however, it is completely absent in the prescribed-vortex solutions, which are essentially grid independent. Hence, the prescribed-disturbance method has been used here for preserving the vortex structure.

Subcritical Interaction

The results of a subcritical parallel BVI are discussed here. This case corresponds to the flow conditions of $M_{tip} = 0.6$, $\mu = 0.2$, and $C_k\hat{\Gamma} = 0.133$ at a blade reference station $r_B = 0.893$. The interacting vortex is located at $x_o = 0.0$ and $z_o = 0.4$ along the y axis. To calculate the BVI flowfield, the interacting vortex is introduced into the baseline rotor solution at the azimuthal position of Ψ = 120 deg. The unsteady flowfield is monitored as the blade is set in motion to advance in azimuth. The blade-vortex interaction effects peak around Ψ = 180-deg azimuthal position. The instantaneous surface pressure distributions are shown in Fig. 8 for several az-

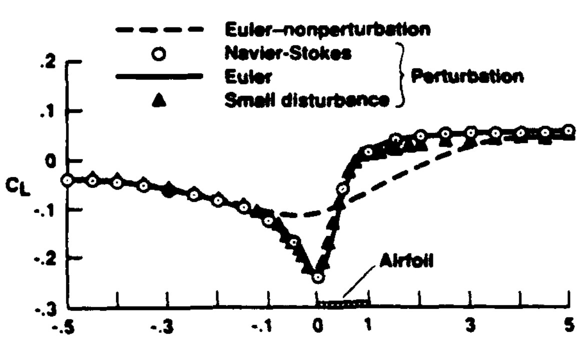

Fig. 7 Demonstration of prescribed-vortex method for preserving vortex structure in two-dimensional airfoil-vortex interaction: NACA 64A006 airfoil; $M_\infty = 0.85$, $\Gamma = 0.2$, and $z_v = -0.26$.

imuthal locations. The present results are compared with the experimental data[2] and the results from published two-dimensional Navier-Stokes calculations.[8]

The present results are in very good agreement with both the experimental data and the two-dimensional Navier-Stokes results. As seen from Fig. 8a for Ψ = 178.15 deg, the lift on the blade, which is initially zero in the absence of vortex interaction, is negative. Because of the sense of its rotation, the approaching vortex introduces a downwash in the flow immediately ahead of the blade. The lift rapidly becomes positive as the blade passes the line vortex. This crossover of lift, from negative to positive, seems to occur when the vortex is approximately aligned with the quarter-chord line of the blade (corresponding to $\bar{x}_v = 0.0$). As mentioned before, the two-dimensional approximation of this three-dimensional, unsteady interaction is, in fact, a very good assumption for this subcritical flow condition. The close agreement of the viscous and inviscid results suggests that the viscous effects are unimportant for this relatively weak interaction.

Supercritical Interaction

This case corresponds to the flow condition of $M_{\text{tip}} = 0.8$, $\mu = 0.2$, and $C_\ell\hat{r} = 0.177$ at a blade reference station of $r_B = 0.893$. The interacting vortex location is the same as in the subcritical case. As in the rotor-alone case this flow condition, in contrast to the subcritical flow condition, exhibits strong unsteady time-lag effects in shock-wave growth and decay for the advancing rotor. This feature seems to accentuate the three-dimensional nature of the flow, and a two-dimensional approximation of this flow overpredicts the shock-wave strength and location, as demonstrated in Ref. 8.

As before, to calculate the BVI flowfield, the interacting vortex is introduced at Ψ = 120-deg azimuthal position, and the time evolution of the flow is monitored as the blade advances in azimuth. Figure 9 shows the interaction flowfield results in terms of instantaneous surface pressures for several azimuthal positions of the blade. Also shown in these figures are the experimental data.[2] The present results are in good agreement with the experimental data for all azimuthal locations of the blade, and they capture the essential details of the flow sharply, including the shock waves.

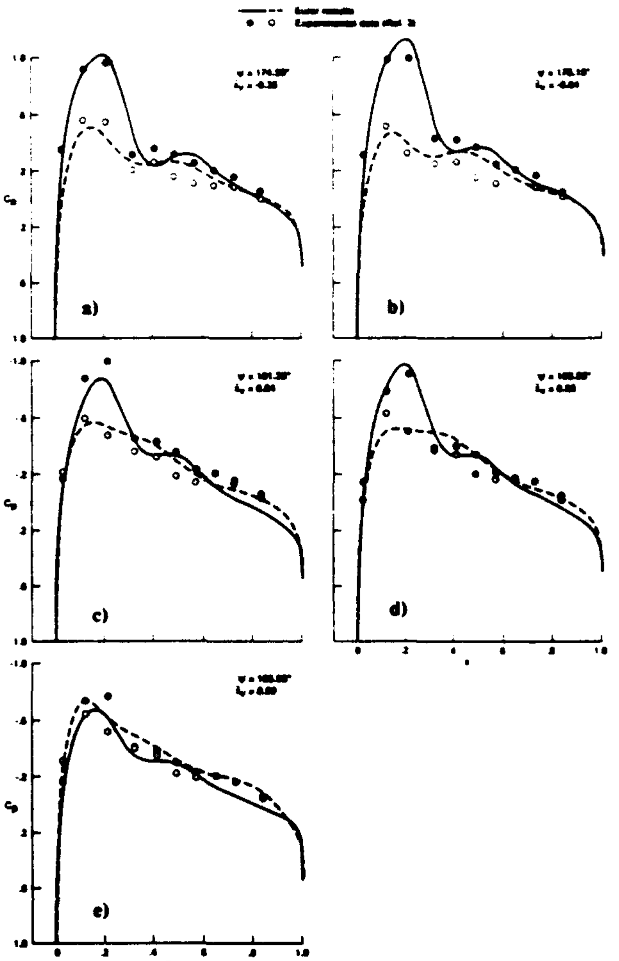

Fig. 9 Comparison of instantaneous surface pressures during parallel blade-vortex interaction for transonic case ($M_{\text{tip}} = 0.8$, $\mu = 0.2$, $C_\ell\hat{r} = 0.177$, $x_o = 0.0$, $z_o = 0.4$, and $r_B = 0.893$).

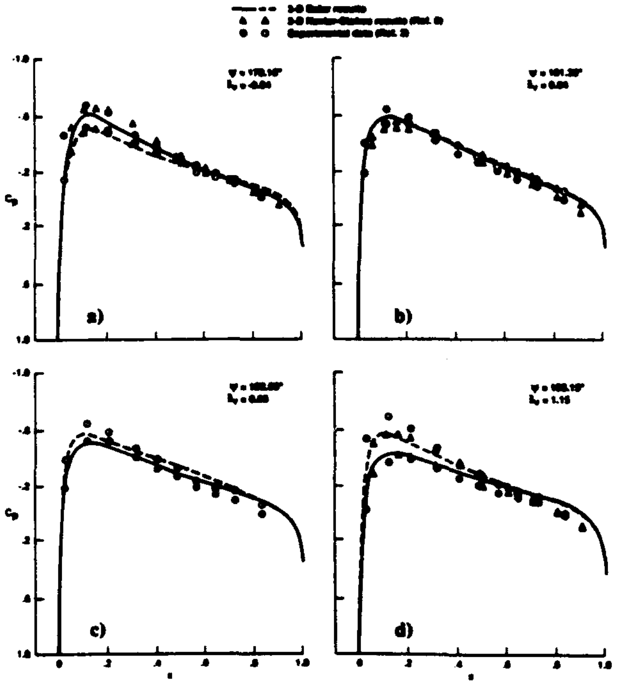

Fig. 8 Comparison of instantaneous surface pressures during parallel blade-vortex interaction for subsonic case ($M_{\text{tip}} = 0.6$, $\mu = 0.2$, $C_\ell\hat{r} = 0.133$, $x_o = 0.0$, $z_o = 0.4$, and $r_B = 0.893$).

The effect of vortex interaction is to induce time-dependent aerodynamic forces on the rotor. For example, as seen from the surface pressure plots of Fig. 9, the lift on the blade, which is initially zero, becomes negative due to induced downwash and rapidly increases to a positive value as the blade passes the stationary vortex. The peak effects of the interaction appear to occur when the blade leading edge is approximately above the line vortex.

Oblique Blade-Vortex Interaction

An interaction is called oblique when the line vortex interacts over a large part of the blade in the radial direction at any given instant of its azimuthal travel. In other words, an observer fixed to the blade and moving with it sees at any given instant different parts of the line vortex interacting with the blade as it sweeps from 0 to 180 deg in azimuth (in the present case). As seen in the schematic of Fig. 2, an oblique interaction is therefore possible whenever x_o is nonzero. This is in contrast to the parallel blade-vortex interaction that occurs when $x_o = 0.0$ where an observer located at one radial station sees the blade passing a point vortex that is stationary. The observer is therefore concerned about the influence of the entire line vortex at this particular radial station. Therefore, for an observer stationed on the blade, the interaction experienced of parallel and oblique BVI is uniquely different.

The oblique interaction considered here corresponds to a freestream condition of $M_{\text{tip}} = 0.763$ and $\mu = 0.197$. The interacting vortex located at $x_o = -2.13$ and $z_o = 0.25$ has a

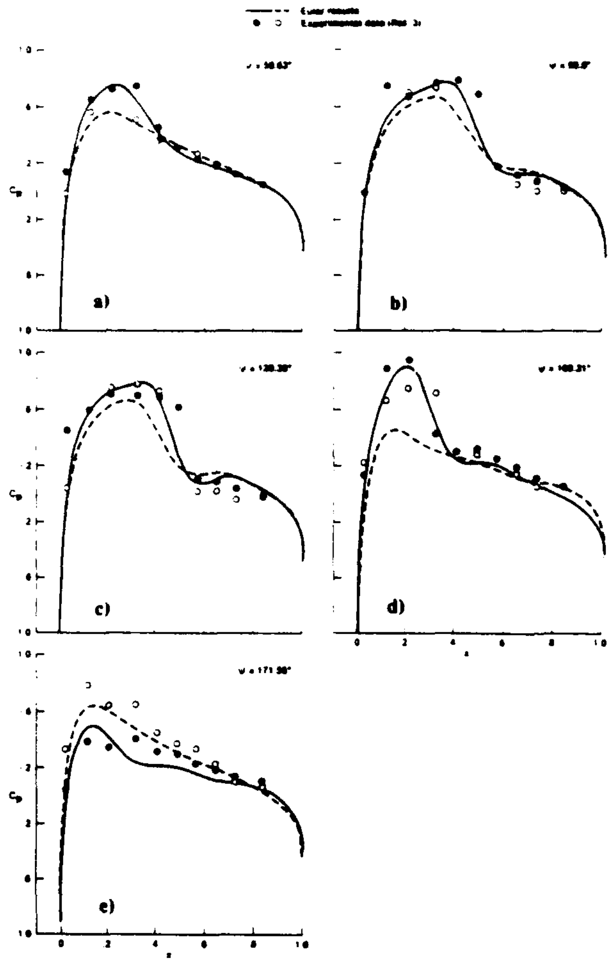

Fig. 10 Comparison of instantaneous surface pressures during oblique blade-vortex interaction for transonic case ($M_{tip} = 0.763$, $\mu = 0.197$, $C_k\hat{\Gamma} = 0.179$, $x_o = -2.13$, $z_o = 0.25$, and $r_B = 0.946$).

strength of $C_k\hat{\Gamma} = 0.179$ for the reference blade section at $r_B = 0.946$. In contrast to the parallel interaction, the oblique interaction occurs over a larger azimuthal sweep of the rotor blade, starting in the first quadrant and completing in the second quadrant. The peak interaction occurs at around $\Psi = 20$ deg in the first quadrant and around $\Psi = 160$ deg in the second quadrant. Therefore, the vortex is introduced into the flow at $\Psi = 0.0$ deg in this case, and the evolution of the unsteady interacting flow is monitored for the advancing rotor.

Figure 10 shows the calculated instantaneous surface pressure distributions at several azimuthal positions of the blade and the experimental data.[3] The comparison of results shows overall agreement of surface pressures. This set of experimental data appears to have large scatter. Even the surface pressures of rotor-alone case have similar scatter.[25] The interaction in the first quadrant occurs at subcritical flow and the agreement with data is good at $\Psi = 50$ deg. The interaction in the second quadrant occurs under supercritical flow condition. The maximum relative blade tip speed in this case (for $\Psi = 90$-deg position) is 0.91 compared to a value of 0.96 corresponding to the transonic parallel interaction case and is thus a weaker interaction.

From the surface pressures of Fig. 10 it can be seen that the lift on rotor blade, which is initially zero, becomes negative due to the vortex influence (because of the sense of rotation), increases to a maximum (negative) value in the second quadrant, and changes over to a positive value at about $\Psi = 165$-deg azimuthal position of the blade. The peak interaction appears to occur around the $\Psi = 160$-deg azimuthal position.

Conclusions

A numerical procedure is presented to calculate the unsteady, inviscid, three-dimensional flowfields of a helicopter rotor in forward flight encountering parallel and oblique blade-vortex interactions in subsonic and transonic flow conditions. Important flow features such as unsteady time-lag effects in shock-wave growth and demise, as well as the importance of three-dimensional effects, are discussed. Although it is possible under certain flow conditions to approximate the parallel blade-vortex interaction as two dimensional and unsteady, the oblique blade-vortex interaction, on the other hand, is strongly three dimensional and unsteady, and therefore cannot be approximated as two-dimensional interaction.

The numerical results are compared with two sets of experimental data generated by Caradonna et al.[2,3] on a model two-bladed rotor in a wind tunnel. The present Euler results show good agreement with experiments for both the parallel and oblique interactions at subsonic and transonic flow conditions. Thus, the numerical methodology presented here has demonstrated the ability to accurately calculate the flowfield of an advancing helicopter rotor including the effects of vortex interaction.

Acknowledgments

The first author (GRS) would like to acknowledge the support of this research by the U. S. Army Research Office under Contract DAAL03-88-C-0006 and DAAL03-90-C-0013. Computational time was provided by the Applied Computational Fluids Branch of NASA Ames Research Center. The authors would like to dedicate this paper to the memory of J. L. Steger.

References

[1] Srinivasan, G. R., McCroskey, W. J., Baeder, J. D., and Edwards, T. A., "Numerical Simulation of Tip Vortices of Wings in Subsonic and Transonic Flows," *AIAA Journal*, Vol. 26, No. 10, 1988, pp. 1153–1162.

[2] Caradonna, F. X., Laub, G. H., and Tung, C., "An Experimental Investigation of the Parallel Blade-Vortex Interaction," 10th European Rotorcraft Forum, The Hague, The Netherlands, Aug. 1984; also NASA TM-86005, Nov. 1984.

[3] Caradonna, F. X., Lautenschlager, J., and Silva, M., "An Experimental Study of Rotor Blade-Vortex Interactions," AIAA Paper 88-0045, Jan. 1988.

[4] Workshop on Blade-Vortex Interactions (unpublished), NASA Ames Research Center, Moffett Field, CA, Oct. 1984.

[5] Rai, M. M., "Navier-Stokes Simulation of Blade-Vortex Interaction Using High-Order Accurate Upwind Schemes," AIAA Paper 87-0543, Jan. 1987.

[6] Steinhoff, J., and Suryanarayanan, K., "The Treatment of Vortex Sheets in Compressible Potential Flow," AIAA Paper 83-1881-CP, July 1983.

[7] Srinivasan, G. R., and McCroskey, W. J., "Numerical Simulations of Unsteady Airfoil-Vortex Interactions," *Vertica*, Vol. 11, No. 1/2, 1987, pp. 3–28.

[8] Srinivasan, G. R., McCroskey, W. J., and Baeder, J. D., "Aerodynamics of Two-Dimensional Blade-Vortex Interaction," *AIAA Journal*, Vol. 24, No. 10, 1986, pp. 1569–1576.

[9] Wu, J. C., Sankar, N. L., and Hsu, T. M., "Unsteady Aerodynamics of an Airfoil Encountering a Passing Vortex," AIAA Paper 85-0203, Jan. 1985.

[10] Strawn, R. C., and Tung, C., "The Prediction of Transonic Loading on Advancing Helicopter Rotors," NASA TM-88238, April 1986.

[11] Caradonna, F. X., Strawn, R. C., and Bridgeman, J. O., "An Experimental and Computational Study of Rotor-Vortex Interactions," *Vertica*, Vol. 12, No. 4, 1988, pp. 315–327.

[12] George, A. R., and Lyrintzis, A. S., "Acoustics of Transonic Blade-Vortex Interactions," *AIAA Journal*, Vol. 26, No. 7, 1988, pp. 769–776.

[13] Lyrintzis, A. S., and George, A. R., "Far-Field Noise of Transonic Blade-Vortex Interactions," *American Helicopter Society Journal*, Vol. 34, No. 3, pp. 30–39.

[14] Baeder, J. D., McCroskey, W. J., and Srinivasan, G. R., "Acoustic Propagation Using Computational Fluid Dynamics," *Proceedings of the 42nd Annual Forum of the American Helicopter Society*, The American Helicopter Society, Washington, DC, June 1986, Vol. 1,

pp. 551-562.

[15]Damodaran, M., and Caughey, D. A., "A Finite Volume Euler Calculation of the Aerodynamics of Transonic Airfoil-Vortex Interaction," *AIAA Journal*, Vol. 26, No. 11, 1988, pp. 1346-1353.

[16]Pulliam, T. H., and Steger, J. L., "Implicit Finite-Difference Simulations of Three-Dimensional Compressible Flow," *AIAA Journal*, Vol. 18, No. 2, 1980, pp. 159-167.

[17]Srinivasan, G. R., and McCroskey, W. J., "Navier-Stokes Calculations of Hovering Rotor Flowfields," *Journal of Aircraft*, Vol. 25, No. 10, 1988, pp. 865-874.

[18]Isom, M. P., "Unsteady Subsonic and Transonic Potential Flow Over Helicopter Rotor Blades," NASA CR-2463, Oct. 1974.

[19]Ying, S. X., Steger, J. L., Schiff, L. B., and Baganoff, D., "Numerical Simulation of Unsteady, Viscous, High-Angle-of-Attack Flows Using a Partially Flux-Split Algorithm," AIAA Paper 86-2179, Aug. 1986.

[20]Steger, J. L., and Warming, R. F., "Flux Vector Splitting of the Inviscid Gasdynamic Equations with Application to Finite-Difference Methods," *Journal of Computational Physics*, Vol. 40, No. 2, 1981, pp. 263-293.

[21]Steger, J. L., and Chaussee, D. S., "Generation of Body-Fitted Coordinates Using Hyperbolic Partial Differential Equations," *SIAM J. Sci. Stat. Comput.*, Vol. 1, No. 4, 1980, pp. 431-437.

[22]Jameson, A., Schmidt, W., and Turkel, E., "Numerical Solution of the Euler Equations by Finite Volume Methods Using Runge-Kutta Time-Stepping Schemes," AIAA Paper 81-1259, June 1981.

[23]Chakravarthy, S. R., "Euler Equations—Implicit Schemes and Boundary Conditions," *AIAA Journal*, Vol. 21, No. 5, 1983, pp. 699-706.

[24]Srinivasan, G. R., Chyu, W. J., and Steger, J. L., "Computation of Simple Three-Dimensional Wing-Vortex Interaction in Transonic Flow," AIAA Paper 81-1206, June 1981.

[25]Srinivasan, G. R., and McCroskey, W. J., "Unsteady Interaction of a Rotor With a Vortex," AIAA Paper 89-1848, June 1989.